Mars Habitability: An Investigation of Martian Meteorites and Terrestrial Analogues – Implications for Mars Sample Return

Lewis Sean Jamie Sym

BSc (Honours) Chemistry, University of Glasgow

Submitted in fulfilment of the requirements for the

Degree of Masters by Research

School of Geographical & Earth Sciences

College of Science and Engineering

University of Glasgow

October 2023

Abstract

The current Mars Sample Return (MSR) mission is poised to return rock samples to Earth from the surface of Mars as early as 2033 – with a major goal of this ground-breaking mission being the investigation of Martian biology. In response to the preparation and development required for a successful MSR mission, this project aims to both further the understanding of Martian habitability and prepare for the analysis of returned samples in a biological context. An extensive literature compilation of 11 nakhlite Martian meteorites is produced including the bulk rock compositions, iddingsite compositions, and crystallisation ages. Evidence is presented supporting both a low water-rock ratio ephemeral interaction and a high water-rock ratio potentially long-lived hydrothermal environment as the true nature of the Nakhlite launch site's aqueous alteration. An ephemeral alteration is ultimately favoured. Atom probe tomography (APT) analyses of the nakhlite Northwest Africa 817 illuminate that, given more attention, APT holds the potential to assist in distinguishing between these two end-case scenarios for the nakhlite alteration (which present greatly differing habitability potentials). An analytical pipeline is successfully employed to directly probe nm-scale carbon inclusions preserved within fossiliferous Rhynie chert and Yellowstone National Park samples (both known terrestrial analogue sites resembling Martian hydrothermal environments). The methodology and analytical avenues presented in these terrestrial analogue investigations can serve as a guide for future returned Martian sample interrogations in the search for preserved Martian biosignatures. Along with evaluating the analytical workflow's effectiveness, multiple recommendations are proposed to improve the pipeline in response to issues experienced throughout this project – developing the pipeline such that better, more robust, results may be obtained in future utilisations. This work carries MSR implications, embodying a step towards the preparation for the analysis of returned Martian samples in a biological context, and also serves to advocate for the usage of APT in the analysis of Martian meteorites, returned Martian samples, and further planetary science materials.

Table of Contents

List of Tables

Tables:

Appendix tables:

List of Figures

Figures:

Appendix figures:

Acknowledgements

Firstly, I would like to thank my primary supervisor, Professor Martin Lee, for their continued support, guidance, and insight throughout the entirety of the project – advising many aspects of work including selecting appropriate samples, data collection, and thesis writing.

Secondly, I would like to acknowledge my secondary supervisor, Dr Luke Daly, for their assistance with, and insights into, APT analysis and for allowing me to access the spare computer in their office which had APT analysis software installed.

Furthermore, I extend my gratitude to Dr Liene Spruzeniece, Mr William Smith, Dr Connor Brolly, Dr Annemarie Pickersgill, and Dr Joshua Einsle for their patient advice and assistance with both sample preparation and equipment operation throughout the project.

I would also like to thank Dr Iain Neill for their helpful comments on the introduction chapter.

Additionally, I would like to thank both Sammy Griffin and Professor James Day for allowing me to include their nakhlite data in the literature compilation produced in this project.

Finally, I would like to express my thanks to Dr Neil Clark and the University of Glasgow's Hunterian Museum for generously supplying the Rhynie chert and Yellowstone National Park terrestrial analogue samples utilised in this project.

This MScR project was funded (*i.e.* tuition fee paid for) by a SAAS postgraduate tuition fee loan – an opportunity I am grateful for.

Declaration of Originality

I hereby declare that, except where explicit reference is made to the contributions of others, this thesis is the result of my own work and has not been submitted for any other degree at the University of Glasgow or any other institution.

List of Abbreviations

Abbreviations:

ALH84001 –	Alan Hills 84001
APT –	Atom Probe Tomography
BSE –	Backscattered Electrons
EDX –	Energy-dispersive X-ray Spectroscopy
FIB –	Focused Ion Beam
FTIR –	Fourier Transform Infrared Spectroscopy
FWHM –	Full Width at Half Maximum
HAADF –	High-angle Annular Dark-Field
iMOST –	International MSR Objectives and Samples Team
IR –	Infrared
LEAP –	Local Electrode Atom Probe
MIL –	Miller Range
MOLA –	Mars Orbiter Laser Altimeter
MSR –	Mars Sample Return
NASA –	National Aeronautics and Space Administration
NWA –	Northwest Africa
SE –	Secondary Electrons
SEM –	Scanning Electron Microscopy
SNC –	Shergottites, Nakhlites, and Chassignites
STEM –	Scanning Transmission Electron Microscopy
TEM –	Transmission Electron Microscopy
vol% –	Volume percentage
WiRE –	Windows-based Raman Environment
wt% –	Weight percentage (or Weight%)
Y-000593 –	Yamato 000593
Y-000749 –	Yamato 000749
Y-000802 –	Yamato 000802

1. Introduction

1.1 Aims and Objectives

1.1.1 Research Goals

The biology of Mars has been a topic of interest amongst planetary scientists for centuries (Mumma, 2012), and continues to maintain relevance today – with a wealth of missions planned (Martín-Torres *et al.*, 2020), or underway (Farley *et al.*, 2020), that are aiming to investigate this area. The study of Martian biology has taken many forms over the years, including: the study of analogous samples or environments (Storrie-Lombardi and Sattler, 2009); the interrogation of Martian meteorites on Earth (Nascimento-Dias *et al.*, 2018); remote observations from Earth-based telescopes (Krasnopolsky *et al.*, 2004); and *in situ* observations from Mars orbiters (Carr *et al.*, 1972), rovers (Szopa *et al.*, 2020), and landers (Klein, 1979). However, research in this area is undoubtedly far from complete and, with the prospect of Martian rock samples being returned to Earth as early as 2033 (mars.nasa.gov, 2022), adequate preparation and advancement in this field is vital. As such, this project will strive to expand upon the research surrounding Martian meteorites, Mars terrestrial analogues, and the analytical techniques involved in their investigation, all with the aim of better understanding the habitability of Mars. More specifically, the main goals of this project are to:

1. Build upon and extract information from Martian meteorites concerning the past habitability of Mars.
2. Investigate Mars terrestrial analogues to guide and inform the analysis of samples to be returned from Mars.
3. Develop and evaluate the employed analytical pipeline for such planetary science applications.

1.1.2 Research Questions

To facilitate the achievement of these goals, this project will endeavour to answer the following research questions:

1. What further information can be garnered concerning the past habitability of Mars from the investigation of the aqueous alteration of the nakhlite Martian meteorites?

2. Can the interrogation of the Rhynie chert and Yellowstone Mars terrestrial analogue sites guide and inform the analysis of returned Martian samples in the search for preserved biosignatures?
3. Can the analysis of terrestrial analogues develop and evaluate the effectiveness of the analytical pipeline for planetary science applications?

Question 1: The nakhlites represent a group of Martian meteorites, host to a wide range of aqueous alteration products that are collectively referred to as iddingsite, thought to originate from the same launch site on the Martian surface (Udry *et al.,* 2020). Thus, it follows that the investigation of the nakhlites' aqueous alteration can allow crucial insights into the nature and abundance of the Martian water that the nakhlite rocks once interacted with (and potentially other factors of the nakhlite launch site) – where understanding the characteristics of available water inventories is key in determining habitability conditions (Brack *et al.*, 2010). As such, this project's interrogation of the aqueous alteration products found in the nakhlites will strive towards better understandings of past Martian habitability.

Question 2: The Rhynie chert and Yellowstone National Park sites represent areas of (past or present) hydrothermal activity in which life is preserved as fossils within silica sinters (Walter and Des Marais, 1993; Rice *et al.*, 2002). Following this, due to the presence of hydrothermal activity on Mars (Turner *et al.*, 2016), samples from these terrestrial analogue sites present the invaluable opportunity to investigate the potential preservation of biosignatures in analogous Martian hydrothermal environments – areas of undoubted interest for selecting samples to return to Earth (Beaty *et al.*, 2019). Accordingly, this project's work on investigating the preservation of biosignatures in these terrestrial analogue samples could be used towards directing and informing the analysis of any returned Martian hydrothermal samples in the search for preserved biosignatures.

Question 3: The analytical pipeline involves the collaborative use of multiple analytical techniques (*i.e.* optical microscopy, Raman spectroscopy, scanning electron microscopy, transmission electron microscopy, and atom probe tomography) – culminating in a high-resolution description of a sample at the nanometre scale. As such, the investigations throughout this project (mainly on Mars terrestrial analogues) will strive to utilise this analytical strategy with the aim of procuring unique insights into preserved biosignatures (displaying the extraordinary scientific power of this method) and identifying key issues (whilst proposing potential solutions to improve the pipeline).

A more comprehensive review of the background literature and rationale behind the utilisation of the nakhlites, the chosen Mars analogues, and the employed analytical suite will be discussed later in this chapter. Although, to start, the following section will introduce and outline the background research surrounding the overarching theme of this project – Martian habitability.

1.2 Martian Habitability

1.2.1 Habitability of Terrestrial Planets

What exactly is habitability? As highlighted in a recent review by Cockell *et al.* (2016), the term "habitability" has seen many revisions to its definition over the years. Ultimately, they suggest that a habitable environment is one which can support the activity of at least one known organism. Crucially, their working definition, and others' (Dartnell, 2011), solely encompass conditions which can support known life – intentionally excluding environments which could potentially sustain undiscovered hypothetical organisms (to avoid speculation). It follows that the extent of the habitability envelope (by this definition) is delineated by the limits of life in extreme conditions on Earth – *i.e.* extremophiles. For example, Stetter (1982) details his discovery and characterisation of hyperthermophilic organisms taken from underwater volcanic systems. He determined that the optimal growth temperature of these organisms was 105 °C, significantly above the previously observed highest optimal growth temperatures of 70 – 85 °C of other thermophilic organisms. This work represents an advancement in the known capabilities of life on Earth, expanding the range of observed temperatures that allow the proliferation of life, undoubtedly serving to further the criteria defining a habitable environment. Additionally, Pikuta *et al.* (2007) review similar examples of extremophiles persisting in a range of physical and chemical conditions, including extreme cold, pH, pressure, salinity, and radiation – all of which contribute to expanding upon the known limits of life and, thus, habitability. Importantly, the presence of liquid water is recognised as a universal prerequisite for any known life (Cockell *et al.*, 2016). Thus, the search for liquid water, and establishing its physiochemical properties, is imperative in determining the habitability of other planets. It should be noted that many other astrophysical factors must also be considered when determining the continuous habitability of a planet over geological time scales (*e.g.* planetary mass, nature of the host star, and orbital characteristics (Guedel *et al.*, 2014; Cockell *et al.*, 2016)). The investigation of other planetary bodies in our solar system, not just Earth, can similarly facilitate developments in

the field of planetary habitability (Preston and Dartnell, 2014). This, plus potentially the most promising prospects of harbouring habitable environments (Horowitz, 1976), has led Mars to become a prime target of abundant biological investigation throughout the years (Fairén *et al.*, 2010b).

Research surrounding Mars has seen much focus on the habitability of the planet (Westall *et al.*, 2013) – a trend that continues even today, with a main objective of many missions to Mars being the assessment of potential life on the red planet (Grotzinger *et al.*, 2012; Williford *et al.*, 2018). This astrobiological movement started with the touchdown of the Viking landers on the surface of Mars in 1976, where a major objective of the landers was to evaluate the presence of extant life on the Martian surface (Klein *et al.*, 1976). Despite not finding definitive evidence of Martian organisms (Klein, 1999; Quinn *et al.*, 2013) (although the abiotic explanations of Viking experiment results is contested by some (Levin and Levin, 1998; Levin and Straat, 2016)), the mission paved the way for, and shaped, future enquiry into the past and present habitability of Mars (Klein, 1998; Fairén *et al.*, 2010b). In particular, Fairén *et al.* (2010b) highlight that further investigations into habitability strived to better understand the evolution of the planet, with unsurprising attention given to the role and prominence of water throughout Mars' history. For example, the subsequent National Aeronautics and Space Administration (NASA) Mars lander (and rover) mission after Viking, titled Pathfinder, aimed to further investigate the atmosphere, surface, and interior of Mars in order to provide valuable context for orbital interrogations (Golombek, 1997). Most notably, observations from the Pathfinder mission, including the presence of rounded pebbles, dust-sized particles, and rocks rich in silica, served to support the previously proposed (Pollack *et al.*, 1987; Squyres and Kasting, 1994) theory that Mars experienced a much wetter and warmer, Earth-like, past (Golombek *et al.*, 1997). This 'liquid-water-abundant past' hypothesis, an idea still discussed in recent years (Wordsworth, 2016; Lasue *et al.*, 2019), importantly illuminates a potential period in Martian history which may have been favourable to the emergence and proliferation of life. Exploring this idea potentially provides habitability insights and may inform future searches as to where signs of extinct life from this era are most likely to reside (Bishop *et al.*, 2013; Vago *et al.*, 2017). Undoubtedly owing to the efforts of Mars habitability investigations, such as the previous example, there exists evidence to suggest that Mars experienced three geological epochs (Carr and Head, 2010; Fairén *et al.*, 2010b). These individual geological ages present differing habitability conditions (Fairén *et al.*, 2010b).

1.2.2 Epochs

1.2.2.1 Early Mars

It is believed that, excluding a hostile induction period soon after planetary formation (Elkins-Tanton, 2008), early Mars was characterised by a dense CO_2 atmosphere (Elkins-Tanton, 2008; Vago *et al.*, 2017) which could provide adequate pressure to allow liquid water to persist and potentially warmed the planet (Vago *et al.*, 2017; Green *et al.*, 2021). Furthermore, early Mars possessed a global magnetosphere (Acuña *et al.*, 1998, 2001; Lillis *et al.*, 2013) (protecting the planet from the Sun's radiation (Green *et al.*, 2021)), and abundant liquid water (Fairén *et al.*, 2010b; Vago *et al.*, 2017) – representing an exceptionally promising window which may have been conducive to the genesis and propagation of life. This liquid-water abundance is supported by evidence of extensive hydrological activity concentrated on the still-exposed primordial Martian surface (Wordsworth, 2016), such as valley networks (Matsubara *et al.*, 2013; Seybold *et al.*, 2018), crater lakes (Goudge *et al.*, 2012; Horvath and Andrews-Hanna, 2017), and aqueously altered materials (Fairén *et al.*, 2010a; Carter *et al.*, 2013) (see Figure 1).

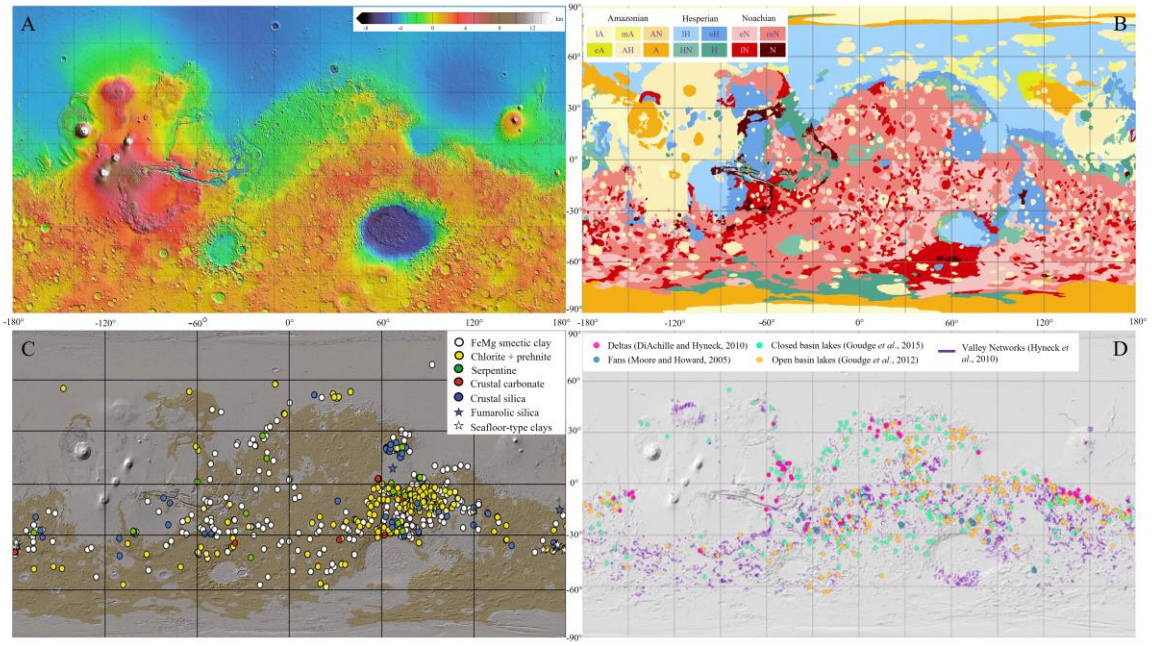

Figure 1 – Surface maps of Mars. A) Topographical map of the Martian surface constructed by the NASA MOLA (Mars Orbiter Laser Altimeter) science team utilising MOLA data (credit: (Neumann and Terrence, 2007)). B) Geological map of Mars detailing the age of surface material with respect to the common Martian eras (credit: (Tanaka *et al.*, 2014)). Key: e = early, m = middle, l = late, A = Amazonian, H = Hesperian, N = Noachian, where two eras are noted (*e.g.* HN) such an area spanned over both epochs. C) Global distribution of hydrothermally altered materials (credit: (Michalski *et al.*, 2018)). D) Global distribution of features produced by aqueous activity (*e.g.* valley networks) on the surface of Mars utilising data from various sources (Moore and Howard, 2005; DiAchille and Hynek, 2010; Hynek *et al.*, 2010; Goudge *et al.*, 2012, 2015) over a MOLA topography map (Smith *et al.*, 2001) (credit: (Lasue *et al.*, 2019)). By comparing B) to D), it becomes clear that most aqueous features are situated over still-exposed, primeval, Noachian terrain (red and pink colours in B)). Comparing B) to C) shows a similar trend, where the majority of detected hydrothermally altered materials exist on the primordial Noachian surface. Note: figures and keys have been slightly altered to match this project's format.

Moreover, it is suggested that these conditions continued from shortly after planetary formation to the late Noachian or early Hesperian era (Vago *et al.*, 2017) (see Figure 2) – potentially presenting a reasonably-sized window in which a Martian biosphere could prosper. Although, contrary to some models proposing a much warmer climate in Mars' early history (Pollack *et al.*, 1987; Craddock and Howard, 2002; Ramirez and Craddock, 2018), many recent models suggest that early Mars may not have been particularly temperate (Wordsworth *et al.*, 2015; Wordsworth, 2016). The rationale behind this 'cold early Mars' scenario is typically based on Mars' further distance (roughly 1.52 AU) from the much younger, and thus fainter, sun. As calculated by Vago *et al*. (2017), the effective temperature on Mars would be 204 – 189 K (based on differing albedo values) which is much too cold for liquid water to persist – necessitating an extreme temperature contribution from the greenhouse effect of the primeval Martian atmosphere to reach even 0 °C (Wordsworth, 2016). Instead, these models suggest that early Mars was punctuated by periods of transient warmth, and thus ephemeral liquid water (explaining observed aqueous features), potentially fuelled by volcanic eruptions (Halevy and Head III, 2014), impact events (Segura *et al.*, 2008), and maybe even assisted by changes in orbital obliquity (Mischna *et al.*, 2013). Nonetheless, early Mars, with its water abundance and at least episodic warmth, is regarded as a key target for habitability investigations and this is highlighted by, for example, early Mars being the prime investigation target of the upcoming astrobiology-focused ExoMars rover (Vago *et al.*, 2017). However, transitioning from wet early Mars, the succeeding global climatic scenario, starting around the late Noachian to early Hesperian (see Figure 2), is believed to have been dominated by a planetary-scale cryosphere (Fairén *et al.*, 2010b) – likely altering the habitability potential of the planet.

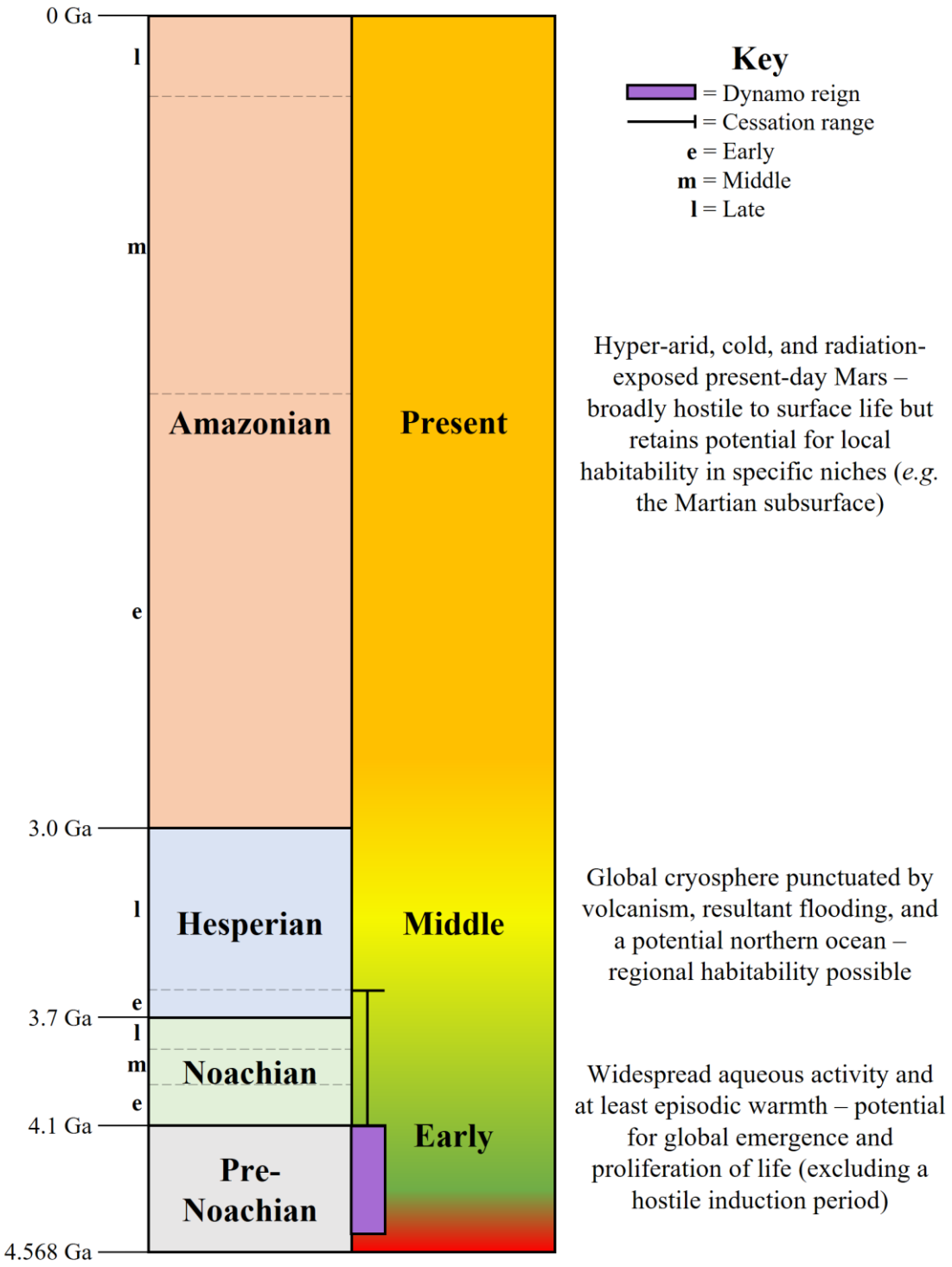

Figure 2 – Timeline of Martian history adapted from various sources (Hartmann and Neukum, 2001; Fairén *et al.*, 2010b; Vago *et al.*, 2017; Udry *et al.*, 2020). Left section is the main Martian periods with their boundaries given in Ga and split into common subsections (*e.g.* late Noachian) by dashed grey lines (see key). Middle section represents the main geological epochs in Martian history with their habitability potentials suggested by their colour – *i.e.* ranging from green = favourable to life – red = hostile to life. Overlaying this section is a purple bar demarking the potential reign of the Martian dynamo and the following black bar represents the range of suggested times at which dynamo cessation occurred (Milbury *et al.*, 2012; Lillis *et al.*, 2013; Mittelholz *et al.*, 2020) (*i.e.* it has been proposed that it could have ceased early at 4.1 Ga, or late at 3.6 Ga). Right section provides a brief explanation of the relevant global conditions and habitability potential of each geological era.

1.2.2.2 Middle Mars

The second major epoch in Martian history is characterised by the loss of the magnetosphere (due to the suspected cessation of the dynamo (Milbury *et al.*, 2012; Lillis *et al.*, 2013)). The resultant drops in atmospheric pressure (potentially driven by atmospheric erosion from subsequently-unshielded exposure to the solar wind (Chassefière *et al.*, 2007)), and lowering of global temperatures (possibly accelerated by the lessening greenhouse warming effect of a thinning atmosphere (McKay *et al.*, 1992)), potentially led to the development of a thick cryosphere – producing an icy and likely less-hospitable middle Mars (Carr and Head, 2010, 2019; Fairén *et al.*, 2010b). Evidence to support this climatic shift is a significant decrease in the formation of aqueously-produced features (such as erosion and valley networks) compared to the late Noachian, suggesting a marked decrease in surface liquid water inventories (Carr and Head, 2010; Schwenzer *et al.*, 2012). Additionally, outflow channels believed to have formed by voluminous groundwater release are proposed, in some models, to necessitate (or at least suggest) the presence of a thick cryosphere (Carr, 1996; Carr and Head, 2019). This further supports the model of a colder and drier middle Mars – presenting conditions likely less favourable to the persistence of life on the surface. However, there may be evidence (such as potential shorelines (Parker *et al.*, 1989, 1993; Citron *et al.*, 2018) and signs of impact-induced tsunamis (Rodriguez *et al.*, 2016; Costard *et al.*, 2019)) to suggest that the groundwater forming these immense floods collected into a large, possibly ice-covered (Parker *et al.*, 1993) or entirely frozen (Carr and Head, 2019), ocean in the northern plains. Although, this theory faces many controversies (Malin and Edgett, 1999; Head *et al.*, 2018; Turbet and Forget, 2019)). Furthermore, whilst evidence of liquid water is scarcer than in early Mars (Carr and Head, 2010), there remains signs of aqueous activity continuing into the Hesperian – *e.g.* valley networks near volcanoes, presumably produced by magmatically-fuelled meltwater (Fassett and Head, 2006, 2007) (where volcanic activity was plentiful during the Hesperian (Greeley and Schneid, 1991; Head, 2002; Carr and Head, 2010)). These factors (*i.e.* the potential cryosphere, ice-covered bodies of water, and local geothermal heating) have led this Martian era to be likened, by some (McKay *et al.*, 1992; Fairén *et al.*, 2010b), to the valleys of Antarctica on Earth in order to investigate the habitability potential of these conditions. McKay *et al.* (1992) highlight that ice-covered lakes in these valleys are host to planktonic organisms and microbial mats – presenting an example of life prospering in an analogous environment to what may have been present on middle Mars (where these environments could potentially persist for hundreds of millions of years under certain conditions (McKay and Davis, 1991)). Moreover, they highlight the ability of such microbial mats to form stromatolites, emphasising their potential to be

preserved for future detection. Thus, although not as promising for life as wetter early Mars, middle Mars may have had regional environments in which a Martian biosphere could prosper and potentially leave signs of its existence. However, towards the end of the Hesperian and into the start of the Amazonian, Mars is thought to have finished transitioning into the hyper-arid and hostile conditions that have prevailed for the past three billion years (Fassett *et al.*, 2010; Fairén *et al.*, 2010b) – further impacting the ability of life to proliferate on the Martian surface.

1.2.2.3 Present Mars

Present Mars is characterised by an extremely thin, mainly CO_2, atmosphere (*i.e.* a surface pressure of around 6.1 millibars (Jakosky and Phillips, 2001; Haberle, 2015)) and harsh mean surface temperatures (*e.g.* Gale crater daily average ground temperatures ranging from roughly -30 – -60 °C depending on the season (Centro de Astrobiología, 2017; Ordonez-Etxeberria *et al.*, 2018)). This results in a lack of surface liquid water (although it could exist ephemerally as certain brine compositions (Martínez and Renno, 2013; Rivera-Valentín *et al.*, 2020)). It is believed that these conditions have reigned across the entire Amazonian era (Fairén *et al.*, 2010b) – presenting some of the most inhospitable surface conditions in Martian history. On top of this, Mars' unprotected exposure to both cosmic rays and the Sun's harmful radiation could kill even otherwise-radiation-resistant terrestrial microorganisms (in a dormant state (Pavlov *et al.*, 2002)), degrade fossilised organic matter (Pavlov *et al.*, 2012), and may even produce biomolecule-destroying oxidants by reaction with the Martian soil (Quinn *et al.*, 2013; Lasne *et al.*, 2016). These factors further compound the threat to any extant life on the Martian surface and potentially reduce the likelihood of discovering signs of extinct Martian life. Despite the seemingly bleak set of surface conditions present throughout Amazonian Mars, the planet may not be entirely devoid of any potentially-habitable niches. Examples of these are the icy polar regions (transiently melted by periods of high orbital obliquity (Jakosky *et al.*, 2003; Stoker *et al.*, 2010)) and specific locales on the surface (*e.g.* soils containing salt knobs that could both shelter microorganisms from radiation and provide a source of ephemeral liquid water (Davila *et al.*, 2010a, b). Further, the Martian subsurface is potentially the most promising environment for hosting extant life on present-day Mars (Fisk and Giovannoni, 1999; Tarnas *et al.*, 2021). Notably, although pure water is generally unstable as a liquid under present Martian surface conditions (Ingersoll, 1970), brine solutions could remain stable as liquids at much lower temperatures than pure water due to freezing point depression from dissolved solutes (Brass,

1980; Martínez and Renno, 2013). Recent results suggest that there may exist substantial subglacial liquid water inventories (stable as a liquid due their solute compositions (Orosei *et al.*, 2018; Lauro *et al.*, 2021)) – potentially providing crucial liquid water environments for any extant Martian life to utilise. Although, River-Valentín *et al.* (2020) assert that the temperature and water activity remain limiting conditions for life in Martian liquid brines. Thus, despite conditions that could be considered the least hospitable in the planet's history, these factors highlight that present Mars arguably still maintains potential to harbour life in specific niches. As such, present-day Mars remains a key target of biological inquisition and discussion – evidenced by, for example, a main goal of the HABIT instrument onboard the upcoming ExoMars rover being the assessment of present-day habitability at Oxia Planum on Mars (Martín-Torres *et al.*, 2020). Regardless of the era being investigated, essential to the interrogation of habitability is the search for, and analysis of, tell-tale signs of extinct or extant life – *i.e.* biosignatures (Beaty *et al.*, 2019).

1.2.3 Biosignatures

The investigation of biosignatures is undoubtedly linked to the evaluation of a planet's habitability (Schwieterman *et al.*, 2018). In discussing NASA's plans for ensuing astrobiological investigations, Des Marais *et al.* (2008) define a biosignature to be an object, substance, or trend that explicitly requires a biological origin – *i.e.* a definitive sign of past or present life. They highlight the important distinction between a biosignature and a potential biosignature, where a potential biosignature represents a feature which may have biological origins, although its legitimacy as conclusive evidence of life is yet undecided, thus prompting further interrogation. A recent example of this, and the resulting discussion, is the potential discovery of phosphine gas (PH_3) in the Venusian atmosphere (Greaves *et al.*, 2021a). Greaves *et al.* (2021a) highlight that this, if accurate, is impactful because, in the absence of any known physical or chemical sources, the inclusion of phosphine in the Venusian atmosphere may be the result of biological processes, a theory supported by the fact that phosphine on Earth is connected almost entirely to life (Sousa-Silva *et al.*, 2020). However, the accuracy of this original assertion (*i.e.* that spectroscopic data was indicative of PH_3) has been subject to much debate (Snellen *et al.*, 2020; Thompson, 2020). For instance, Villanueva *et al.* (2021) argue that the spectral feature in the Greaves *et al.* (2021a) data set was misattributed to PH_3 and, instead, was potentially reflecting atmospheric SO_2. A follow-up paper by Greaves *et al.* (2021b) contests this conclusion by Villanueva *et al.*, stating that, amongst other arguments, an SO_2 abundance necessary to explain the observed

spectral peak would be abnormally large. As of the time of writing, no consensus has been met regarding the presence or abundance of phosphine in Venus' atmosphere (Greaves *et al.*, 2021c; Bains *et al.*, 2021), a testament to the extensive scrutiny potential biosignatures face. Nonetheless, this example illustrates the ensuing discussions arising from the postulation of potential biosignatures, and the scientific value that this process presents – especially in terms of better understanding planetary habitability. For example, Bains *et al.* (2021) further explore the habitability of Venusian clouds which could potentially harbour life that acts as the source of observed PH_3. Mars has also been subject to a wealth of biosignature investigation (Banfield *et al.*, 2001; Summons *et al.*, 2011) which is imperative in better constraining the past and present habitability of the planet.

A major driving force for Mars research, historically and today, is the search for evidence of life beyond Earth (Mckay, 1997; Vago *et al.*, 2017). This continued evaluation of life on the red planet has necessitated extensive investigation into Martian biosignatures (Banfield *et al.*, 2001; Cady *et al.*, 2003; Westall *et al.*, 2015). For instance, Ruff and Farmer (2016) evaluate the opaline silica deposits observed in the Gusev crater by the Mars Spirit rover as a potential biosignature. By comparing features captured by the Spirit rover to a hydrothermal discharge channel at El Tatio, Chile, they propose that, owing to remarkable similarities with El Tatio microstromatolites, mm-scale structures in the Martian silica outcrops could be of biological origin. Although, the authors stress that, without further and more in-depth analysis, the biogenicity of observed features is undeterminable – calling for a future rover mission to better assess these silica deposits or, ideally, samples to be returned to Earth for complex laboratory analysis. This assertion (*i.e.* that present evidence was insufficient to irrefutably determine a biotic origin) serves to reemphasise the extensive caution and scrutiny necessary to critically evaluate potential biosignatures as undisputable evidence of extra-terrestrial life (Neveu *et al.*, 2018), a trial that Martian biosignatures are no stranger to (McMahon and Cosmidis, 2021). Regardless, this example of an *in situ* investigation of a potential Martian biosignature presents valuable insights into Martian silica deposits, which are prime targets for preserving signs of life and habitability information (McMahon *et al.*, 2018), and encourages further research to be performed regarding the preservation of biosignatures in siliceous hydrothermal systems – an area that the present project will assist in. Additionally, on top of *in situ* observations (*e.g.* by rovers (Webster *et al.*, 2015)) and remote observations (*e.g.* by Earth-based telescopes (Krasnopolsky *et al.*, 2004; Sparks *et al.*, 2012)), there is an additional valuable resource

permitting the direct investigation of potential Martian biosignatures (as well as other aspects of habitability (Lee *et al.*, 2018)) – Martian Meteorites (Gibson *et al.*, 2016; McSween, 2019).

1.3 Martian Meteorites

1.3.1 Meteorites on Earth

There are over 60,000 known meteorites on Earth (Gattacceca *et al.*, 2020) and researchers have investigated them for centuries (Lipschutz and Schultz, 2014). The majority of currently known meteorites are fragments of asteroids (Farinella *et al.*, 1993) residing in the asteroid belt that, through sometimes complex and dynamical routes (Morbidelli and Gladman, 1998), intersect with Earth. Meteorites provide the unique ability to directly investigate their parent bodies, since complex laboratory analyses are possible. For example, King *et al.* (2017) describe how they were able to collate and evaluate the mineral compositions of carbonaceous chondrite meteorites, as determined by X-ray crystallography. They highlight that the investigated meteorites range from consisting of partially, to almost entirely, hydrated minerals as a result of aqueous alteration. This obvious and abundant evidence of aqueous alteration provides invaluable insight into the presence, identity, and abundance of water on the parent asteroids. Findings such as this led to, and support, the hypothesis that water on Earth may have originated from asteroids (Morbidelli *et al.*, 2000; Alexander *et al.*, 2012). This example shows the scientific power of terrestrial laboratory analysis of meteorites, and how they can be used to better understand our Solar System. However, meteorites on Earth do not solely originate from asteroid fragments. Instead, meteorites can reach Earth from a range of other planetary bodies in the Solar System, *e.g.* via ejection from impact events (Nyquist *et al.*, 2001), even including samples believed to originate from Mars (McSween, 1994).

A subset of meteorites, currently consisting of over 260 individual rock samples (Gattacceca *et al.*, 2020), are believed to be Martian (McSween, 1994). The evidence for a Martian origin includes: crystallisation ages (McSween, 1994), trapped gas compositions (Bogard and Johnson, 1983; Marti *et al.*, 1995), and characteristic oxygen isotope ratios (Clayton and Mayeda, 1996). Although, McSween (1994) highlights that the young crystallisation ages (Geiss and Hess, 1958) of the igneous meteorites (signifying recent volcanic activity) would merely constrain the meteorites to a large planetary body – not specifically Mars. Additionally, as summarised by Jones (2015), there exists long running debate and

controversy surrounding the actual crystallisation ages of the shergottite meteorites – which further lessens the weight of crystallisation ages as evidence in deciding a Martian origin. In contrast, much more conclusive evidence in initially suggesting a Martian origin resided in the trapped gas compositions and isotopic ratios where, as shown by Marti *et al.* (1995), the trapped gasses in shergottites strongly resembled the Martian atmosphere as measured by the Viking Martian landers (Owen *et al.*, 1977). Following such lines of evidence, most notably characteristic oxygen isotope ratios and abundances (Franchi *et al.*, 1999), it is reasonable to assume that the meteorites currently identified as Martian are likely to be so. Despite all being classified as Martian meteorites, these rocks are commonly separated into three categories – the Shergottites, the Nakhlites, and the Chassignites (the SNC meteorites) (Jones, 2015).

1.3.2 Classification

1.3.2.1 Shergottites

The most numerous (The Meteoritical Society, 2021) group of the Martian meteorites is the shergottites. They are predominantly basaltic, olivine-phyric, or poikilitic igneous rocks (Udry *et al.*, 2020) that are mainly comprised of olivine, pyroxene, and maskelynite (McSween, 2015). They are categorised based on their relative incompatible trace element compositions (Udry *et al.*, 2020) into depleted, intermediate, and enriched shergottites. Their igneous crystallisation ages are subject to much discussion, owing to radiometric dating techniques giving different ages depending on the isotopes used (Jones, 1986, 2015; Bouvier *et al.*, 2005). For example, Bouvier *et al.* (2009) interpret Pb-Pb isochron data to give an igneous crystallisation age of roughly 4.1 to 4.3 Ga for the shergottites. However, as they even acknowledge, Rb-Sr, Sm-Nd, Lu-Hf, and U-Pb isochron data indicate much younger ages for the shergottites, with the majority from the late Amazonian period (Jones, 2015; Udry *et al.*, 2020). Although contested by Bouvier *et al.* (2009), arguing that the young ages calculated by many isochron data indicate a resetting event, the Amazonian ages are generally accepted to represent the true igneous crystallisation ages of the shergottites (Brennecka *et al.*, 2014; Udry *et al.*, 2020; Váci and Agee, 2020). Thus, the shergottites provide a wealth of information on the Amazonian period of Mars. However, whilst the shergottites give important insights into the water content of the Martian interior (Usui *et al.*, 2012; McCubbin *et al.*, 2016; Hu *et al.*, 2020), another group of meteorites potentially offers much more in terms of direct habitability information (Lee *et al.*, 2018) – the nakhlites.

1.3.2.2 Nakhlites

The second most numerous (The Meteoritical Society, 2021) grouping of the Martian meteorites is the nakhlites. They represent a group of igneous clinopyroxenite cumulates which contain varying quantities of olivine (Treiman, 2005), and are believed to have igneous crystallisation ages of around 1.3 Ga (Nyquist *et al.*, 2001), as determined by multiple radiometric dating techniques. Thus, the nakhlites also sample the Amazonian period of Mars' history. Additionally, Ar cosmogenic exposure data shows that many of the nakhlites have similar ejection ages of around 11 Ma (Cohen *et al.*, 2017), suggesting that they are launch-paired meteorites that were ejected by a singular impact event. Furthermore, the nakhlites host the greatest suite of water alteration products among the Martian meteorites (Lee *et al.*, 2015). Investigation of these alteration products allows for strong insights into the presence and identity of Martian water (Treiman *et al.*, 1993), which is crucial in better understanding the past and future habitability of Mars (Cockell *et al.*, 2016).

These alteration products, collectively referred to as iddingsite, include hydrous silicates, iron oxides, and iron oxyhydroxides (Lee *et al.*, 2018) and were originally believed to have formed from water on the nakhlite parent body (*i.e.* Mars) based on mineralogical and petrological evidence (Gooding *et al.*, 1991). Accordingly, they potentially allow insights into the characteristics and longevity of past Martian water. For example, Borg and Drake (2005) concluded that iddingsite in Lafayette and Yamato 000593 (both nakhlites) likely formed at roughly 633 Ma, as determined by the weighted average of both Rb-Sr and K-Ar radiometric ages. This suggests that sufficient liquid water to cause this degree of aqueous alteration was present in the Martian crust as late as 633 million years ago – providing constraints and insights into the longevity of the Martian hydrosphere. Furthermore, the formation age of the iddingsite also supports the Martian origin of the altering aqueous solution by pre-dating the believed 11 Ma ejection (Cohen *et al.*, 2017) of the meteorites from the Martian surface. Further, Lee *et al.* (2015) highlight that iddingsite in the nakhlites can be interrogated to investigate the temperature, composition, pH, and redox potential of the Martian water responsible for the aqueous alteration (Treiman *et al.*, 1993; Bridges and Schwenzer, 2012) – all of which, including longevity (Cockell *et al.*, 2012), are potentially vital in discerning the habitability of the Martian crust (Brack *et al.*, 2010; Schuerger *et al.*, 2012). Thus, the nakhlites serve as a key probe into Martian habitability by detailing the conditions of the Martian water that they interacted with. There is another group of

meteorites believed to have potentially originated from the same location on Mars as the nakhlites – the chassignites (Nyquist *et al.*, 2001; McCubbin *et al.*, 2013).

1.3.2.3 Chassignites

The third category, despite not being the third most numerous (The Meteoritical Society, 2021), of the SNC meteorites is the chassignites. They are igneous olivine- and chromite-bearing dunites (Udry and Day, 2018). They, like the nakhlites, are believed to have igneous crystallisation ages of around 1.3 Ga (Nyquist *et al.*, 2001) (based on radiometric dating techniques), again sampling the Amazonian period. The similar crystallisation ages, concurrent ejection ages of 11 Ma (Eugster *et al.*, 1997; Nyquist *et al.*, 2001), and various compositional similarities (McCubbin *et al.*, 2013) hint at a strong relationship between the nakhlites and the chassignites – leading to the idea that the two groups may even be comagmatic in origin (Mason *et al.*, 1976). This is contested by Wadhwa and Crozaz (1995), concluding that the distribution of trace elements in augites indicates that the two groups, even whilst acknowledging their similarities, were likely not comagmatic. However, McCubbin *et al.* (2013) propose a model involving the addition of Cl-rich fluid to the parent magmas that can account for such differences – once again permitting a comagmatic origin of the nakhlites and the chassignites. This, together with a wealth of other papers (Udry and Day, 2018; Hewins *et al.*, 2020) similarly investigating the petrogenesis of two groups, highlights the potential connection and comagmatic origin of chassignites and the nakhlites, giving good insights into the inner workings of the Martian mantle and magmas. There exists two further sets of Martian meteorites (distinct from the classical SNC categories (Mittlefehldt, 1994; Agee *et al.*, 2013)) that may provide habitability insights – the Polymict Breccia meteorites and, more notably, the famous Alan Hills 84001 meteorite.

1.3.2.4 Anomalous Meteorites

One of the few meteorites identified as Martian that does not fall under the SNC umbrella is the anomalous Alan Hills 84001 meteorite (herein ALH84001). It is an igneous orthopyroxenite cumulate (Udry *et al.*, 2020), therefore distinct from the SNCs. However, as discovered by Clayton (1993), its oxygen isotope ratios are indistinguishable from other Martian meteorites. This, along with other petrographic features also in accordance with other SNCs (Mittlefehldt, 1994), indicates that ALH84001 is Martian in origin. The igneous

crystallisation age of ALH84001, although previously thought to be roughly 4.51 Ga (Nyquist *et al.*, 2001), is determined to be around 4.09 Ga (Lapen *et al.*, 2010), as shown by Lutetium-Hafnium isotope radiometric data. This age is anomalously old compared to the SNCs (Udry *et al.*, 2020), allowing potentially unique insights into a much younger Mars. Although the Polymict Breccia Northwest Africa (NWA) 7034 is now believed to contain material that is even older (Nyquist *et al.*, 2016; Hu *et al.*, 2019). Following ALH84001's connection to Mars, the meteorite was subject to extensive investigation (Gibson *et al.*, 2001) after a paper published by McKay *et al.* (1996) suggested potential evidence of past biological activity.

This paper, as highlighted in a later review by Gibson *et al.* (2001), incited an enormous discussion surrounding the legitimacy of the claim – with much scrutiny, and support, towards the biological origin of the features seen in ALH84001. In the original paper by McKay *et al.* (1996), they propose four main features potentially indicating past biogenic activity – including the observation of carbonate globule structures analogous to microorganisms found on Earth, the carbonate structures that they produce, or even microfossils. However, Bradley *et al.* (1997) contest this finding, explaining that the structures are likely to be lamellar growths (*i.e.* abiotic in origin) and that their segmented appearance is merely an artefact of the conductive coating applied to the samples upon preparation for analysis. Similar abiotic explanations are offered for the other pieces of proposed evidence (Scott, 1999; Golden *et al.*, 2000, 2001), refuting the potential discovery of evidence of past Martian life. It should be noted that McKay *et al.* (1996) do acknowledge that all of the highlighted features in ALH84001 could have inorganic origins. Despite some papers supporting biological origins (Clemett *et al.*, 1998; Thomas-Keprta *et al.*, 2002), the general consensus is that the features in ALH84001 are most likely abiotic (Martel *et al.*, 2012; McSween, 2019). However, the discussion surrounding the ALH84001 meteorite likely paved the way for advances in our understanding of what constitutes as robust evidence of extra-terrestrial life, and reignited interest in Martian biology (McSween, 2019). Subsequently, there potentially remains unextracted habitability information residing in the nakhlites (Lee *et al.*, 2018) – an area that this project will investigate.

1.3.3 Future Work on Habitability

A recent paper by Lee *et al.* (2018), employing a range of analytical methods, strived to further investigate the aqueous alteration of the nakhlite meteorite NWA 817 and its relationship to the other nakhlites. This work successfully achieved its main goal, concluding that the iddingsite within NWA 817 is the most abundant amongst the nakhlites, it was likely aqueously altered with the other nakhlites at roughly 633 Ma, and the altering water was probably of crustal or atmospheric origin. Most interestingly, the paper posed questions about the observed relationship between the composition of iddingsite and the parent nakhlite's stratigraphic position. They found that the bulk iddingsite MgO composition weight% (henceforth wt%) appeared to decrease with increasing eruption age of the host meteorite. This potentially signifies a change in the chemical properties of the altering fluid as it evolved from flowing through the younger, thus closer to the surface, rocks to the older, deeper, ones (Lee *et al.*, 2018). Understanding this relationship may hint at the original stratigraphic position of the meteorites in the nakhlite launch site, and the nature of their alteration (*e.g.* water flowing downwards under the influence of gravity (Lee *et al.*, 2018)). However, they also noted that their observations (*i.e.* bulk rock composition also correlating well with iddingsite composition) could instead be described by a scenario in which the water-to-rock ratios were very low, thus the iddingsite chemistry would be predominantly influenced by the composition of the host rock rather than the altering fluid. This theory can also explain the stratigraphic relationship between the nakhlites because the bulk rock MgO values also decrease with increasing age (and, thus, depth (Lee *et al.*, 2018)). This project will further research in this area, with the aim of better constraining the relationship between the nakhlite iddingsite, the bulk rock, and the radiometric ages – in order to gain insight into Martian crustal water and, thus, Martian habitability.

Specifically, Lee *et al.* (2018) call for further research involving mineral analyses of the iddingsite within additional nakhlite meteorites (since only four nakhlites were considered in the original work) – particularly of nakhlites Yamato 000593 and Yamato 000749 (henceforth Y-000593 and Y-000749, respectively) whose radiometric ages are known (Cohen *et al.*, 2017). Accordingly, this project will further investigate the trends in the nakhlite iddingsite compositions by incorporating new mineralogy data sets containing details of a greater number of nakhlite meteorites, including the two aforementioned meteorites with known ages. On top of expanding upon the bulk iddingsite MgO composition versus the radiometric age data, there may be benefits in considering different

elemental compositions (*i.e.* not exclusively MgO) with the varying age of the meteorites. Additionally, investigating the relationships of iddingsite within not only olivine, but also the veins hosted in pyroxene, may prove beneficial in clarifying the relationship between the whole rock and the iddingsite. It is hoped that this project's work will contribute towards unveiling the true layout of the nakhlite launch site, and the nature of its aqueous alteration. Importantly, better understanding the identity, abundance, and origin of the Martian fluids that altered the nakhlites is imperative in advancing the knowledge of past Martian habitability (Cockell *et al.*, 2016) – a key goal of this project. However, the investigation of Martian meteorites alone may not be sufficient to fully answer many of the remaining questions surrounding Mars, its habitability, and the development of planets in our Solar System. Instead, many have called for the collection and return of samples directly from Mars (MEPAG Next Decade Science Analysis Group, 2008; McSween *et al.*, 2021) – commonly called Mars Sample Return.

1.3.4 Mars Sample Return

Mars Sample Return (MSR) is a series of missions involving the collection, retrieval, and delivery of rock samples from Mars (Muirhead *et al.*, 2020). The current MSR mission represents an international effort, collaboratively run by NASA and the European Space Agency (Zurbuchen and Parker, 2018), that has already begun (Farley *et al.*, 2022). The Perseverance rover has started to collect rock samples for future retrieval from the Jezero Crater (Farley *et al.*, 2022) – a location believed to have once hosted a lake that has since dried up (Fassett and Head III, 2005; Grant and Golombek, 2018; Farley *et al.*, 2022). If all proceeds as planned, the Earth Return Orbiter and the Sample Retrieval Lander are to be launched in 2027 and 2028, respectively, with Martian rock samples returning to Earth as early as 2033 (mars.nasa.gov, 2022). The MSR mission proposes the unique opportunity to investigate Martian rock samples where, unlike Martian meteorites, the full geological context is known – allowing invaluable insight into many remaining questions surrounding Mars, Martian habitability, and the development of life in our universe (McSween *et al.*, 2021).

The MSR mission undoubtedly represents the next big step in planetary science and undeniably presents a great deal of scientific value. The International MSR Objectives and Samples Team (iMOST) outline the most important scientific goals and objectives of an

MSR mission, and how best to utilise such a mission in answering crucial remaining questions surrounding Mars and beyond (Beaty *et al.*, 2019). They highlight that a major objective (one of seven) of an MSR mission will be to investigate the habitability of Mars by interrogating returned samples for insights into, and potentially evidence of, past or current Martian life. They further break this down into three main sub-objectives: 1) the investigation into Martian carbon and its relevance to life, 2) the discovery and interpretation of biosignatures of past Martian life, and 3) the assessment of potential biosignatures of extant Martian life. It is evident that the fulfilment of these three sub-objectives will be vital in answering many remaining questions surrounding the habitability of Mars and the development of life in the universe – clearly highlighting the vast scientific potential of an MSR mission. Moreover, MSR serves to complement the biased Mars geological record from the investigation of Martian meteorites (Udry *et al.*, 2020). Currently, the suite of Martian meteorites represents only the Martian rocks that were hard and resilient enough to survive the harsh journey to reach Earth from the Martian crust (*i.e.* mostly igneous rocks (Udry *et al.*, 2020)). This effectively excludes softer samples, *e.g.* sedimentary rocks (barring some clasts in the Polymict Breccia meteorites (Santos *et al.*, 2015)), regolith, and dust. Whereas, the Perseverance rover can, and most likely will (mars.nasa.gov, 2021), collect and cache such samples – filling crucial gaps in the understanding of Martian geology and Martian habitability (owing to the fact that these rocks are prime targets for the preservation of biosignatures (Bosak *et al.*, 2021)). Already, despite looking at only a few aspects of an MSR mission's scientific goals, the grand scientific value of an MSR mission is apparent. In order to best realise the aims of this mission, important proceeding steps must be taken to ensure the proper handling and analysis of returned samples (Beaty *et al.*, 2019; McSween *et al.*, 2021).

The most relevant aspect of preparation to this project revolves around the second sub-objective outlined in the previous paragraph, *i.e.* the preparation for the accurate interpretation and investigation of biosignatures of past Martian life. As highlighted by the ALH84001 meteorite (Bradley *et al.*, 1997), as well as other examples investigating terrestrial fossils (Allwood *et al.*, 2018), the confirmation of biosignatures as definitive evidence of life is subject to much scrutiny. To compose the most compelling case for legitimacy, it is clear that complex on-Earth analyses (not feasible by rovers or orbiters) are required, preferably involving a range of techniques over multiple complementary lines of evidence (Ohmoto *et al.*, 2008). However, as discussed by iMOST (Beaty *et al.*, 2019), cutting-edge analysis techniques require sufficient development in the preparation, handling,

and analysis of samples before they can be reliably employed to produce accurate and convincing data surrounding Martian biosignatures. One way to develop analytical techniques for this purpose is to investigate strategically chosen Earth rocks that resemble the environments and conditions on Mars (Daly *et al.*, 2021) – *i.e.* terrestrial analogues; an idea that this project will investigate.

1.4 Mars Terrestrial Analogues

1.4.1 Role in Planetary Science

A terrestrial analogue is a site or sample from Earth that resembles features of interest in an extra-terrestrial body (Preston and Dartnell, 2014), *e.g.* the surface of our Moon (Léveillé, 2010) or the Venusian atmosphere (Limaye *et al.*, 2018). The investigation of terrestrial analogues is particularly important in planetary science, providing insights into planetary processes, the preservation of biosignatures, and habitability (Preston and Dartnell, 2014; Neish *et al.*, 2017). Their investigation also presents the opportunity to develop analytical techniques for use in space exploration (Daly *et al.*, 2021). For example, Prieto-Ballesteros *et al.* (2003) investigate the usage of the Tírez lake in Spain as an analogue for the presumed brine oceans of Jupiter's icy moon, Europa. They concluded that the Tírez lake proved useful for better understanding Europa's oceans by potentially assisting in interpreting orbital data obtained by the Galileo space probe and investigating processes related to the formation of the ice layer. Additionally, the terrestrial analogue environment served to propose and represent a potentially habitable niche in the Europan oceans, *i.e.* low temperature vents, due to the presence of sulphate-reducing bacteria and methanogenic archaea in the Tírez lake brines (Prieto-Ballesteros *et al.*, 2003). As such, including many other examples (Preston and Dartnell, 2014; Antunes *et al.*, 2020), terrestrial analogues can greatly assist in the development of space exploration and planetary science by complementing and guiding *in situ* observations. However, Preston and Dartnell (2014) stress that terrestrial analogues merely resemble target locations, *i.e.* they are not perfect representations. Thus, adequate acknowledgment and constant consideration of the differences that may be present in terrestrial analogues is essential when attempting to make inferences surrounding extra-terrestrial bodies. Although, with this being said, Baker (2014) concludes that, whilst analogues alone may be insufficient to fully explain extra-terrestrial occurrences, they serve as powerful resources for planetary scientists to formulate informed hypotheses, facilitating

developments in understanding. Unsurprisingly, Mars has been a prime target for a wide range of terrestrial analogue investigations (Fairén *et al.*, 2010b; Dypvik *et al.*, 2021).

Mars' history is divided into three distinct geological eras with differing environmental conditions and habitability potentials (Fairén *et al.*, 2010b). The three unique geological scenarios necessitate three groups of terrestrial analogues that best represent the features of interest, *e.g.* habitability, in their respective eras. For example, Westall *et al.* (2011) investigated a sample of the roughly 3.5 Ga fossiliferous Kitty's Gap chert from the Pilbara Craton in north-western Australia as an analogue of the preservation of biosignatures in early, Noachian, Mars. Additional examples exist for the remaining two Martian epochs – *e.g.* permafrost in the Dry Valleys of Antarctica as analogues investigating the habitability and preservation of life in Martian ice environments (Gilichinsky *et al.*, 2007; Heldmann *et al.*, 2013) (pertaining to middle Mars), or the dry soils in the Atacama Desert, Chile, as analogues for habitable niches in the hyper-arid present day Mars (Wierzchos *et al.*, 2011; Aerts *et al.*, 2020). Investigations of Martian habitability and preservation of biosignatures via terrestrial analogues serve to guide and inform the collection and analysis of samples returned from Mars for the maximum probability of discovering and confirming the observation of life. The following section will introduce the Rhynie chert from Scotland and discuss this project's use as a Mars analogue.

1.4.2 Rhynie Chert

The Rhynie chert site, discovered around 1912 (Mackie, 1914), samples a roughly 410 Ma (Mark *et al.*, 2011; Parry *et al.*, 2013) hot spring system near the village of Rhynie in Aberdeenshire, Scotland (Garwood *et al.*, 2020). Hydrothermal activity was responsible for the release of siliceous sinters which, over an extended period of time, formed cherts (Rice *et al.*, 2002). Most notably, the cherts host a vast array of exceptionally well-preserved fossils of the Devonian biota, formed by siliceous permineralization (Trewin and Rice, 1992; Rice *et al.*, 2002). For example, Kidston and Lang (1921) identified and detailed multiple sporophyte plant species, the presence of fungi, and the inclusion of algae preserved within the Rhynie chert. These investigations paved the way for many developments in terrestrial botany (Wellman, 2019). Further work on the Rhynie chert has revealed fossils of arthropods (Fayers and Trewin, 2002), lichens (Taylor *et al.*, 1997), and insects (Whalley and Jarzembowski, 1981), amongst others (Strullu-Derrien *et al.*, 2019). Additionally, Poinar *et*

al. (2008) described the discovery and identification of the first non-arthropodan animal preserved in the Rhynie chert, a nematode worm. Their work describes the oldest known undisputed fossils of nematode bodies and, owing to the exceptional preservation of nematodes at all stages of life within parent plant tissue, may even sample some of the earliest interactions between plants and terrestrial animals. These examples highlight the remarkably pristine preservation of fossils in the Rhynie chert via rapid silicification, and the rare insights that this allows into primeval terrestrial life on Earth (Kenrick *et al.*, 2012). It is clear that the Rhynie chert has significant potential to function as a terrestrial analogue investigating the preservation of biosignatures in Martian hydrothermal systems (*e.g.* hydrothermal vents in Martian impact craters (Turner *et al.*, 2016)).

The value of the Rhynie chert as a Mars analogue has been previously recognised (Preston and Genge, 2010; Qu *et al.*, 2015). However, the research surrounding this usage of the Rhynie chert is presently lacking. For example, Preston and Genge (2010) investigated the Rhynie chert via Fourier transform infrared spectroscopy (FTIR) with the goal of identifying preserved biomolecules whilst relating this work to the investigation of preserved Martian biosignatures. However, they conceded that, despite confirming the presence of infrared bands potentially pertaining to biomolecules, neither the exact identity nor the concentration of the biomolecules was determined – highlighting the limitations of this method. Furthermore, they acknowledged that contamination could be responsible for many of the key bands observed – calling for further research in this area to better ascertain the identity and origin of such preserved biomolecules. Qu *et al.* (2015), utilising a combination of Raman spectroscopy and micro-FTIR, later expanded upon this work on investigating the identity and origin of preserved organic material. Their analytical strategy, whilst certainly providing valuable progress concerning the unravelling of preserved organic matter, merely represents one avenue of investigation (*i.e.* ultrastructural features of carbon chains) – leaving more work to do on the Rhynie chert as a Mars analogue. Moreover, these works focus on techniques best suited for *in situ* observations and analysis (Tarcea *et al.*, 2008; Edwards and Christensen, 2013; Rull *et al.*, 2021) (*e.g.* on surface rovers), effectively excluding the interrogation of the Rhynie chert as an analogue for the complex laboratory analyses that Martian hydrothermal rock samples returned in an MSR mission would be subject to (Beaty *et al.*, 2019). This project will serve to build upon research in this area by employing a high-resolution analytical pipeline in the identification and interrogation of the siliceously-preserved biosignatures. To complement this work on the Rhynie chert, this project will also investigate fossil samples from a Mars terrestrial analogue site which is

often likened to a modern-day analogue of the Rhynie chert hot spring (Channing and Edwards, 2009) – the Yellowstone National Park hydrothermal systems.

1.4.3 Yellowstone

The Yellowstone National Park encompasses a unique volcanic field with extensive volcanic activity over the last 2.1 million years located in Wyoming, America, that is still geothermally active (Christiansen, 2001). Yellowstone comprises over 10,000 hydrothermal features ranging from mud pots to geysers, displaying an unmatched diversity in physical and chemical conditions (Hurwitz and Lowenstern, 2014). The most numerous of the hot springs are those that deposit silica sinters (Walter and Des Marais, 1993), which are known for their ability to preserve evidence of life (Jones, 2021). For instance, a recent review by Tank *et al.* (2017) highlights the in-depth investigations on the microbial mats situated in the alkaline, siliceous hot spring environments of Mushroom Springs and Octopus Springs. The work on these microbial mats, *e.g.* a paper by Huber *et al.* (1998) on bacteria proliferating at temperatures upwards of 80 °C and in low salinity environments, serves to further our understanding of the ability of life to persist in such extreme conditions (*i.e.* hydrothermal vents), providing important insights into the boundaries of life. This abundance of hydrothermal activity and the present extremophile biota has led to Yellowstone being an established Mars terrestrial analogue site (Walter and Des Marais, 1993; Bishop *et al.*, 2004) relevant to hydrothermal systems.

Yellowstone hot spring systems have been utilised to investigate the preservation of biosignatures in analogues Martian hydrothermal systems. For example, Hellman and Ramsey (2004) used a combination of remote detection techniques (*i.e.* a spaceborne radiometer and an airborne spectrometer) with context provided by *in situ* investigations to scrutinise hot spring environments in Yellowstone. They demonstrate the ability and effectiveness of multiple analytical techniques in determining the state of the hydrothermal vents (*i.e.* active or extinct), distinguishing the location and abundance of hydrothermally altered minerals, and detecting the presence of extremophile bacteria inhabiting the hot springs. Guidry and Chafetz (1999, 2003) also investigated the siliceous sinters of Yellowstone. They used scanning electron microscopy, amongst other techniques, to investigate the preservation of biosignatures in the silica sinters in multiple hydrothermal sites – finding ample evidence of well-preserved life in the form of silicified stromatolites,

a variety of silicified microbial features, and opal-A deposits (coined “shrubs”) that are host to fossilised bacteria. The works described above have important implications in the search for preserved life on Mars by demonstrating how an analytical toolkit could be used to identify and interrogate such biomarkers in an analogous Martian hydrothermal environment. This project will expand upon this idea by employing an analytical pipeline on Yellowstone fossil samples in order to inform the analysis of returned Martian samples (regarding preserved biosignatures) and evaluate and improve the pipeline’s effectiveness.

This concludes the first chapter of this thesis which served to introduce the main aim of this research and detail the background literature. The following chapter (Materials and Methods) will describe the methodology performed throughout this project – including descriptions of the samples used and precisely how techniques were employed in their preparation and investigation.

2. Materials and Methods

2.1 Samples

Unpublished nakhlite energy-dispersive X-ray spectroscopy (henceforth EDX) data, collected by Sammy Griffin, were included in this project concerning iddingsite in Y-000593 (127-A), Nakhla (USNM), Y-000749 (64-A), Yamato 000802 (36-A) (henceforth Y-000802), NWA 998 (UG-1), Miller Range (MIL) 90030 (62), MIL 090032 (108), and MIL 090136 (50). The codes in parentheses immediately following each meteorite are identifiers for the specific sample of the respective meteorite. This was augmented by unpublished data collected by James Day concerning the Y-000802 (50) bulk rock. Appendix 1 details the collection of these unpublished nakhlite data.

A fossiliferous rock sample of the Rhynie chert was supplied by the University of Glasgow's Hunterian Museum. This sample was a fragment of the 926-gram GLAHM 132384 Rhynie chert collection item, known to have originated from roughly 74 – 86 cm above the base of the bed as part of a trench sequence, belong to the Middle Old Red Sandstone lithology, and contain fossilised *Asteroxylon* plant material. The Hunterian Museum also supplied two fossiliferous rocks samples from the Yellowstone National Park. The samples were GLAHM Pb2152 (henceforth YellowstoneA), a sample originating from the fossil forest ridge in Yellowstone known to contain a preserved leaf of *Magnolia spectabilis*, and GLAHM Pb2193 (henceforth YellowstoneB), a sample from Elk Creek, Yellowstone National Park known to host a fossilised sample of *Allantodiopsis erosa*.

2.2 Methodology

2.2.1 Thin Section Preparation

Three standard polished thin sections (*i.e.* of 30 µm thickness) were prepared from the Rhynie sample (hereafter Rhynie1, Rhynie2, and Rhynie3) by the Thin Section and Sample Preparation Facility at the University of Edinburgh. Sample preparation facilities available at the University of Glasgow were utilised to produce three standard polished thin sections (30 µm thick) from YellowstoneA (hereafter Yellowstone1, Yellowstone2, and Yellowstone 3) and one standard polished thin section from YellowstoneB (hereafter Yellowstone4).

These thin sections were then subject to initial characterisation by the analytical pipeline – starting with optical microscopy.

2.2.2 Optical Microscopy

Optical microscopy utilises a series of lenses to focus and magnify light from a sample (Dokland, 2006). On top of standard magnified imaging, light filters can allow either plane polarised light or cross polarised light to pass through – permitting deeper insight into qualitative mineralogy (Treiman, 2005) – and reflected light can be used, instead of transmitted light, to tell if features are exposed to the surface or buried below encapsulating minerals (which is important for further analyses). Additionally, modern optical microscopes are computer assisted (zeiss.com, 2022) – permitting functions like z-stacking (*i.e.* images at varying focus depths to detail 3-dimensional morphology) and collages (*i.e.* a series of adjacent images stitched together digitally to image larger areas at a chosen magnification). However, optical microscopy is typically limited to initial, qualitative, characterisation of samples due to its achievable resolution (Vernon-Parry, 2000). This is because optical microscopy employs visible light (roughly 400 – 800 nm wavelength) where, as described by Abbe's equation (Equation 1) for determining the resolution of an optical system, it is evident that such large wavelengths restrict the maximum achievable resolution (to typically around 200 nm for conventional optical microscopy (Huang, 2010)).

$$d = \frac{0.612\lambda}{NA} \qquad \text{Equation 1}$$

Where d = resolution (nm)

λ = wavelength (nm)

NA = Numerical Aperture

Despite this resolution drawback, optical microscopy is used widely in planetary science research (Treiman, 2005; McLoughlin *et al.*, 2019).

In the present project, all seven of the thin sections (Rhynie1-3 and Yellowstone1-4) were inspected under the computer-assisted ZEISS optical microscope at the University of Glasgow (fitted with an Axiocam 305 color camera). Fossils were captured at varying higher magnifications (typically 10x, 40x, or 63x magnification) and computer-assisted functions (*i.e.* z-stacks and collages) were utilised. Fossils determined to be adequately close to the

surface were chosen to be further investigated by the analytical pipeline – starting with molecular characterisation by Raman spectroscopy.

2.2.3 Raman Spectroscopy

Raman spectroscopy uses the scattering of light corresponding to changes in molecular vibrational modes which result in a change in polarizability (Smith and Dent, 2019). A sample is irradiated by a (typically visible) monochromatic laser which causes the excitation of molecules from their electronic ground state to a virtual energy state (Smith and Dent, 2019). Since this virtual energy state is not stable, the molecule soon drops back down to the electronic ground state – reemitting a photon in the process (Colthup *et al.*, 1975) (*i.e.* scattering). The vast majority of the time, this scattering will be elastic – *i.e.* the molecule will return to the original vibrational energy state in the electronic ground state (Colthup *et al.*, 1975) (thus the emitted photon is of the same energy as the incident photon). This is called Rayleigh scattering (Ferraro *et al.*, 2003). A small proportion of the time, the molecule will instead relax to a different vibrational state (either higher or lower in energy than original vibrational state) in the electronic ground state (Colthup *et al.*, 1975) – *i.e.* inelastic scattering can occur. If the molecule relaxes to a higher energy vibrational state in the electronic ground state (and thus the scattered photon is of lower energy than the incident radiation), this is called Stokes scattering (Smith and Dent, 2019). If the opposite occurs (*i.e.* the molecule relaxes to a lower vibrational state and the scattered photon is of higher energy), this is instead called anti-Stokes scattering (Smith and Dent, 2019) (see Figure 3).

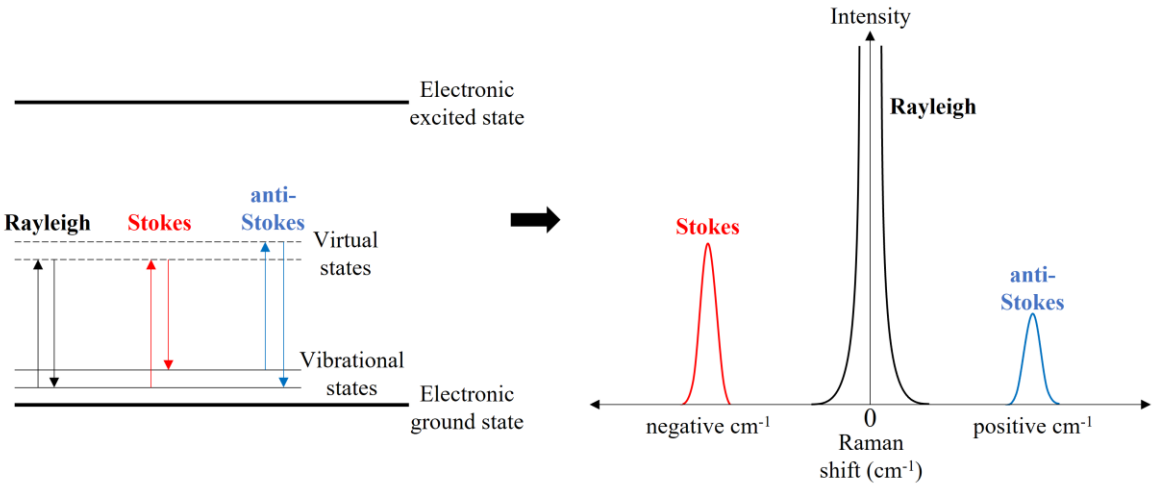

Figure 3 – Left is a simplified energy diagram of Raman-relevant transitions adapted from literature (Ferraro *et al.*, 2003; Smith and Dent, 2019). Right is a simplified Raman spectrum displaying the result of these transitions (where Raman shift is the energy difference of the emitted radiation and the incident radiation). Stokes lines are typically more intense than anti-Stokes lines because the vibrational ground state is more populated than excited ones (as described by the Boltzmann distribution law (Ferraro *et al.*, 2003)).

It is these inelastic scattering events that form the basis of Raman spectroscopy (Colthup *et al.*, 1975). A key selection rule for observed Raman peaks is that the resultant molecular vibration causes a change in the polarizability of the molecule (as opposed to a change in dipole moment for infrared spectroscopy (Ferraro *et al.*, 2003)). By observing the change in energy from inelastically scattered light to the incident light, the energy difference between a molecule's vibrational states can be determined. Since molecules exhibit characteristic energy differences between vibrational states, Raman peaks can be used in chemical identification (Smith and Dent, 2019). As such, Raman allows the investigation into the identity and structure of carbon within a sample – potentially permitting assessment of the biogenicity of carbonaceous material (Edwards *et al.*, 2007; Qu *et al.*, 2015) – contributing to its promising (Tarcea *et al.*, 2008) and burgeoning (Rull *et al.*, 2017; Uckert *et al.*, 2021) usage in planetary science.

One of the three Rhynie chert thin sections and two of the four Yellowstone thin sections were chosen to undergo further interrogation via the analytical pipeline – namely Rhynie3, Yellowstone1, and Yellowstone2. The thin sections were inspected on a Renishaw InVia Raman laser spectrometer at the University of Glasgow. Following the guidance of previous Rhynie chert Raman work by Qu *et al.* (2015), Rhynie3 was irradiated using a 514 nm laser with a grating of 2400 g/mm, and data was collected over a spectral range of roughly 404 – 1712 cm^{-1} (to encapsulate both the chert peak situated at roughly 465 cm^{-1} and the key carbonaceous material peaks centred at roughly 1350 cm^{-1} and 1600 cm^{-1}). Yellowstone1 and Yellowstone2 were also inspected under these same conditions (including the 514 nm laser). Individual point spectra were initially obtained with varying settings to calibrate the optimal acquisition parameters for the specific sample and area – with typical optimal settings being a laser power of 1 or 5%, an exposure time of 3, 5, or 10 s, and collecting 1 – 3 accumulations. Following methodology outlined by Kouketsu *et al.* (2014), Renishaw's Windows-based Raman Environment (WiRE) Raman analysis software was used to remove the baseline of acquired spectra by a linear subtraction over the 1000 – 1750 cm^{-1} range, and peak deconvolution was performed (via the peak fitting capabilities of the WiRE software) using a mixed Gaussian-Lorentzian peak shape. All spectra were acquired whilst utilising the software's ability to compensate for cosmic background radiation. Raman spectral maps were captured (employing previously determined optimal acquisition conditions and baseline removal settings) of key areas of interest. It should be noted that spectra boasting relevant peak intensities residing within 5% of the extremes were excluded from the maps (leaving only 5 – 95% peak intensity spectra) in order to improve the accuracy of the maps.

Overall, this was done to complement subsequent high-resolution imaging and elemental composition analysis by scanning electron microscopy (SEM).

2.2.4 Scanning Electron Microscopy

SEM utilises signals produced by an electron beam that is scanned across a sample surface (Zhou *et al.*, 2006). Backscattered electrons (high energy electrons produced from elastic collisions) and secondary electrons (lower energy electrons emitted in inelastic interactions) are two primary signals that are used to image the surface of the sample, with secondary electrons being more used for topographical information due to their greater surface sensitivity (Zhou *et al.*, 2006) (see Figure 4). Backscattered electrons and characteristic X-rays (produced when an atom's outer shell electron drops to fill a hole that was produced by the electron beam in a lower energy shell) both provide compositional and chemical information, since their responses are dependent on the interacting atom (Zhou *et al.*, 2006). Thus, SEM allows imaging of a surface and the investigation of its elemental composition.

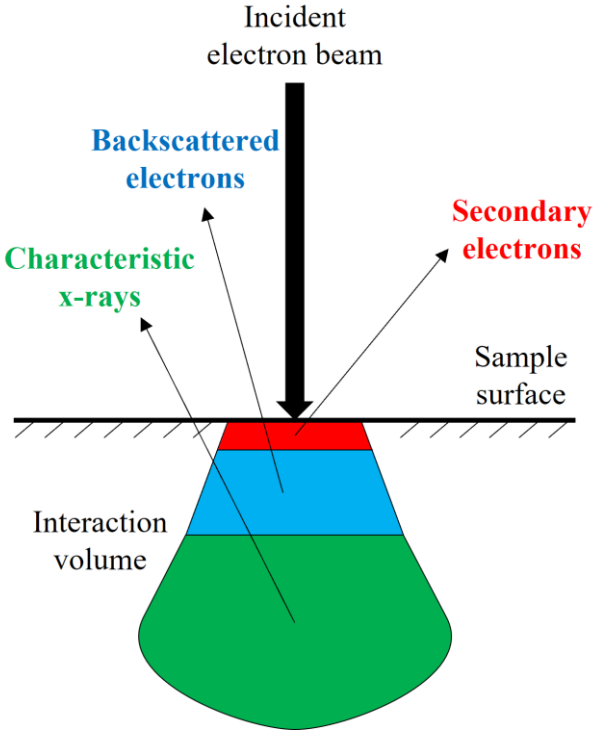

Figure 4 – Simplified diagram illustrating three of the SEM-relevant responses of a sample upon irradiation by the incident electron beam (adapted from literature (Vernon-Parry, 2000; Zhou *et al.*, 2006)). The relative depth below the surface that each signal has enough energy to escape the sample and be detected from is suggested by their colour – with red for secondary electrons, blue for backscattered electrons, and green for characteristic x-rays. This clearly highlights why the lower-energy secondary electrons are more surface sensitive than the higher-energy backscattered electrons (and are thus more used for imaging topography).

A major advantage of SEM over optical microscopy, on top of providing elemental analysis, is the achievable resolution (Vernon-Parry, 2000). This is due to the fact that, by accelerating the electrons in the SEM's electron beam to energies of 2 – 1000 keV, the incident beam's

wavelength (0.027 – 0.0009 nm) is much smaller than that of the visible light (roughly 400 – 800 nm) used in optical microscopes (Vernon-Parry, 2000). Therefore, by Abbe's equation (Equation 1), it is evident that the much smaller wavelength employed in the SEM will result in a much better resolution (Zhou *et al.*, 2006). The typical SEM can achieve resolutions of up to around 1nm, whereas conventional optical microscopy is limited to around 200nm (Vernon-Parry, 2000; Zhou *et al.*, 2006; Huang, 2010). Owing to its high resolution and compositional analysis capabilities, SEM is a valuable technique for planetary science research – *e.g.* see D'Elia *et al.* (2017).

Rhynie3 was initially coated with a roughly 15 nm gold (with trace amounts of palladium) protective layer using sample preparation facilities available at the University of Glasgow – however, after trials in obtaining high-resolution images and compositional information, this coating was removed. Both Rhynie3 and Yellowstone1 were then coated (utilising the same facilities as above) with roughly 20 nm of carbon which was used for subsequent data collection. Copper tape was applied to both ends of the thin sections, that connected to the metal mount, before the samples were loaded into either the Sigma ZEISS SEM or the FEI Quanta 200F Environmental SEM (both at the University of Glasgow). This, on top of the added conductive carbon layer, served to allow current produced from the SEM's electron gun to run off – *i.e.* acted to prevent, or at least reduce, surface charging. Following loading of the coated, mounted, and taped samples, a high vacuum was pulled in the sample chamber – preparing the sample for analysis. After focus and attenuation were properly tuned, the typically 20 kV beam was operated to obtain backscattered electron (henceforth BSE) and secondary electron (henceforth SE) images of fossils. For compositional information, the Sigma ZEISS SEM's attached Oxford Instruments X-Max silicon-drift EDX detector was operated by AZtec microanalysis software. Like for the Raman spectra, initial EDX spectra were obtained under varying conditions to determine the optimal acquisition settings – with typical optimal settings being an accelerating voltage of 20 kV, a working distance of either 8.0 or 8.6 mm, 500000 counts, a process time of 3-5s, and a dwell time of 100 µs. Once determined, these acquisition parameters were used to produce elemental area maps. Although, it is important to note that the software's ability to automatically remove carbon signals corresponding to the 20 nm carbon coating was disabled for some map acquisitions in order to gain better insight into the distribution of carbon in the preserved fossils. Following this, using the BSE images as a guide, pinpointed and characterised areas of interest were milled out to electron transparency by a focused ion beam (FIB) in preparation for further investigation in the analytical pipeline.

2.2.5 Focused Ion Beam

The FEI Nova Nanolab 200 FIB, available at the University of Glasgow, was operated (using XT microscope control software) to extract two electron-transparent slices from Rhynie3 (hereafter Rhynie3 Slice1 and Rhynie3 Slice2) corresponding to a single fossil. The thin section was inserted into a sample mount (nestled atop a bed of copper tape) and subsequently inserted into the FIB's sample chamber – where a high vacuum was then pulled. After locating the fossil, the Sidewinder electron beam (with a 1.4 ms dwell time) was used to deposit a thin (roughly 400 nm) layer of Pt on the surface – demarcating the two areas (roughly 10 µm long) on the fossil that would then be milled out to electron transparency. The FIB's ion beam was then used to deposit a thick layer of Pt on the surface of these demarcated areas in order to protect the surface of the sample from the following milling by the ion beam. Next, the Ga ion beam was used to mill points into the surface of Rhynie3, flanking each denoted area, in order to guide the automated milling process. This would thin the slices down to roughly 2 µm thickness, 15 µm in length (longer than the delineated 10 µm length to provide a buffer, since ends are typically shortened during milling), and roughly 10 µm deep into the surface. Subsequent milling (from 2 µm down to the roughly 100 nm thickness for electron transparency) was then performed manually with decreasing beam voltages (starting with a 30 kV ion beam) to provide better control when thinning the slices. Rhynie3 Slice1 and Rhynie3 Slice2 were then lifted from Rhynie3 (using the attached OmniProbe 100) and inserted into a separate mount.

The Helios Plasma FIB (also available at the University of Glasgow) was then utilised, following similar methodology to that outlined for the FEI Nova Nanolab 200 FIB, to mill two further electron-transparent slices from Rhynie3 (henceforth Rhynie3 Slice3 and Rhynie3 Slice4) plus two slices from Yellowstone1 (hereafter Yellowstone1 Slice1 and Yellowstone1 Slice2). It should be noted that, in distinction from the FEI Nova Nanolab 200 FIB, the Helios Plasma FIB employed a Xenon plasma ion beam to mill the samples to electron-transparency instead of a Ga ion beam. The four newly produced electron-transparent slices were then lifted from their respective polished thin sections and transferred to a separate mount. The mounts hosting these slices (Rhynie3 Slice1-4 and Yellowstone1 Slice1-2) were then transferred for inspection by transmission electron microscopy (TEM).

2.2.6 Transmission Electron Microscopy

TEM utilises a transmitted electron beam to characterise a sample (Reimer and Kohl, 2008). The sample must be sufficiently thin (typically <100 nm thick) to allow for the transmission of electrons – *i.e.* samples must be electron-transparent (Lee *et al.*, 2003). Incident electrons experience a range of elastic and inelastic interactions with atoms in a sample (Reimer and Kohl, 2008) (see Figure 5). A TEM image is formed by capturing and interpreting transmitted electrons, where different parts of the sample will scatter electrons to a greater degree than others (*e.g.* heavier atoms versus lighter atoms) – allowing a contrast to be produced that provides in-depth structural and compositional information (Lee, 2010). Energy lost by inelastically scattered electrons can be used to identify the interacting atom (Verbeeck *et al.*, 2005) – forming the basis of electron energy loss spectroscopy (henceforth EELS). When investigating crystalline specimens, electron diffraction patterns may be produced due to diffraction by the atomic lattice – permitting insights into the sample's crystallographic identity (Lee, 2010).

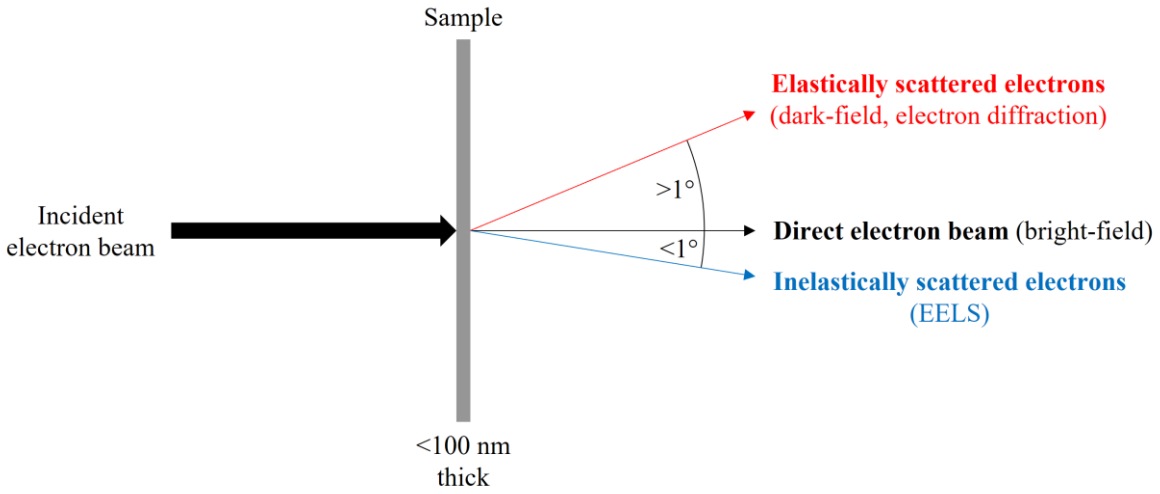

Figure 5 – Simplified diagram of three transmitted signals used in TEM (adapted from literature (Williams and Carter, 2009; Lee, 2010)) with the information they mainly provide in parentheses. Red is elastically scattered electrons – typically scattered at >1° and are mainly used for dark-field images and electron diffraction patterns (for crystalline samples). Black represents the directly transmitted electron beam (*i.e.* unscattered) which allows the production of bright-field images. Blue are the inelastically scattered electrons which are typically scattered <1° and form the basis of EELS (since their lost energy corresponds to atomic information).

By focusing the electron beam into a small 'electron probe' and scanning the beam across a sample, an image of the sample can be constructed – known as scanning TEM (henceforth STEM) (Nellist, 2019). TEM is able to achieve exceptionally high resolutions (down to the atomic scale) due to the high energy electron beam (Daly *et al.*, 2020) (typically 200 keV), as described by Abbe's equation (Equation 1). Importantly, EELS is particularly useful for detecting and identifying elements of low atomic numbers (*e.g.* carbon (Ahn, 2004)) –

making it an extremely important tool in biosignature investigations. As such, TEM is a technique that also presents much value in the field of planetary science (Daly *et al.*, 2020).

The University of Glasgow's FEI Tecnai T20 TEM was operated to procure bright-field images and electron diffraction patterns from Rhynie3 Slice1 and Rhynie3 Slice2. The mount hosting these slices was loaded into a sample holder which was subsequently inserted into the TEM's specimen chamber – where a vacuum was then pulled. The two slices were then irradiated by the TEM's 200 kV electron beam (where electrons were produced by a LaB_6 filament) and the response observed. This TEM work was done to assess the potential presence of any preserved biogenic material within the Rhynie chert slices to inform and prompt further analysis of the Rhynie chert (and Yellowstone) samples via STEM and EELS.

The mount hosting the four newer electron-transparent slices (Rhynie3 Slice3, Rhynie3 Slice4, Yellowstone1 Slice1, and Yellowstone1 Slice2) was loaded into the sample holder that was subsequently inserted into the University of Glasgow's JEOL ARM 200CF TEM instrument and a vacuum pulled. The 200 kV electron beam (produced using a cold field emission gun electron source) was then operated to acquire dark-field images of the entirety of all four slices and raster-scanned across regions of interest within each sample (*i.e.* STEM) to produce STEM dark-field images of specific features. Furthermore, the attached Gatan 965 Quantum ER spectrometer was utilised to obtain EELS data correlating to these STEM-imaged areas of interest in order to capture the elemental composition of these regions at similarly high resolutions.

2.2.7 Atom Probe Tomography

Although not employed on the analogue samples, atom probe tomography (henceforth APT) was then used in the analysis of the nakhlites. APT is a state-of-the art analytical technique which utilises field-evaporation and time-of-flight analysis to determine the chemical identity and original 3-dimensional position of atoms within a sample (Reddy *et al.*, 2020). An important prerequisite of APT is that the sample must have a needle-like geometry (Reddy *et al.*, 2020) with a hemi-spherical tip of typically <100 nm diameter. APT is usually operated under vacuum to avoid the detection of any extraneous gas molecules, and samples are cooled to roughly 20 – 80 K to minimise thermal-induced interference (*e.g.* surface

migration of atoms prior to evaporation (Gault, 2016; Reddy *et al.*, 2020)). The needle-like samples are then inserted adjacent to an annular electrode within the atom probe. The electrode applies a potential bias of typically multiple keV to the sample, inciting a strong electric field (roughly 10 – 50 V/nm) at the tip (Kelly and Larson, 2012; Reddy *et al.*, 2020). For conductive samples, voltage pulses can then initiate field-evaporation of singular atoms. However, this method is largely ineffective for non-conductive samples (Sijbrandij *et al.*, 1998) (*i.e.* most planetary samples (Daly *et al.*, 2020)). It was later discovered that the addition of a high-pulse-frequency laser (now typically ultraviolet) once again permitted controlled field-evaporation – whereby laser pulses at the tip of the sample cause temperature fluctuations that impart sufficient energy to initiate the field-evaporation of singular atoms (Larson *et al.*, 2013). These now-ionised field-evaporated atoms are then accelerated over a known distance to a position-sensitive detector (Reddy *et al.*, 2020) (see Figure 6). The detector then allows the determination of the initial 'x' and 'y' (*i.e.* lateral) position of an incident ion, via its flight path trajectory (Reddy *et al.*, 2020). The initial 'z' position (*i.e.* depth) of the detected species within the sample is determined by the order of evaporation, where it is assumed that the atoms were evaporated one-by-one, layer-by-layer, such that the initial depth of an ion can be evaluated as the depth of the previous ion plus a calculated depth-increment (Geuser and Gault, 2017). Although, variations in sample geometry and composition can cause deviations from this (Vurpillot *et al.*, 2013). Thus, the initial 3-dimenional positions of atoms within the sample is known.

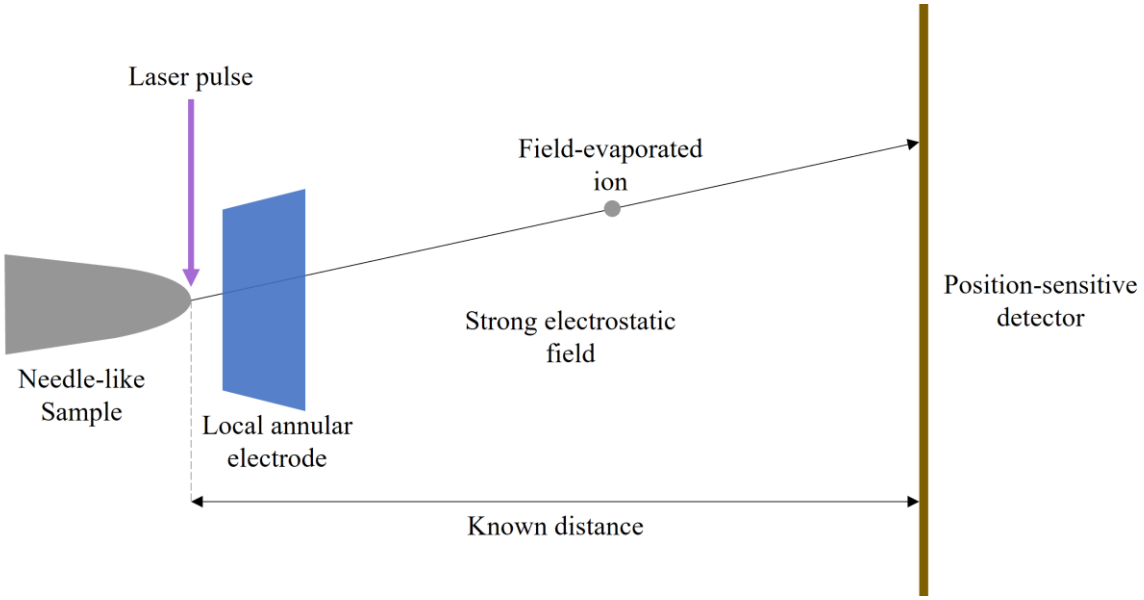

Figure 6 – Simplified illustration of APT field-evaporation of singular species adapted from literature (Saxey *et al.*, 2018; Reddy *et al.*, 2020). Laser pulses (or voltage pulses for conductive samples) incite field-evaporation of singular species which are then accelerated through a strong electrostatic field over a known distance to a position-sensitive detector. This detector, via the field-evaporated ion's flight path trajectory, determines the initial lateral position of the species within in the sample, and the depth within the sample is determined by a calculated depth increment applied after each detection.

Since the timing of a pulse and the time at which a subsequently-evaporated ion reaches the detector are known, it is possible to calculate the time-of-flight for detected ions (Reddy *et al.*, 2020). From this, by time-of-flight analysis, the mass-to-charge-ratio of each ion can be determined. This allows the precise chemical, and even isotopic, identity of atoms within the sample to be evaluated (Reddy *et al.*, 2020). Since both position and chemical identity are known, an isotopically-detailed 3-dimensional reconstruction of the original sample can be made with atomic resolution. Due to all elements being evaporated with equal efficiency (theoretically (Saxey *et al.*, 2018; Daly *et al.*, 2020)) and modern atom probes being able to detect up to around 80% of evaporated ions (Prosa *et al.*, 2014; cameca.com, 2022a), APT is able to produce extremely accurate and high sensitivity models. That is, up to 1 atomic part per million sensitivity (Kelly and Larson, 2012) over a sample volume of up to 100 nm x 100 nm x 1000 nm (Daly *et al.*, 2020). Hence, despite its inherently destructive nature, APT proves to be a valuable tool in the field of planetary science (Daly *et al.*, 2021) – with its quality of maximal information in exchange for minimal destroyed sample.

APT data concerning iddingsite in NWA 817 was reconstructed. This data was previously collected by Luke Daly, operating the CAMECA Local Electrode Atom Probe (henceforth LEAP) 5000XR available at the University of Oxford. Analysis and reconstruction were performed utilising CAMECA's AP Suite 6 software. The first sample (hereafter Nakhlite1) was a volume of NWA 817 iddingsite. The second sample (henceforth Nakhlite2) was an olivine-iddingsite interface also from NWA 817. The sample acquisition and reconstruction conditions for these samples are summarised in Table 1 (constructed following guidance suggested by Blum *et al*. (2017)).

Table 1 – Relevant instrument, sample acquisition, and sample reconstruction information for the nakhlite APT data considered in this project

	Nakhlite APT data	
Specimen	Nakhlite1	Nakhlite2
Instrument	LEAP 5000XR	LEAP 5000XR
Laser wavelength[a]	355 nm	355 nm
Laser pulse energy	100 – 200 pJ (mainly 100 pJ)	80 pJ
Pulse frequency	135 – 175 kHz	200 kHz
Detection efficiency[b]	Roughly 50%	Roughly 50%
Detection rate	0.2 – 0.6%	0.3%
Flight path length	382 mm	382 mm
Meteorite	NWA 817	NWA 817
Brief Description	Iddingsite	Olivine-iddingsite interface
Temperature	50.0K	50.0K
Good hits	2,580,532	38,379,058
Good%	95.6%	97.1%
Reconstruction method	Fixed shank	Voltage
Angle	5	-

"-" represents where information is not applicable
[a] (Peng *et al.*, 2018)
[b] (cameca.com, 2022b)

In summary, the analytical pipeline was mainly employed in the investigation of the Rhynie chert and Yellowstone samples (and partially in the investigation of the nakhlites). The ability of this pipeline to focus into a specific feature of interest with ever-increasing resolution is shown in Figure 7 – a hypothetical utilisation of the pipeline constructed with literature-sourced images.

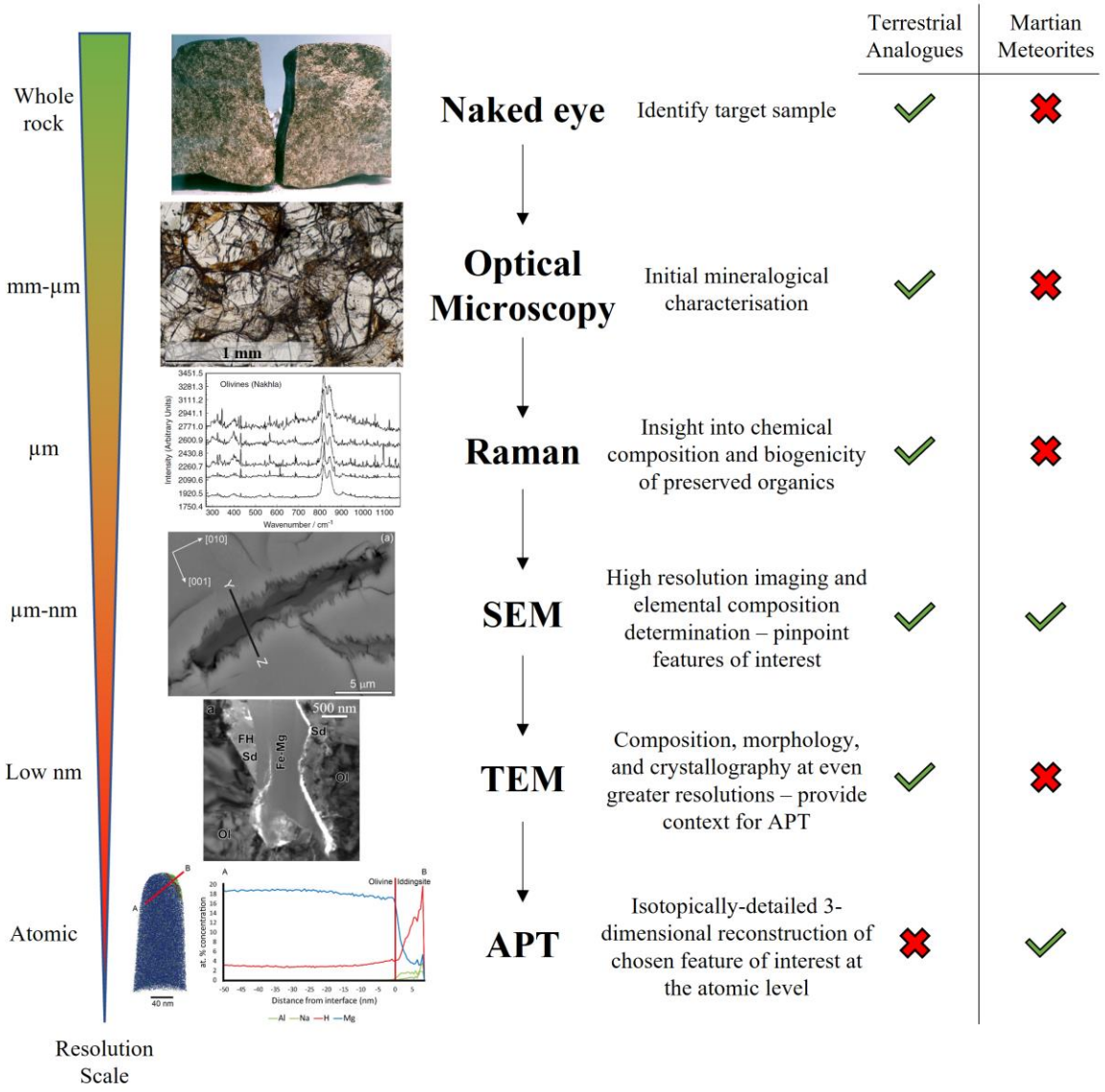

Figure 7 – Illustrative example of the analytical pipeline employed in this project. Tapered bar on the left represents the ever-increasing resolution, highlighting the scientific power arising from the correlative and successive usage of these analytical techniques. Note: the resolution steps in the bar are not to relative scale and are instead representative of the achievable resolution at each step in the pipeline. To the right are exemplar images acquired from literature of nakhlites being investigated by the named analytical technique to the right of the image – representing a hypothetical utilisation of the pipeline. Images from the top are: a photograph of the Nakhla meteorite (credit: NASA photo #S98-04014, (Meyer, 2012)); a transmitted light image of a Nakhla thin section showing mineral composition (credit: (virtualmicroscope.org, 2022)); a 5 – 10 µm spot point-Raman spectra of Nakhla olivine grains (credit: (Rull *et al.*, 2004)); a backscattered electron SEM image of an olivine-hosted iddingsite vein in Nakhla (credit: (Lee *et al.*, 2013)); a bright-field TEM image of a olivine-hosted iddingsite vein in Nakhla, cut along the Y-Z line in the above SEM image (credit: (Lee *et al.*, 2015)); and an APT reconstruction and 1-dimensional concentration diagram of an NWA 817 olivine-iddingsite interface (credit: (Daly *et al.*, 2020)). To the right of this is a brief explanation behind the inclusion of each technique in the workflow, and the information that they can provide. The far-right section summarises which techniques have been involved in the analysis of which samples in this project – where the green check mark represents where the technique was involved and the red cross where not (*e.g.* TEM was involved in this project's terrestrial analogue analyses, but not in the Martian meteorite work).

This concludes the Materials and Methods chapter of the thesis, where the precise methodology undertaken as part of this project was outlined. The subsequent chapter, Results, will report the results obtained via this work.

3. Results

3.1 Martian Meteorites

3.1.1 Nakhlite Composition

The chemical compositions of bulk nakhlites and their olivine-hosted veins of iddingsite were compiled from published literature in order to garner deeper insights into the water that interacted with the rocks on Mars. The compilation was then augmented by incorporating a new data set obtained by Sammy Griffin at the University of Glasgow – hereafter referred to as the "new data set". However, the raw data was highly varied – ranging from roughly 8 – 100 total wt%, with values at the extremes corresponding to holes and other minerals, not exclusively iddingsite. Accordingly, the values were systematically reduced to better reflect and represent measurements that pertain to the olivine-hosted iddingsite. Appendix 1 details the filtering of this data set. It is important to note that, for this study, all sulphur was recalculated as SO_2, and all iron recalculated as FeO. The data sources for this compilation are in Table 2.

Table 2 – Data sources for the nakhlite iddingsite and bulk oxide compositions

Meteorite		Author(s)	Host Crystal/ Sample	Measurement Type	Values Taken	Total Values
Lafayette	Vein	Treiman *et al.*, 1993	Olivine	Average	1	
		Kuebler *et al.*, 2004	Olivine	Average (29)	1	
		Changela and Bridges, 2010	Olivine 'gel'	Average (8)	1	
		Hicks *et al*., 2014	Olivine 'gel'	Average	1	4
	Bulk	Boctor *et al.*, 1976	Fusion crust	-	1	
		Lodders, 1998	Bulk	-	1	
		Udry and Day, 2018	Bulk	-	1	3
Y-000593	Vein	Imae *et al*., 2005	Olivine	Representative	2	
		Noguchi *et al*., 2009	Olivine (crack)	Representative	1	
		Hicks *et al*., 2014	Olivine 'gel'	Average	1	
		New data set	Olivine	Average (16)	1	5
	Bulk	Shirai *et al*., 2002	Bulk	-	1	
		Imae *et al.*, 2003	Bulk	-	1	
		Oura *et al*., 2003	Bulk	-	1	
		Udry and Day, 2018	Bulk	-	1	4
Nakhla	Vein	Hallis *et al.*, 2012	Olivine alteration	-	1	
		Hicks *et al.*, 2014	Olivine 'gel'	Representative	1	
		Lee and Chatzitheodoridis, 2016	Olivine	Average (3)	1	
		New data set	Olivine	Average (23)	1	4

Nakhla	Bulk	Prior, 1912	Bulk	-	3	
		McCarthy *et al*., 1974	Bulk	-	1	
		Bunch and Reid, 1975	Fusion crust	-	1	
		Dreibus *et al*., 1982	Bulk	-	1	
		Lodders, 1998	Bulk	-	1	
		Anand *et al*., 2005	Bulk	-	1	
		Udry and Day, 2018	Bulk	-	2	10
NWA 817	Vein	Gillet *et al*., 2002	Olivine	Average (25)	1	
		Sautter *et al*., 2002	Olivine	-	2	
		Hicks *et al*., 2014	Olivine 'gel'	Representative	1	4
	Bulk	Sautter *et al*., 2002	Bulk	-	1	
		Udry and Day, 2018	Bulk	-	1	2
MIL 03346	Vein	Day *et al*., 2006	Olivine	Representative	4	
		Sautter *et al*., 2006	Olivine	-	1	
		Imae and Ikeda, 2007	Olivine	Representative	2	
		Hallis *et al*., 2012	Olivine	-	1	
		Stopar *et al*., 2013	Olivine	Average (5)	1	
		Hicks *et al*., 2014	Olivine 'gel'	Representative	1	
		Daly *et al*., 2019b	Olivine	Average (17)	1	11
	Bulk	Anand *et al*., 2005	Bulk	-	1	
		Day *et al*., 2006	Bulk	Average (20)	1	
		Udry and Day, 2018	Bulk	-	1	3
Y-000749	Vein	Noguchi *et al*., 2009	Olivine	Representative	1	
		Hicks *et al*., 2014	Olivine 'gel'	Representative	1	
		New data set	Olivine	Average (21)	1	3
	Bulk	Imae *et al*., 2003	Bulk	-	1	
		Udry and Day, 2018	Bulk	-	1	2
Y-000802	Vein	New data set	Olivine	Average (25)	1	1
	Bulk	James Day*	Bulk	-	1	1
NWA 998	Vein	Treiman and Irving, 2008	Olivine	-	3	
		New data set	Olivine	Average (3)	1	4
	Bulk	Treiman and Irving, 2008	Fusion crust/ modal calculation	-	2	
		Udry and Day, 2018	Bulk	-	2	4
NWA 11013	Bulk	Udry and Day, 2018	Bulk	-	1	1
MIL 090030	Vein	Hallis and Taylor, 2011	Olivine alteration	Representative	2	
		New data set	Olivine	Average (34)	1	3
	Bulk	Udry and Day, 2018	Bulk	-	1	1
MIL 090032	Vein	Hallis and Taylor, 2011	Olivine alteration	Representative	1	
		New data set	Olivine	Average (28)	1	2
	Bulk	Udry and Day, 2018	Bulk	-	1	1
MIL 090136	Vein	Hallis and Taylor, 2011	Olivine alteration	Representative	1	
		New data set	Olivine	Average (23)	1	2
	Bulk	Udry and Day, 2018	Bulk	-	2	2

"-" used to represent information that was not understood, not clear, or not present in the source publication
"(n)" after Average in Measurement Type denotes that this value was specified as an average of n values
Total Value column sums the subsequent number of values used in succeeding analyses
* This value is an unpublished Y-000802 bulk value from analyses performed by James Day

Following completion of this filtering and incorporation into the compilation, the new average values were used to produce graphs of the bulk rock composition versus the olivine-

hosted iddingsite composition for multiple elements, which are in Figure 8. Supplementary information, including full tables, is available in Appendix 1.

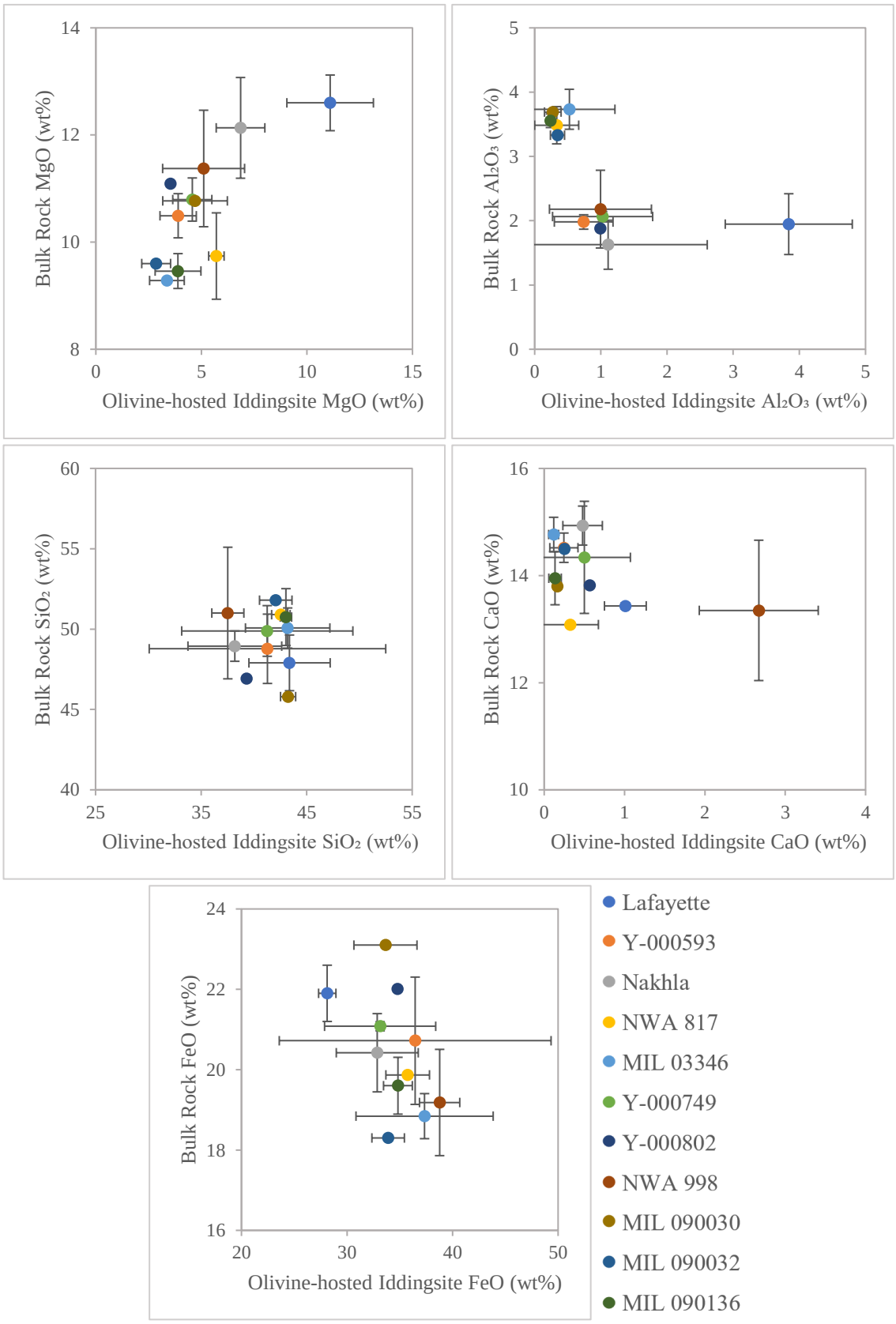

Figure 8 – Graphs of bulk rock composition (wt%) versus olivine-hosted iddingsite composition (wt%) for a group of the nakhlites. The black bars on points within the graphs represent the standard deviation (since the bulk and iddingsite values are produced as averages). Where such bars are not shown, the value is an "average" of one value and thus has no standard deviation, or the standard deviation is zero. Note that the scale of axes is not necessarily the same between graphs, nor necessarily the same on both axes within an individual graph.

Figure 8 reveals a strong positive correlation between bulk rock and iddingsite MgO content and no correlation for Al_2O_3 and CaO. SiO_2 shows little variation and iddingsite FeO decreases as bulk rock FeO increases.

The updated olivine-only iddingsite composition and the bulk rock composition compilations of the nakhlites produced in this project were then plotted against the igneous crystallisation age of the meteorites as calculated by Cohen *et al*. (2017) via Ar-Ar radiometric dating. This was done to investigate the changing composition of iddingsite with depth below the surface (which is suggested by crystallisation age) to better understand the nature of the nakhlite alteration at 633 Ma. Although, Cohen *et al*. (2017) only concerned the crystallisation ages of five of the nakhlites that were considered in this study – namely Lafayette, Y-000593, Nakhla, MIL 03346, and Y-000749. The plots for these meteorites are in Figure 9.

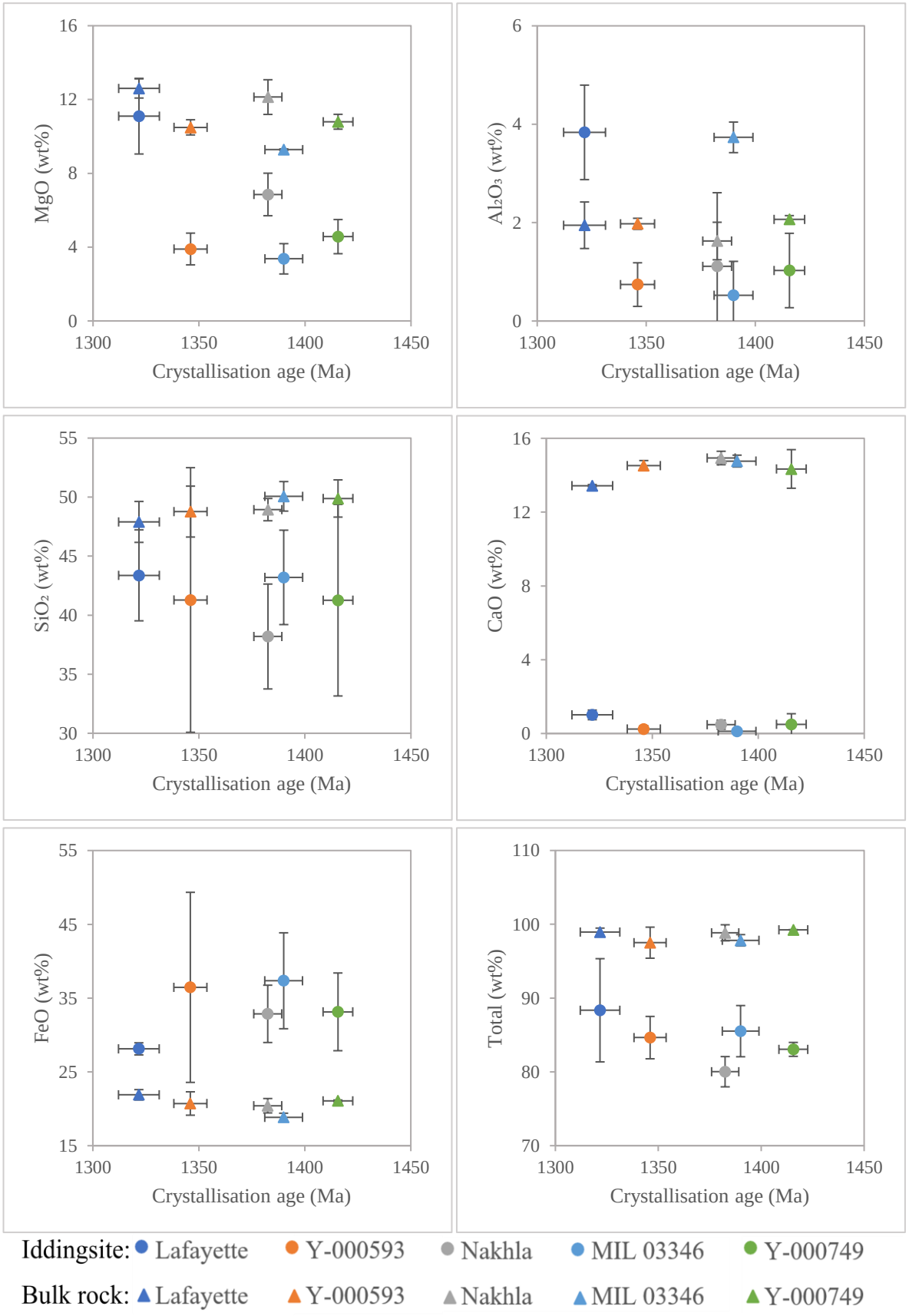

Figure 9 – Graphs of both olivine-hosted iddingsite and bulk rock oxide compositions (wt%) versus igneous crystallisation age (Ma) as determined by Cohen *et al*. (2017). It should be noted that "Total" represents the average of each individual total weight percentage of a quantity (*e.g.* Lafayette bulk rock) – not the summation of each averaged oxide value. The horizontal black bars represent the full external age uncertainty reported by Cohen *et al*. (2017), and the vertical black bars represent the standard deviation (since both the iddingsite and bulk rock composition values are produced as averages). Where such vertical bars are not shown, the value is an "average" of one value and thus has no standard deviation, or the standard deviation is zero. Note that, whilst the x-axis is the same between the graphs, the scale of the y-axis is not necessarily the same for all of the graphs.

Figure 9 shows that both bulk rock MgO and iddingsite MgO have the same relationship with crystallisation age. Whereas Al_2O_3, SiO_2, CaO, and FeO have differing relationships between bulk rock content with age and iddingsite content with age. Bulk rock total wt% stays roughly constant at around 100, meanwhile iddingsite total wt% trends slightly downwards with increasing crystallisation age.

These analyses concerning the oxide composition of iddingsite within the Martian meteorites were then complemented by reconstructing and interrogating nakhlite APT data.

3.1.2 Nakhlite APT Reconstructions

Two NWA 817 iddingsite APT samples (Nakhlite1 and Nakhlite2) were reconstructed and subsequently analysed in order to probe the nature of the nakhlite alteration which carries implications for the habitability of the past environment. The assigned and annotated mass spectra for both reconstructions are in Appendix 2 (Appendix Figure 1 and Appendix Figure 2, respectively). Various isosurfaces were produced to illuminate the relative (density) distribution of water in Nakhlite1 and the differences in elemental concentrations over the olivine-iddingsite interface in Nakhlite2. These isosurfaces are presented in Figure 10 and Figure 11.

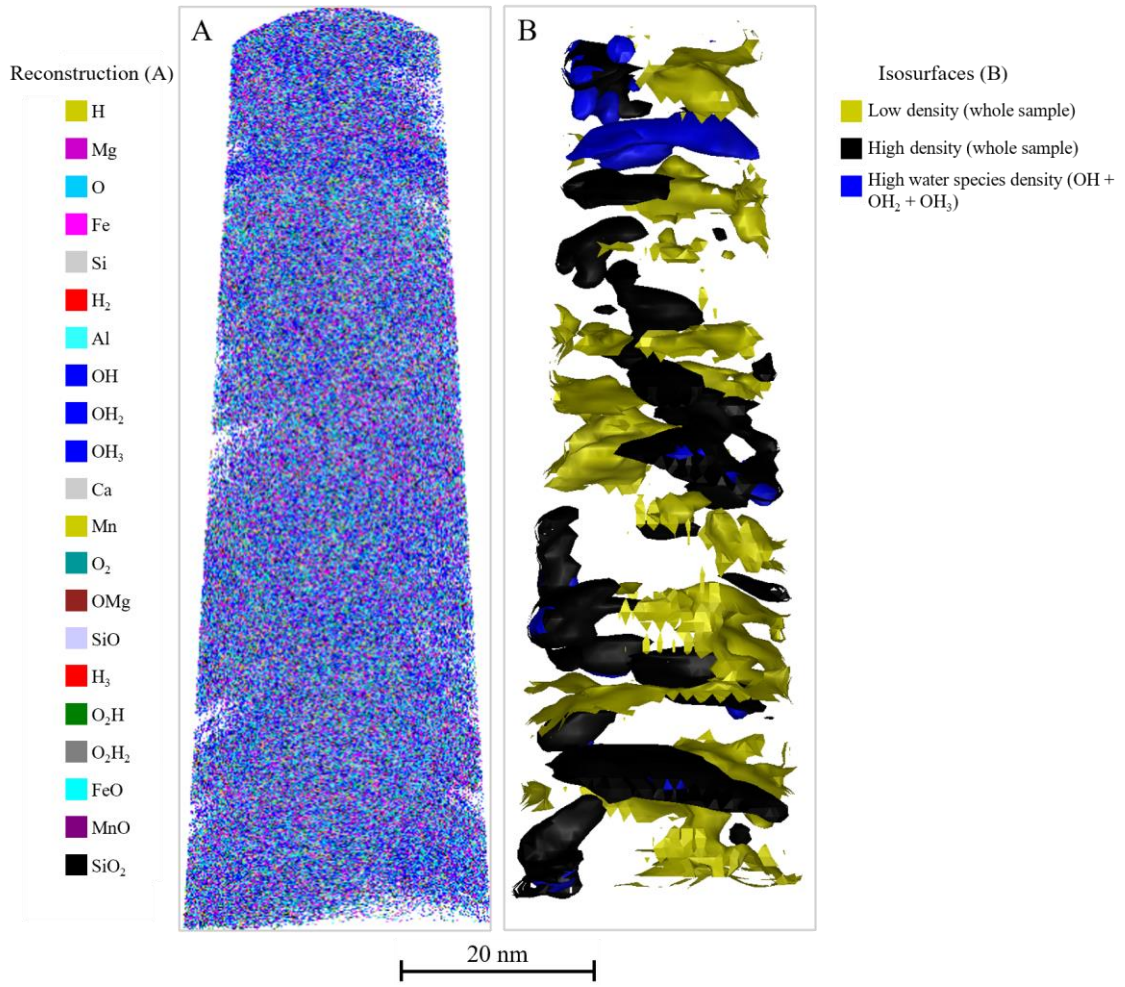

Figure 10 – A) represents a reconstruction of an NWA 817 iddingsite sample (Nakhlite1) whereas B) represents multiple density isosurfaces created from this reconstruction. B) highlights an area of high water species density (blue) that does not simply correlate with an area of high overall density in the sample (black) which is located near the top of the sample (sprawling left to right) – potentially presenting an area of true high water species density within the iddingsite sample.

These isosurfaces reveal areas of high and low density scattered throughout the whole reconstruction. Areas of high density typically correlate with areas of high water species density. An area of high water species density that does not overlap with an area of high density is observed near the top of the sample and is roughly 20 nm in diameter.

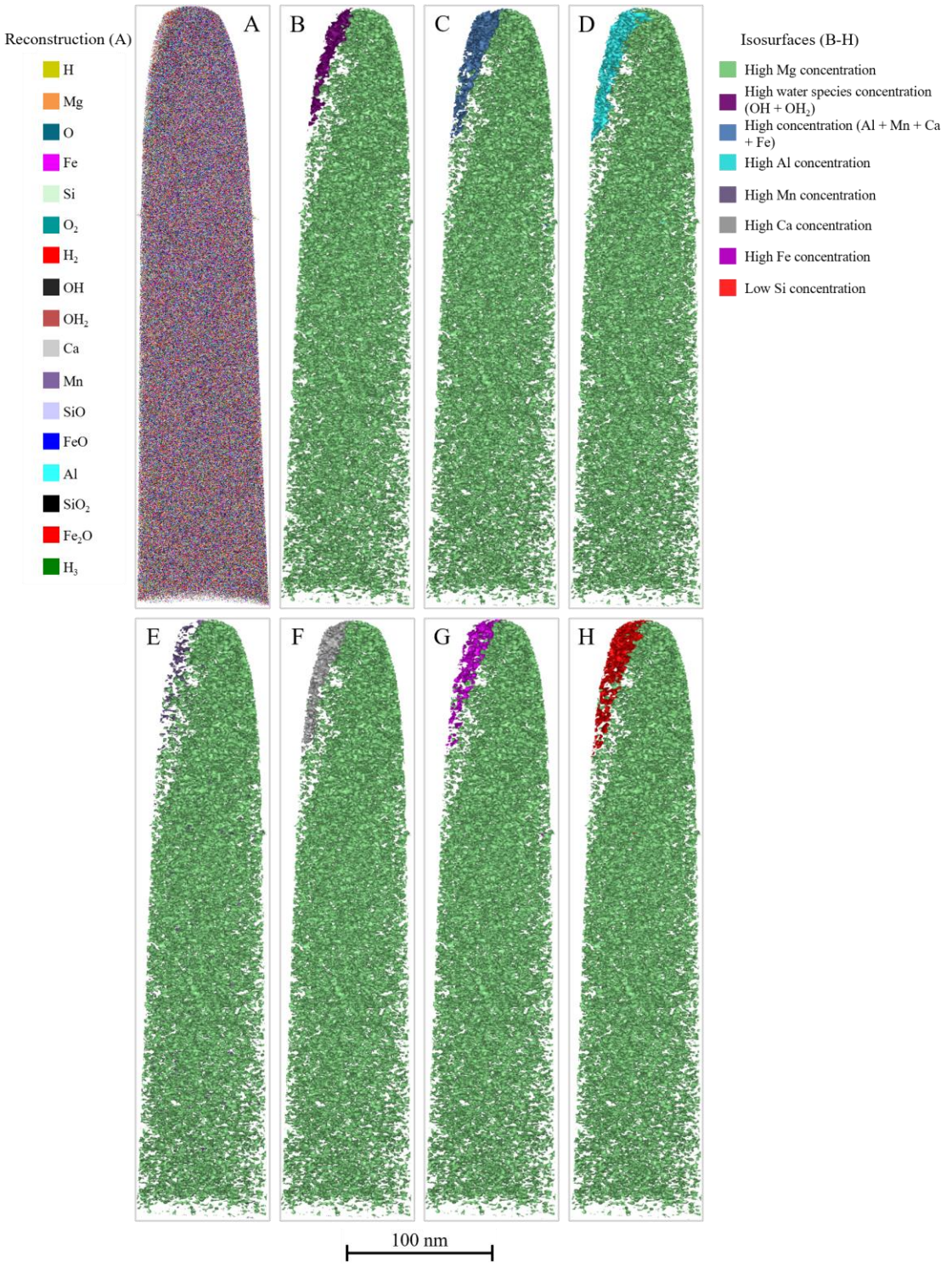

Figure 11 – A) is a reconstruction of an olivine-iddingsite interface in NWA 817 (Nakhlite2) whereas B) – H) are various concentration isosurfaces created from this reconstruction to highlight relative distribution of elements across the iddingsite interface. It should be noted that the small top left area (highlighted clearly by the produced isosurfaces) represents the iddingsite portion of the sample and the larger remaining portion represents the olivine.

Figure 11 highlights that iddingsite is higher in Mg, Al, Mn, Ca, and Fe concentration and lower in Si concentration compared to its host – olivine. Iddingsite also has a higher water species density – as expected of the aqueously altered material.

A 1-dimensional concentration profile was produced that runs straight through the olivine-iddingsite interface present in Nakhlite2 – done to investigate the concentration gradients of species which can provide insight into the mechanism of aqueous alteration (Daly *et al.*, 2019a). This is in Figure 12.

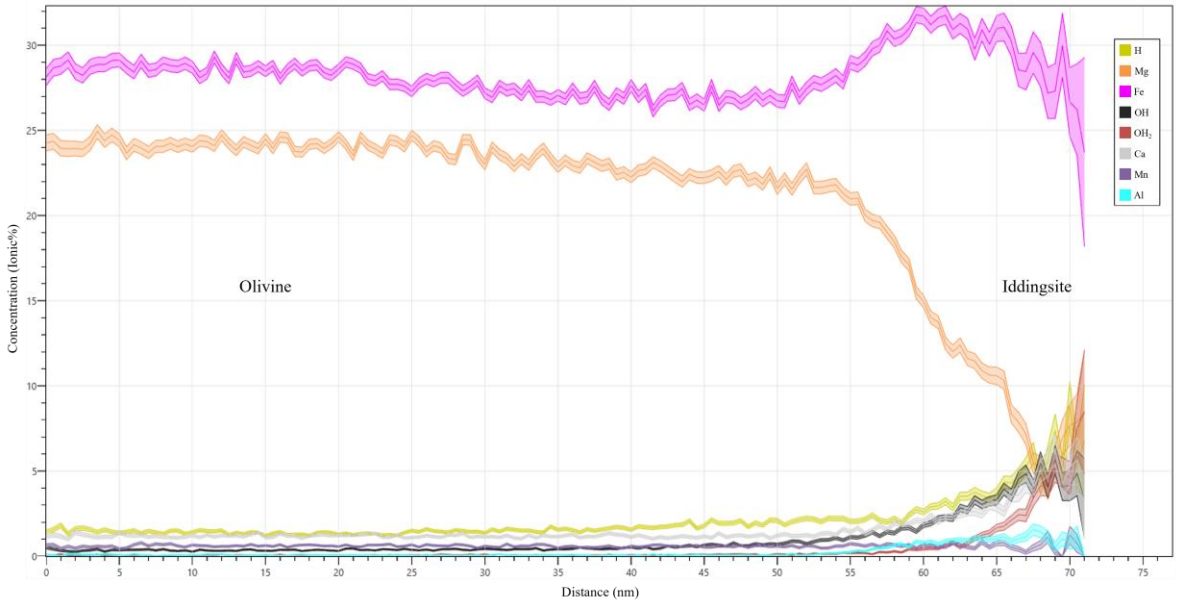

Figure 12 – A 1-dimensional concentration profile that runs through the olivine-iddingsite interface in Nakhlite2 (showing only a selection of species). Note that the coloured thickness of the trendlines represents the associated error with the concentration in ionic percentage. The interface can be recognised by the sharp change in concentration present in all of the shown species' concentrations beginning at around 55 – 60 nm (where the distance scale represents the distance along the 1-dimensional line created on the sample to produce this graph). It can be clearly seen that the water species concentrations (OH and OH_2 in this case) display a steep rise in concentration upon transitioning into the iddingsite portion of the reconstruction (right side of the graph) compared to the larger olivine portion of the sample (left side of the graph).

Appendix 2 contains a figure which details the exact area through which this 1-dimensional concentration profile was taken from in Nakhlite2. A steep change in concentration is observed in most species at around 55 – 60 nm – corresponding to the olivine-iddingsite interface. Passing into the iddingsite, Mg greatly decreases whereas Fe initially rises and then begins to fall. H, OH, OH_2, and Ca significantly increase past the interface and Mn and Al slightly increase. Species marginally increase or decrease in the preceding 15 – 20 nm before the interface (*e.g.* Mg slightly decreases from around 35 – 55 nm before sharply dropping).

Bulk composition analyses (background-corrected ionic counts) for both whole samples and multiple select regions of interest within each sample were recorded and then converted to wt%. This conversion was performed by transforming ion counts into mass via multiplication by the species' relative atomic mass, where OH, OH_2, and OH_3 were reserved for water (and all treated as H_2O when converting to mass). Once the total mass of the sample was known, the wt% of individual species (*e.g.* Mg wt%) could be calculated and

subsequently converted to the associated oxide wt% (*e.g.* MgO wt%) by a factor calculatable from the relative atomic mass of the main element and the associated oxide. Finally, these values were normalised such that the total wt% would be 100.00 wt%. These results are in Table 3.

Table 3 – Nakhlite1 and Nakhlite2 APT composition data (wt%) for both whole samples and regions of interest

		NWA 817 APT normalised composition (wt%)										
		$FeO + SiO_2$	MgO	Al_2O_3	P_2O_5	SO_2	CaO	TiO_2	MnO	NiO	Water	Total
Iddingsite	Literature average (olivine only)[a]	35.75 + 42.56	5.71	0.33	0.00	0.08	0.32	0.03	0.58	0.02	(14.69)*	85.31
Nakhlite1	Whole sample	63.44 + 19.07	9.01	0.13	-	-	0.20	-	0.81	-	7.35	100.00
	Whole sample (decomposed)[b]	60.91 + 19.78	9.32	0.15	-	-	0.80	-	1.42	-	7.63	100.00
	Representative cube[c]	63.57 + 20.02	9.63	0.15	-	-	0.32	-	0.90	-	5.41	100.00
	True water cylinder[c]	39.14 + 16.48	7.00	0.37	-	-	0.59	-	1.84	-	34.57	100.00
	Pseudo water cylinder[c]	62.72 + 18.04	10.14	0.00	-	-	0.36	-	0.72	-	8.02	100.00
Nakhlite2	Whole sample	55.72 + 19.69	21.80	0.06	-	-	1.55	-	0.96	-	0.22	100.00
	Whole sample (decomposed)[b]	52.44 + 22.40	22.17	0.07	-	-	1.64	-	1.05	-	0.23	100.00
	Olivine cylinder[d]	55.66 + 19.83	21.78	0.05	-	-	1.52	-	0.96	-	0.20	100.00
	Iddingsite cylinder[d]	69.50 + 14.46	9.36	1.15	-	-	3.09	-	0.86	-	1.57	100.00

"-" indicates where the oxide wt% could not be calculated because the main element was not assigned in the reconstruction

[a] NWA 817 literature average iddingsite oxide composition values produced in this project

[b] Created after running the whole sample data through the AP Suite 6 software's peak decomposition feature

[c, d] Exact location and explanation of these volumes of interest can be found in Appendix Figure 3 and Appendix Figure 4 (respectively) in Appendix 2

* Assumed to be the entire remainder of the total (*i.e.* 100 – 85.31 = 14.69 wt% water) for comparison purposes

Most notably, the "true water cylinder" has distinctly lower MgO and FeO content (plus higher water content) than the rest of the reconstruction. However the isobaric interference of the Fe^{2+} and Si^{+} peaks overlapping (at roughly 28 Da) means that proper distinction between the two counts was not possible (although, as demonstrated by J. Liu *et al.* (2022) for example, proper qualitative analysis is still possible by considering particular isotopes with unique atomic weights). In Nakhlite1 and Nakhlite2, the peak at 28 Da was assigned to Fe for both reconstructions (informed by surrounding isotope peak ratios) and thus resulted in higher Fe (and thus FeO) wt% values and lower Si (and thus SiO_2) wt% values than would be expected of these samples. As such, the FeO and SiO_2 wt% values are presented in the same column within Table 3 to highlight their apparent inseparability via this project's methods (where AP Suite 6's peak decomposition feature, as utilised by this project, also did not result in a marked difference to their values). Further, Nakhlite1 (which is composed of entirely iddingsite) shows significantly less water content than would be expected based on the literature average value of NWA 817 iddingsite (produced in this project). This may be the result of the known characteristic of APT to typically underestimate oxygen counts (Devaraj *et al.*, 2013; Karahka *et al.*, 2015) – thus resulting in lower OH, OH_2, and OH_3 counts and, consequently, reflecting a lower calculated water wt%.

3.2 Terrestrial Analogues

3.2.1 Initial Characterisation

As initiation into the analytical pipeline, all seven of the Rhynie chert and Yellowstone standard polished thin sections were inspected under optical microscopy in order to produce an initial characterisation of the sample and to acquire a preliminary assessment of the presence and surface-proximity of any preserved biogenic material. Figure 13 and Figure 14 are examples of the collage function utilised to image the entirety of Rhynie3 and Yellowstone1 (respectively) at 2.5x magnification and under varying light conditions.

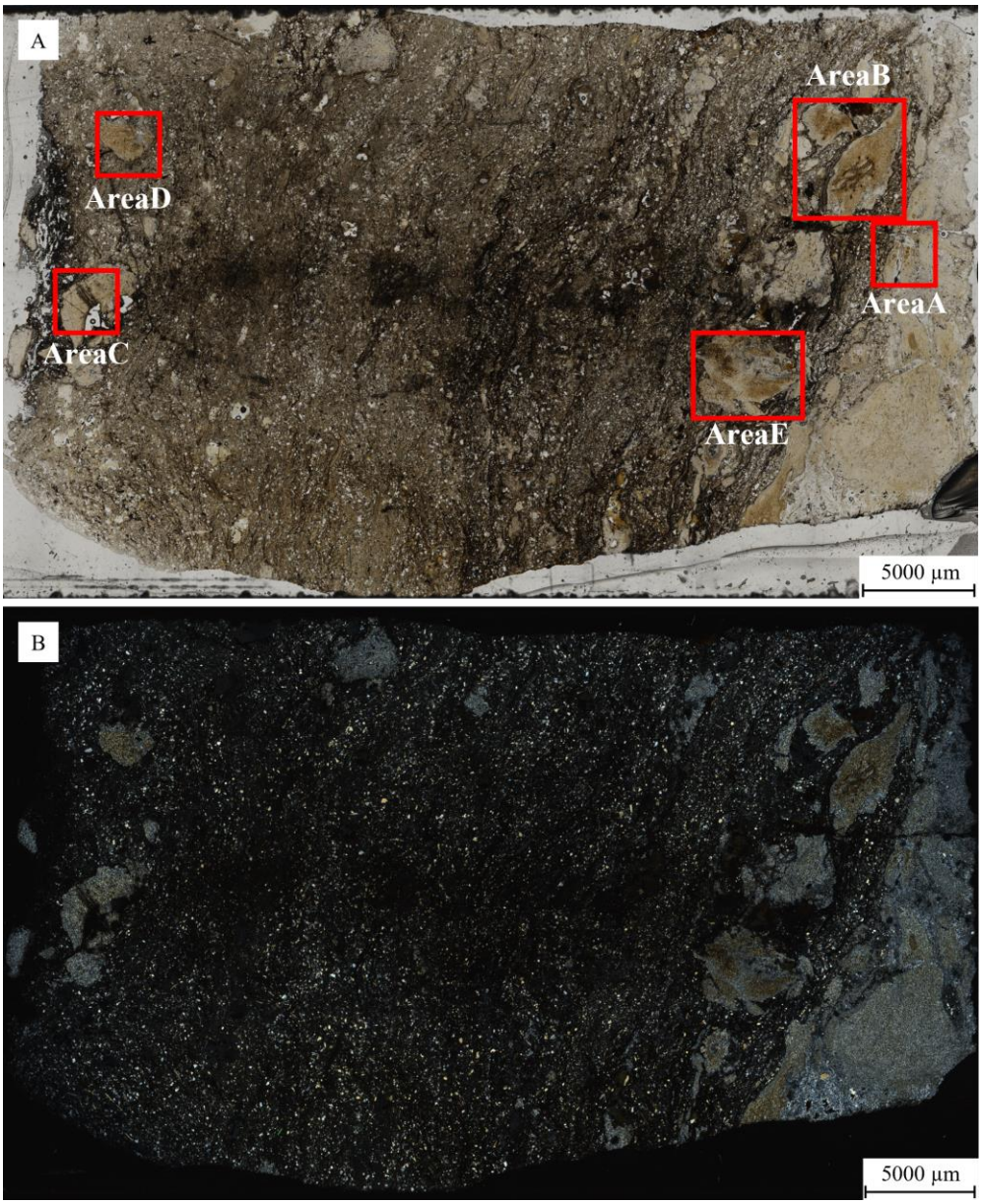

Figure 13 – Rhynie3 full-thin-section montages of 2.5x magnification images. A) is produced using plane polarised light whereas B) is produced under cross polarised light. Five areas of preserved fossils (arbitrarily labelled AreaA-E) are annotated by the red squares in A).

These montages show that the Rhynie chert samples consist of areas of chert dispersed throughout sandstone and that the chert is commonly host to fossilised organic material.

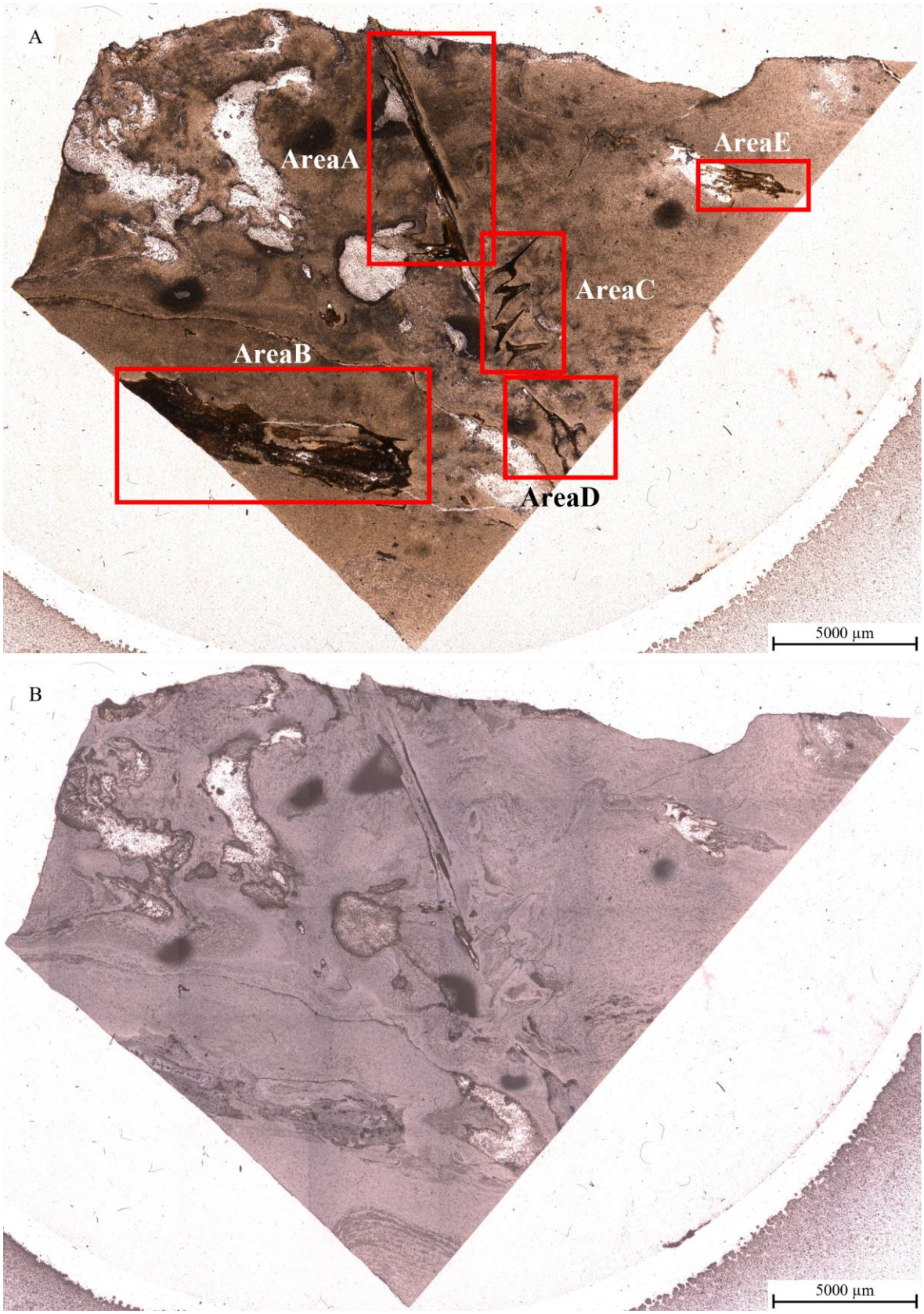

Figure 14 – Yellowstone1 full-thin-section montages of 2.5x magnification images. Collage A) is taken in transmitted plane polarised light whereas B) is taken in reflected plane polarised light (notably different to Figure 13 settings). Five areas of preserved fossils (arbitrarily labelled AreaA-E) are annotated by the red squares in A).

Figure 14 shows the distribution of fossils preserved within a siliceous material in the YellowstoneA sample.

Optical microscopy was further used to image the fossils at higher magnifications, create z-stack images, and inspect areas under reflected light. This was done to gain better insights into their depth into the thin section – because fossils must be sufficiently close to the surface to be accessed by later surface-sensitive techniques in the pipeline. Examples are in Figure 15 and Figure 16.

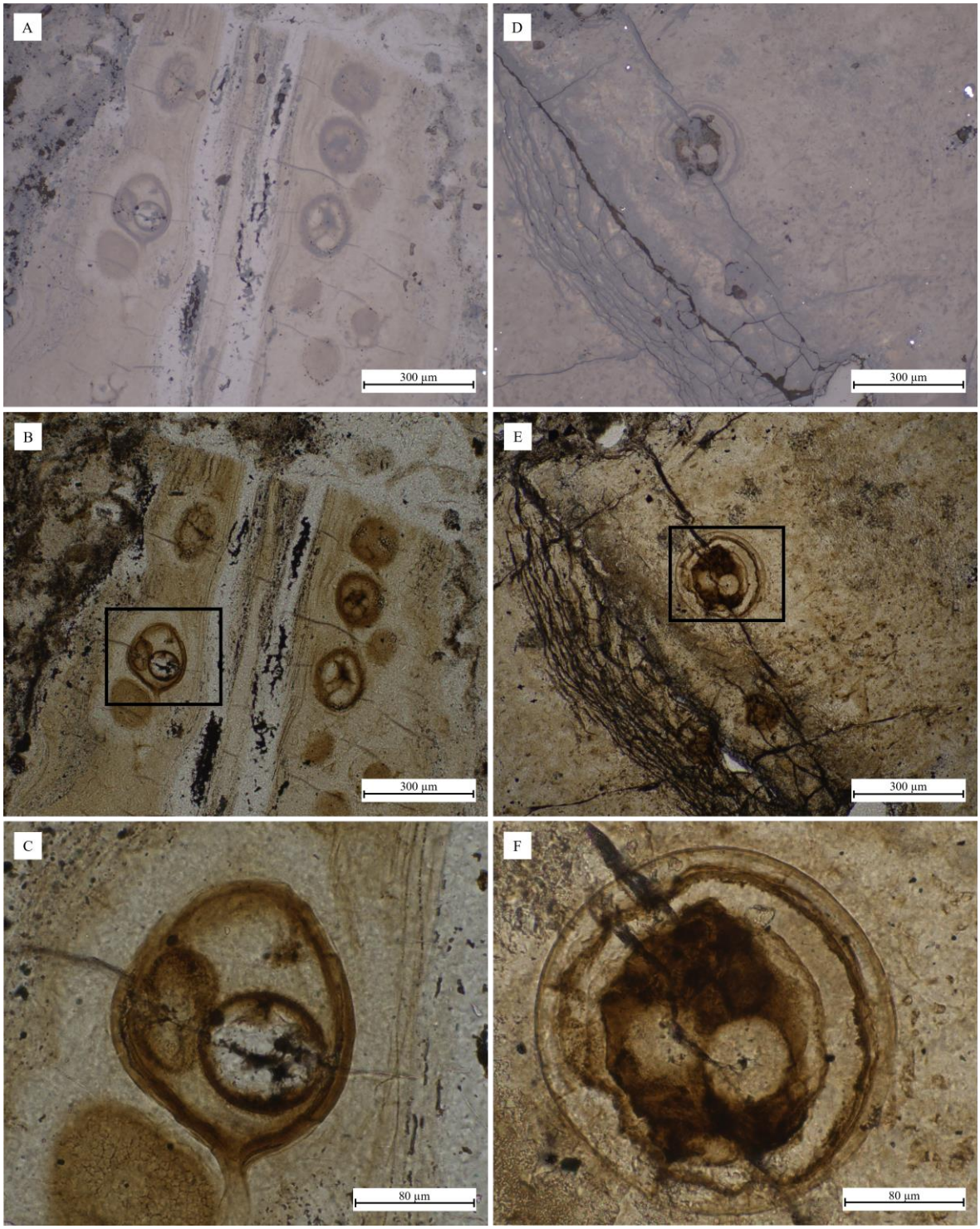

Figure 15 – Example of optical microscopy used to investigate Rhynie3 AreaA (images A) – C)), an area hosting fossils tentatively identified as fungal spores or chlamydospores upon comparison to work by Preston and Genge (2010), and Rhynie3 AreaC (images D) – F)) – presumed to be another fungal spore or a chytrid (Preston and Genge, 2010). Images A) and D) are reflected light images of both Rhynie3 AreaA and AreaC, respectively. Darker areas in these reflected light images were interpreted to represent topographical differences and thus these areas were selected for further investigation due to organic matter possibly being exposed to the surface. Images B) and E) are images of the respective fossils but using transmitted light instead. Black boxes in B) and E) signify where the following higher magnification images (images C) and F)) relate to. Images C) and F) represent z-stack images of Rhynie3 AreaA and AreaC, respectively.

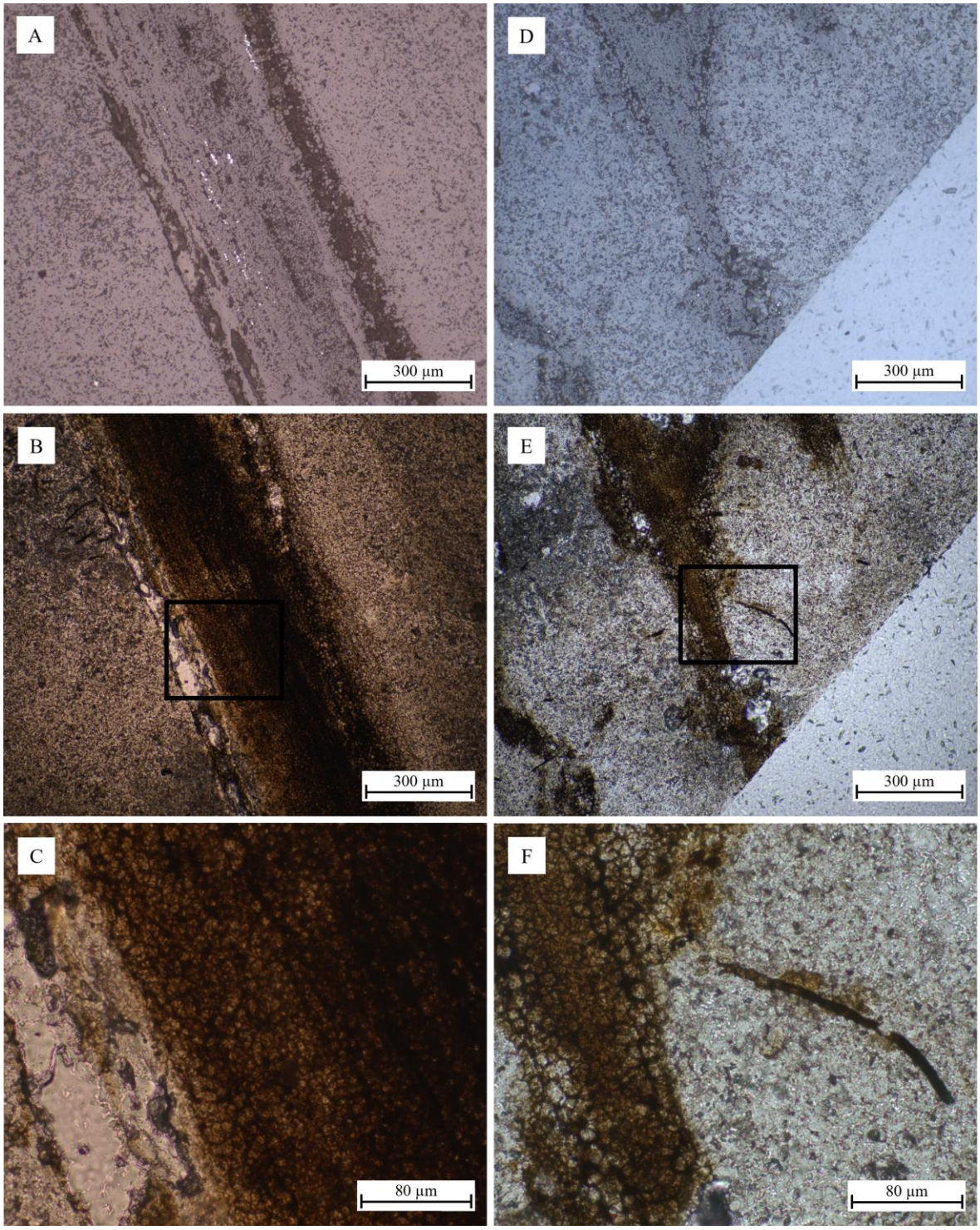

Figure 16 – Example of optical microscopy used to investigate Yellowstone1 AreaA (images A) – C)) and Yellowstone1 AreaD (images D) – F)) – both areas presumed to host fossilised plant cells of a *Magnolia spectabilis* leaf. Images A) and D) represent reflected light images of both Yellowstone1 AreaA and AreaD, respectively. Darker areas in these reflected light images were again interpreted to represent topographical differences, potentially hinting that the fossils are exposed to the surface. Images B) and E) are images of the respective fossils in transmitted light mode. Black boxes in B) and E) signify where the following higher magnification images (images C) and F)) are taken from. Images C) and F) represent images of Yellowstone 1 AreaA and AreaD, respectively.

Fossils determined to be likely sufficiently close to the surface (*e.g.* Rhynie3 AreaC in Figure 15 and Yellowstone1 AreaA in Figure 16) were then scrutinised by Raman spectroscopy with the goal of further investigating the identity of the preserved carbonaceous material

presumed present in the fossils. To start, a spectrum was acquired of an empty area in Rhynie3, Yellowstone1, and Yellowstone2 to acquire spectra of the epoxy resin used to make the thin sections. This was done to ensure that further analysis of carbonaceous material would not be merely reflecting peaks of the epoxy resin but instead the actual fossilised material. An example epoxy resin spectrum is in Figure 17.

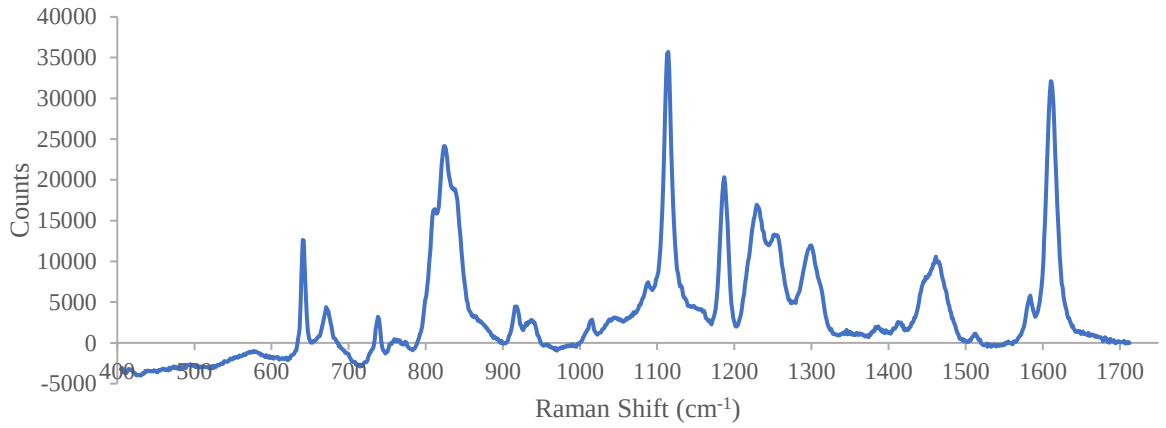

Figure 17 – Example of epoxy resin Raman spectra (after linear baseline removal from 1000 – 1750 cm^{-1} to ensure spectra are comparable) taken from an area on the outer edges of Rhynie3. Built-in library databases in the Renishaw WiRE software recognised these peaks as a match for epoxy resin – assisting in confirming that spectra were taken from the correct area.

Following this, a range of point spectra were acquired concerning the fossils in Rhynie3 (AreaA and AreaC) and in Yellowstone1 (AreaA). Figure 18 is an example of Rhynie3 and Yellowstone1 Raman acquisitions importantly encapsulating the quartz peak at around 465 cm^{-1} and the two key carbonaceous material peaks at around 1350 cm^{-1} and 1600 cm^{-1}.

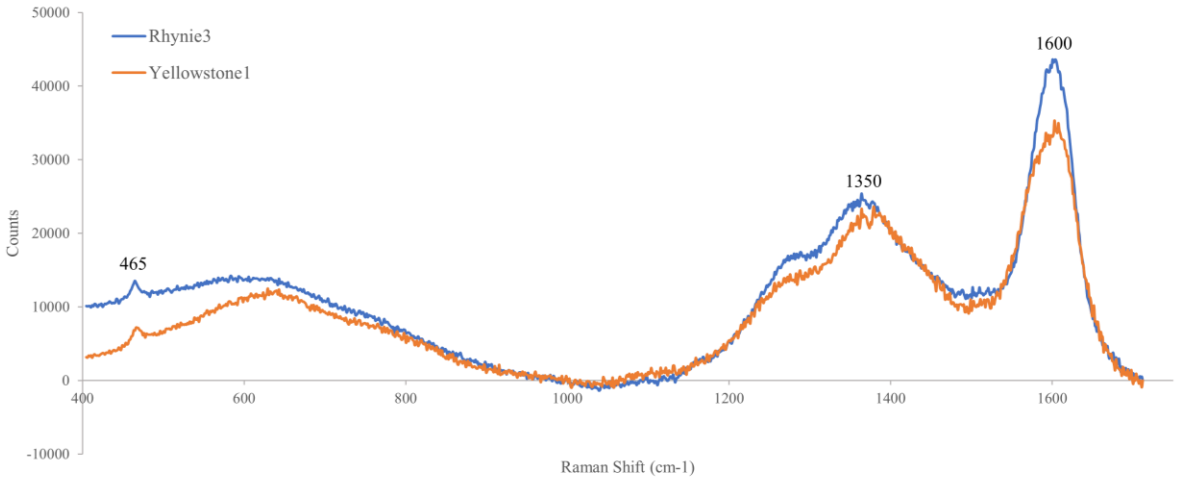

Figure 18 – Example Raman spectra taken from both Rhynie3 (blue) and Yellowstone1 (orange) illustrating that the chosen spectral range envelops both the quartz peak at around 465 cm^{-1} and the two key carbonaceous material peaks at around 1350 cm^{-1} and 1600 cm^{-1}. Note that the "peak" shape at around 650 cm^{-1} is merely an artefact of the linear baseline removal and is not reflecting an actual peak.

The spectra were treated following procedure suggested by Kouketsu *et al.* (2014) – *i.e.* baseline removed linearly over the range of 1000 – 1750 cm^{-1} and peak deconvolution (of the two key carbonaceous material peaks) performed following the flow chart presented in

Figure 3 of their paper. A labelled example of a baseline-removed and peak-deconvoluted Raman spectrum of Rhynie3 AreaC is in Figure 19.

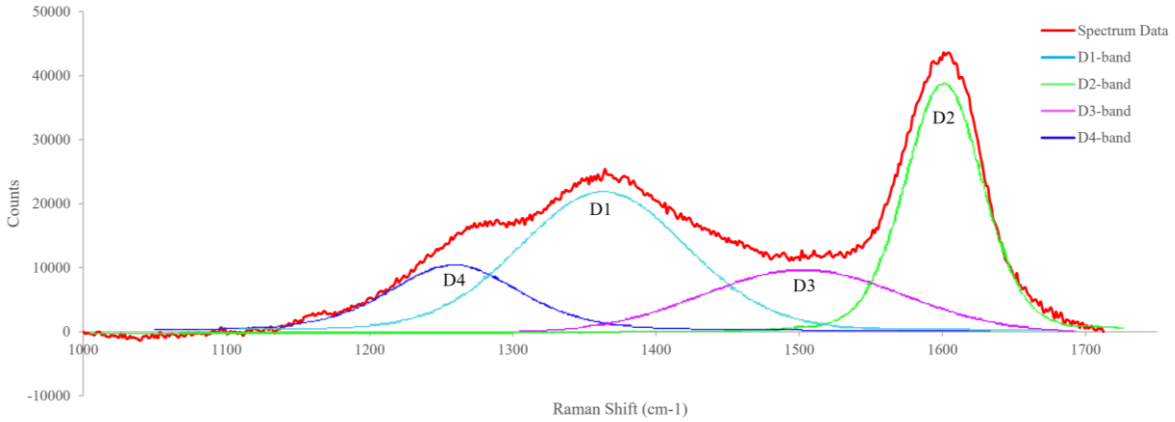

Figure 19 – A Raman spectrum from Rhynie3 AreaC over the 1000 – 1750 cm^{-1} range displaying the deconvolution of the key carbonaceous material peaks into the constituent D1-, D2-, D3-, and D4-bands (performed according to methodology outlined by Kouketsu *et al.* (2014)).

Parameters of these deconvoluted D-bands (*e.g.* area or full width at half maximum (henceforth FWHM)) can then be utilised as a geothermometer – *i.e.* can probe the peak metamorphic temperature experienced by the sample (Kouketsu *et al.*, 2014). Accordingly, Equation 2 and Equation 3 represent relations proposed by Kouketsu *et al.* (2014) for evaluating peak metamorphic temperature, valid in the range of roughly 150 – 400 °C, based on the D1-band FWHM and the D2-band FWHM, respectively.

$$T_1 = -2.15 \times D1_{FWHM} + 478$$ Equation 2

$$T_2 = -6.78 \times D2_{FWHM} + 535$$ Equation 3

Where T_1, T_2 = peak metamorphic temperature (°C)

$D1_{FWHM}$ = FWHM of the D1-band (cm^{-1})

$D2_{FWHM}$ = FWHM of the D2-band (cm^{-1})

For each spectrum acquired, both T_1 and T_2 were used to estimate the peak metamorphic temperature suggested by that spectrum. However, since the effective temperature range accurately covered by these equations is around 150 – 400 °C (Kouketsu *et al.*, 2014), any value calculated to be outside of this range was discarded. These filtered values were then used to estimate a preliminary range of possible peak metamorphic temperatures (*i.e.* the lowest (filtered) calculated temperature represents the initial lower bound and the highest (filtered) calculated temperature represents the initial upper bound of the range) that both the Rhynie chert and Yellowstone fossiliferous samples experienced. Although, the temperature

error accompanying $D1_{FWHM}$ is ±30 °C, and $D2_{FWHM}$ presents an error of ±50 °C (Kouketsu *et al.*, 2014). As such, the lower bound of the preliminary range was lowered by the appropriate error (*i.e.* by 30 °C or 50 °C depending on what equation was used) and, likewise, the upper bound of the range increased by either of these values – resulting in the final estimation of the peak metamorphic temperature range experienced by the Mars analogues. Acquired data suggests a peak metamorphic temperature range of roughly 100 – 210 °C (over eight spectra) for Rhynie3 and roughly 125 – 185 °C for YellowstoneA (over three spectra). It should be noted that the much younger Yellowstone samples will not have been metamorphosed as the old and buried Rhynie samples have – where the duration of heating and experienced pressures are largely different. As summarised by Qu *et al.* (2015), a peak metamorphic temperature of <360 °C (which both Rhynie chert and Yellowstone are calculated to exhibit in the present study) should imply that the ratio of intensity of the band at roughly 1350 cm^{-1} and the band at roughly 1600 cm^{-1} will decrease as the structural order of the examined carbonaceous material decreases. Thus, further analyses aimed to establish deeper insight into the structural order of the carbonaceous material by way of interrogating the value of intensity at 1350 cm^{-1} divided by intensity at 1600 cm^{-1} (henceforth referred to as the R-value). Figure 20 and Figure 21 are examples of spectra taken from Rhynie3 AreaC and Yellowstone1 AreaA (respectively) with their R-values annotated.

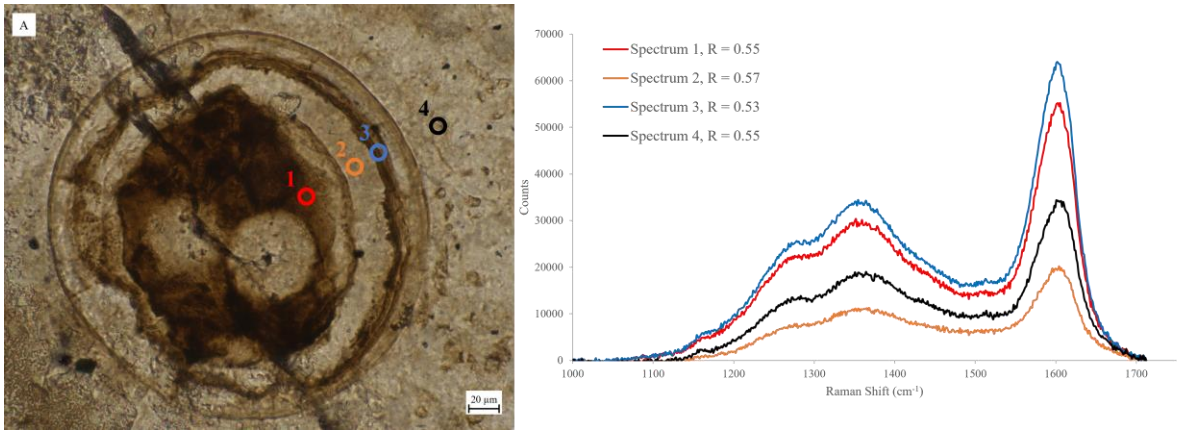

Figure 20 – The left image is an optical microscopy Rhynie3 AreaC z-stack image that is annotated (with both colour and number) to represent where the respective Raman spectrum was taken from. Note that the size of the annotating circles is arbitrary and does not represent the spot size. The right item is multiple baseline-removed Raman spectra (correlating to the annotations on image A)) overlayed onto the same graph with their colour, numbering, and calculated R-value annotated in the key. It should also be noted that the relative heights of the spectra are different due to varying acquisition conditions.

The lowest R-value is seen in the cell wall of the fungal fossil – suggesting a lower carbonaceous material structural order than both the intracellular material and the extracellular material.

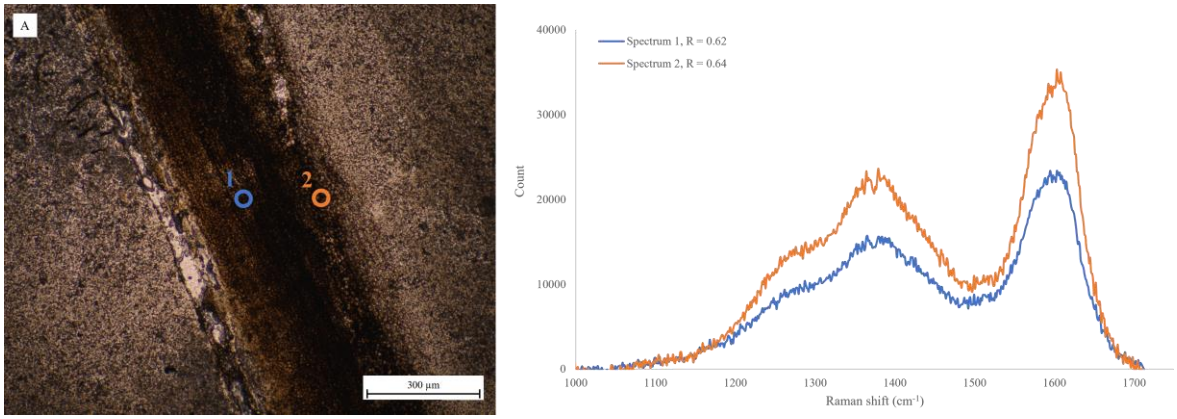

Figure 21 – Image A) is an optical image of Yelloswstone1 AreaA which is annotated with the approximate location of the respective Raman spectra (where the number and colour match that of the spectrum). Note that the size of the annotating circles is arbitrary and does not represent the spot size. The spectra on the right are from Yellowstone1 AreaA (after baseline removal) with their calculated R-values annotated in the key. It should also be noted that the relative heights of the spectra are different due to varying acquisition conditions.

The plant cells closer to the edge of the fossil have a higher R-value than those in the centre, although the difference is minor.

The WiRE software's mapping capability was utilised to produce multiple Raman spectral maps from Rhynie3 and Yellowstone2. These are in Figure 22 and Figure 23, respectively.

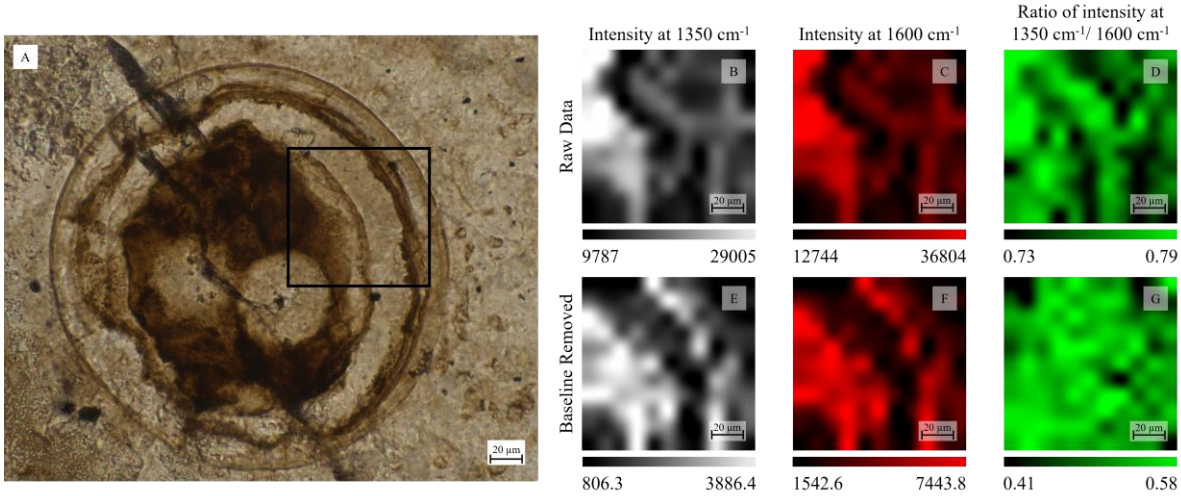

Figure 22 – Example of Raman maps produced concerning the key carbonaceous material peaks observed in Rhynie3 AreaC. Image A) represents a z-stack image of the Rhynie3 AreaC fossil with an overlaying black square annotating the area from which data was collected for Raman maps B) – G). Maps B) – D) are Raman maps produced from the raw collected data at the specified peak shift (*i.e.* 1350 or 1600 cm^{-1}, or the ratio between these intensities) – *i.e.* produced before baseline removal. Whereas maps E) – G) are produced after the linear baseline subtraction from 1000 – 1750 cm^{-1}.

Figure 22 map D) again shows that the R-value appears to be lowest in the cell wall of the fungal fossil. However, whilst the peak intensity maps E) and F) well resemble the fungal fossil, no explicit R-value trends are observed after baseline removal (map G)).

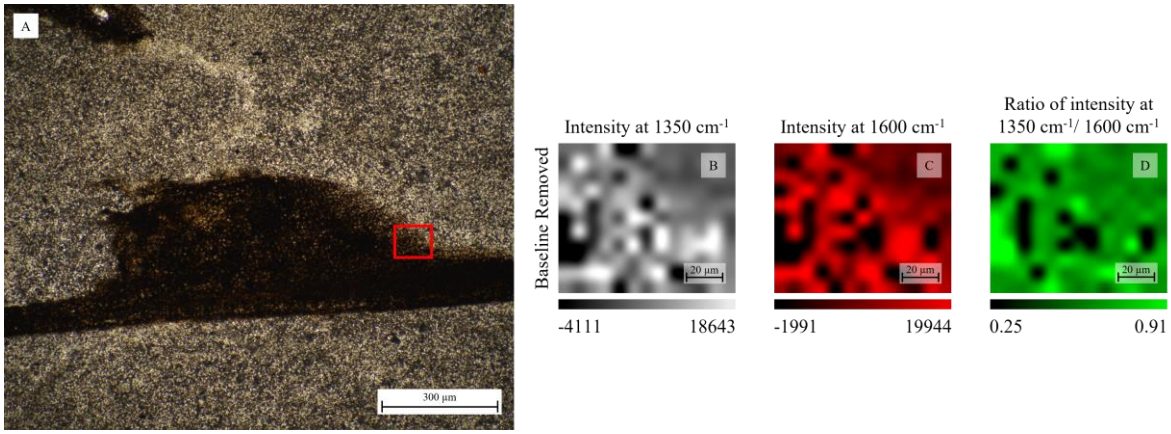

Figure 23 – Example of Raman maps produced of the key carbonaceous material peaks observed in Yellowstone2 AreaA. Image A) represents an image of Yellowstone2 AreaA fossilised plant cells with an overlaying red square annotating the area from which data was collected for Raman maps B) – D) – which are produced from the baseline-removed data at the specified peak shift (*i.e.* 1350 or 1600 cm^{-1}, or the ratio between these intensities).

No meaningful trends are observed in either of the intensity maps or the R-value map for this area of fossilised plant cells in Yellowstone2. This may be because of the scale of the map being too large to observe any differences on the cellular level.

Rhynie3 and Yellowstone1 were then further investigated via the in-depth analysis stage of the analytical pipeline.

3.2.2 In-depth Analysis

Both Rhynie3 and Yellowstone1 were inspected via SEM for high-resolution imaging and analysis of the elemental composition of chosen fossils. Figure 24 and Figure 25 are examples of such images.

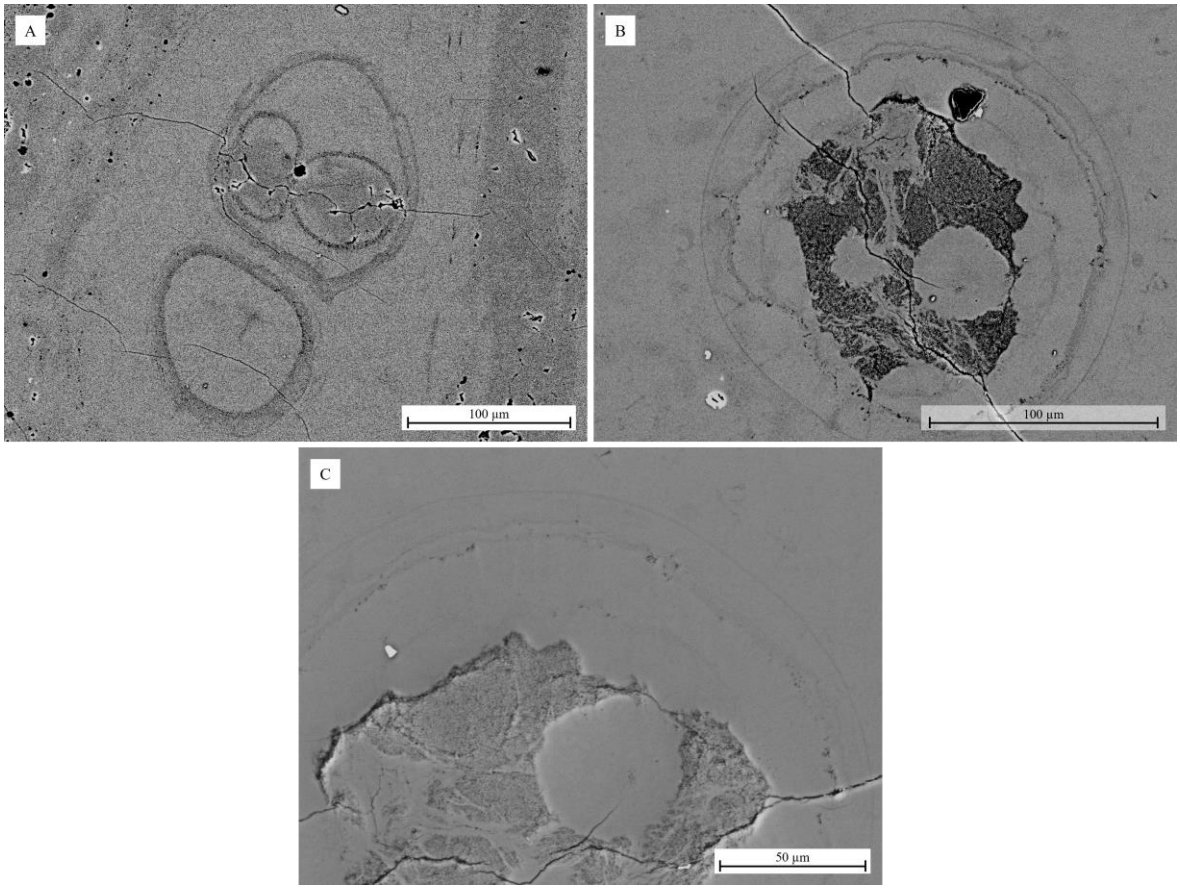

Figure 24 – BSE images of A) Rhynie3 AreaA and B) Rhynie3 AreaC. C) is an SE image of Rhynie3 AreaC (notably in a different orientation to B)). C) shows that the darker inner region of the fungal fossil is deeper in the thin section.

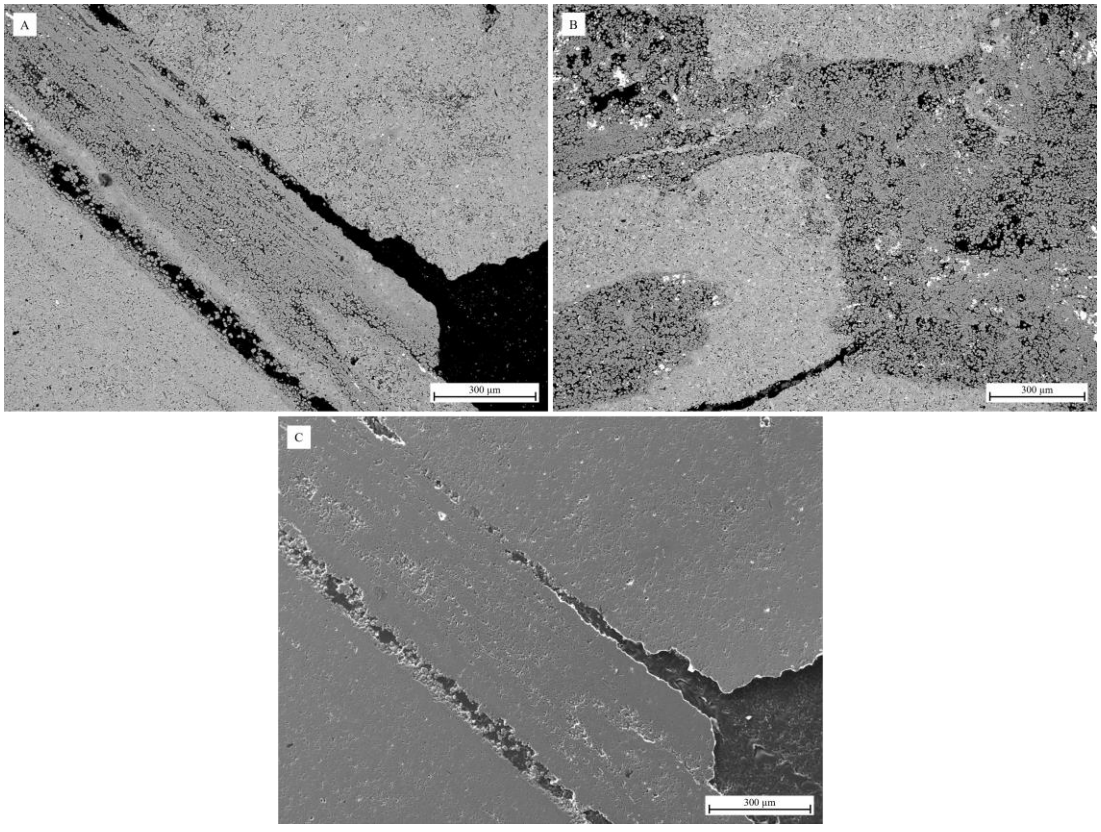

Figure 25 – BSE images of A) Yellowstone1 AreaA and B) Yellowstone1 AreaB. C) is an SE image Yellowstone1 AreaA and highlights the rough topography of the fossil and that it is mostly bordered by a hole.

Furthermore, images were captured at progressively increasing magnifications in order to assist in the later step of locating the fossils in the FIB (in preparation for investigation via TEM). Figure 26 and Figure 27 show examples of these images for Rhynie3 AreaC and Yellowstone1 AreaA, respectively.

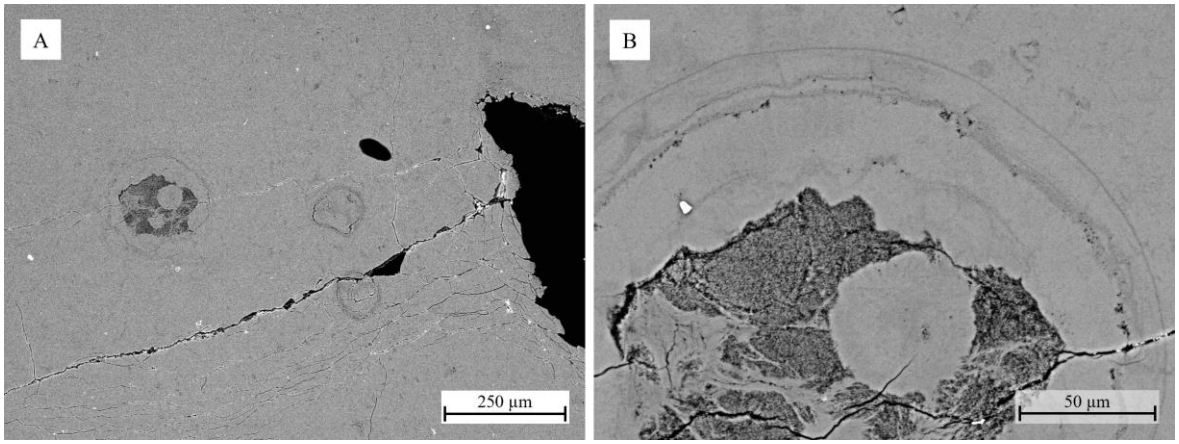

Figure 26 – A) and B) are a sample of the BSE images of Rhynie3 AreaC at varied magnifications that were used to assist in locating the fossil in subsequent FIB milling.

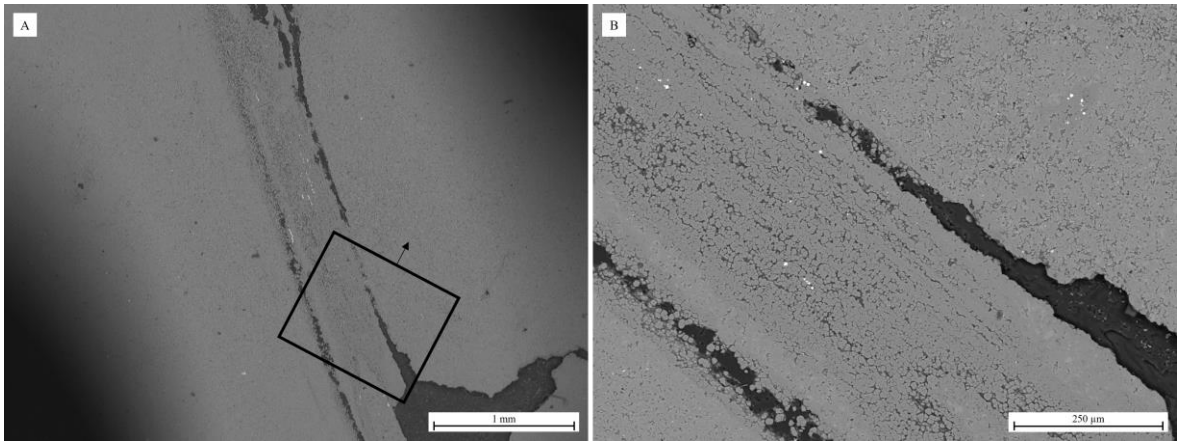

Figure 27 – A) and B) are exemplar images of Yellowstone1 AreaA at increasing magnifications that would later assist in locating AreaA in subsequent steps in the analytical process. A) is annotated with a black square to clarify the location and orientation of BSE image B) (where the annotated black arrow represents the upwards direction).

The elemental composition analysis functionality of SEM was utilised to map the distribution of elements in Rhynie3 AreaC and Yellowstone1 AreaA – mainly performed in order to investigate the distribution of carbon in the preserved fossils. This is in Figure 28 and Figure 29.

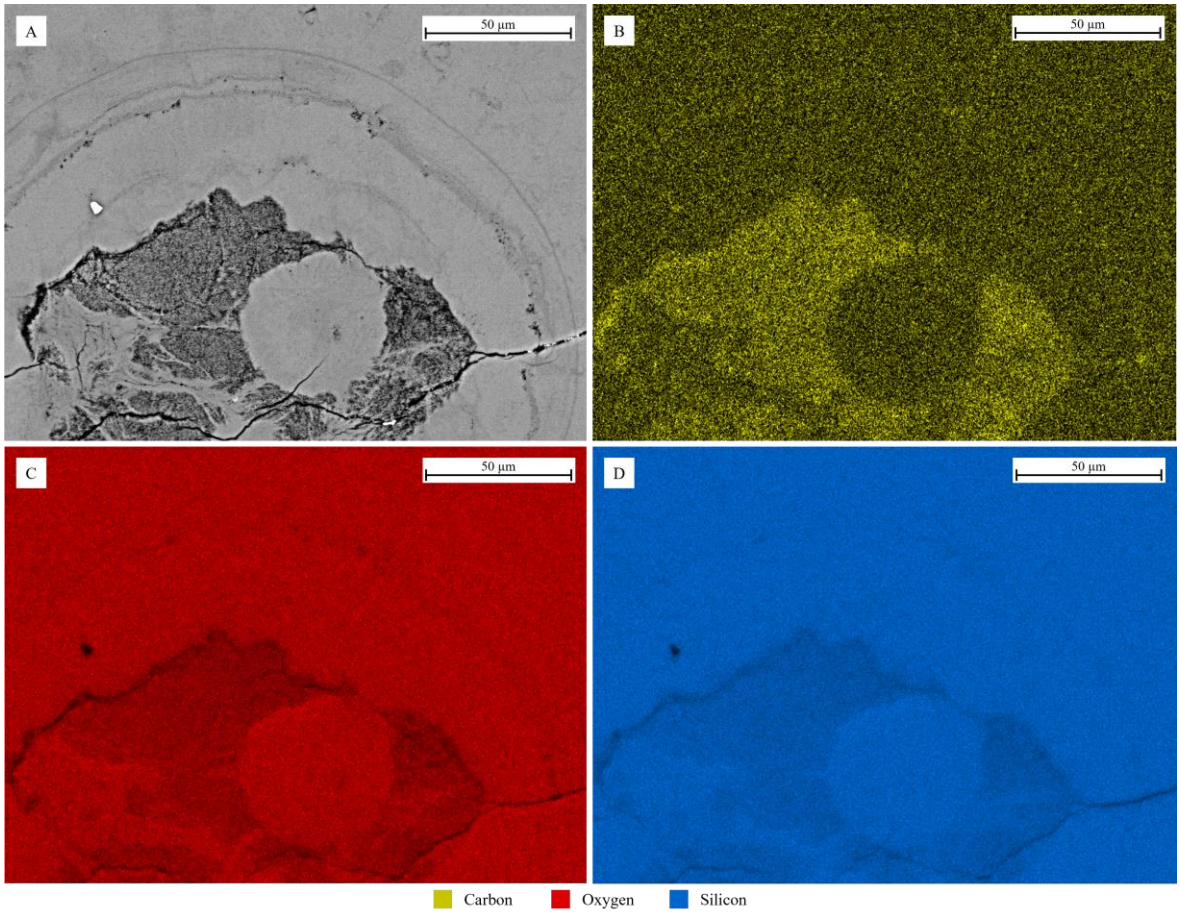

Figure 28 – EDX elemental maps of Rhynie3 AreaC. A) represents a BSE image of the area where the maps were taken from where the EDX maps are of B) carbon, C) oxygen, and D) silicon. It should be noted that the software's automatic coating compensation feature (which would attempt remove any signals from the carbon coating) was disabled for the acquisition of these maps in order to garner a more representative insight into the distribution of carbon in the fungal fossil.

Increased carbon concentration is observed in the deeper area inside the preserved fungal cell and a slight increase tracing the cell wall. High abundances of oxygen and silicon are observed – which is expected of a chert (mainly SiO_2). The oxygen and silicon counts are slightly decreased in the deeper area of the fossil corresponding to increased carbon concentration.

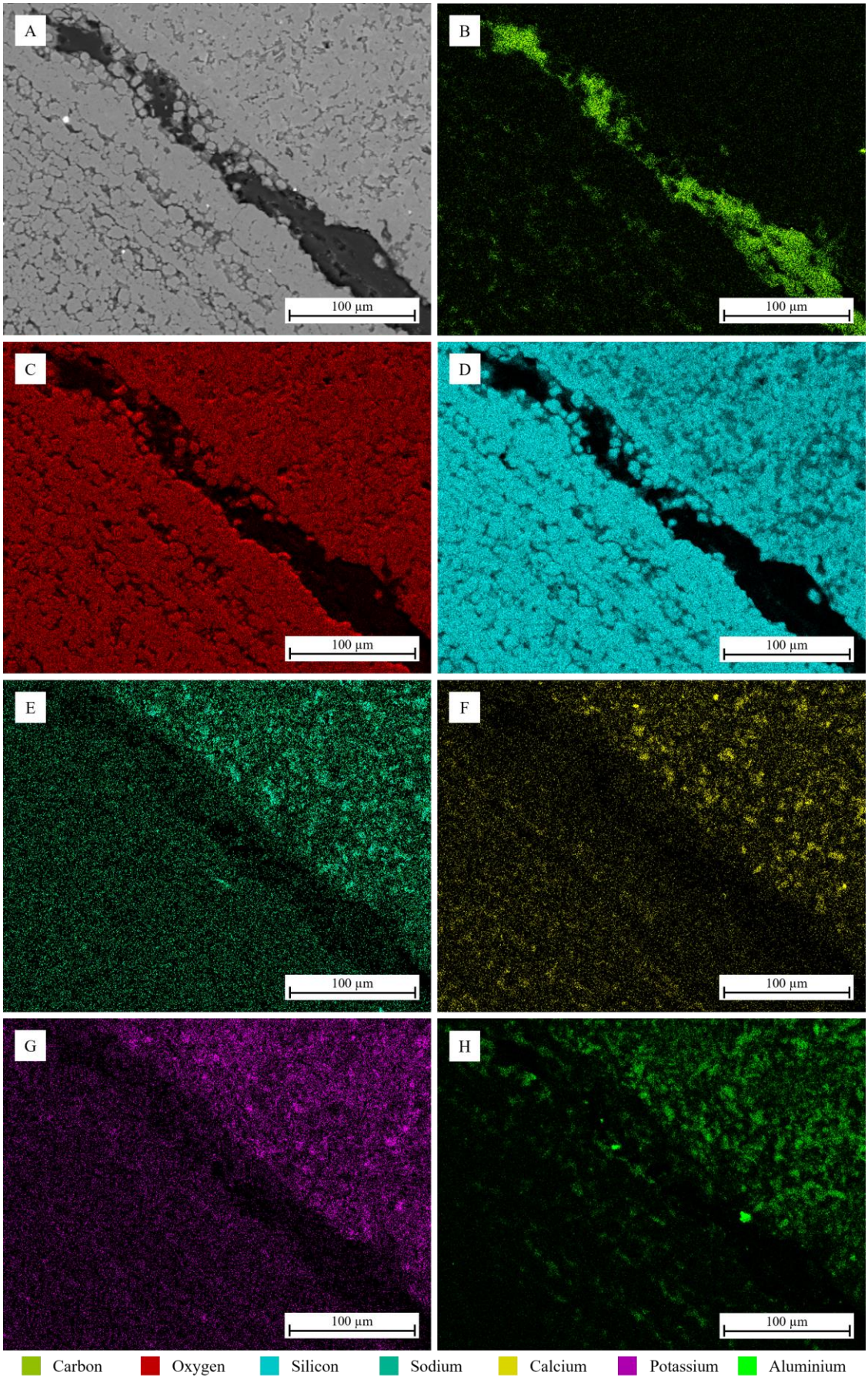

Figure 29 – EDX elemental maps of Yellowstone1 AreaA. A) represents a BSE image of the area where the maps were taken from where the EDX maps are of B) carbon, C) oxygen, D) silicon, E) sodium, F) calcium, G) potassium, and H) aluminium. It should be noted that the software's automatic coating compensation feature (which would attempt remove any signals from the carbon coating) was also disabled for the acquisition of these maps in order to garner a more representative insight into the distribution of carbon in the fossilised plant material.

Figure 29 maps show a large increase in carbon concentration corresponding to the hole that borders the fossilised plant cells – likely reflecting the epoxy resin of the thin section. Small areas of increased carbon concentration are also observed corresponding to topographical variation within the fossilised material. Unlike the Rhynie chert sample, the encapsulating material is enriched in Na, Ca, K, and Al. These are possible in impurities (Boggs, 2011) (*e.g.* clay minerals), and abundant O and Si suggests that this sample is an impure chert.

Rhynie3 AreaC was chosen for investigation via TEM due to the fossil's good preservation and surface proximity and, in preparation for this, two electron-transparent slices were milled and lifted out of the cell wall of the preserved fossil. The approximate location of the two cuts is displayed in Figure 30.

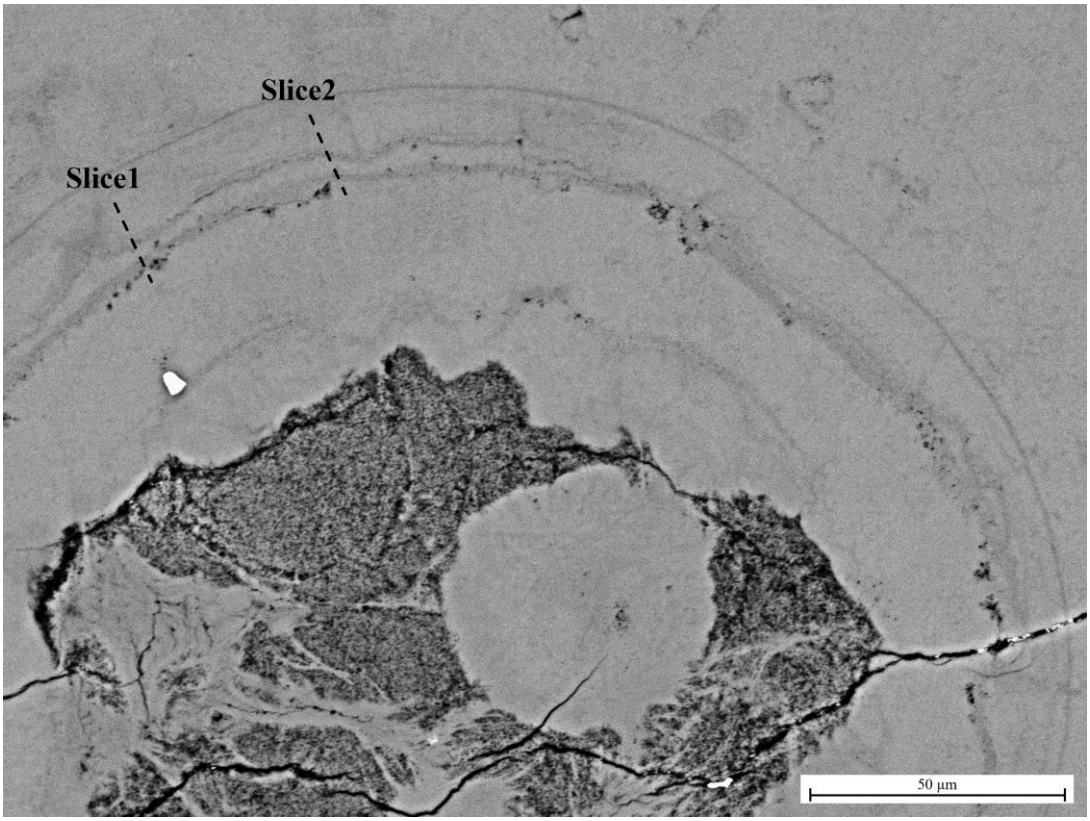

Figure 30 – BSE image of Rhynie3 AreaC with dashed black lines annotating roughly where the two electron transparent slices (Rhynie3 Slice1 and Rhynie3 Slice2) were taken from in the cell wall of the fungal species.

The FEI TEM was utilised to produced electron diffraction patterns of the crystalline material within both Rhynie3 Slice1 and Rhynie3 Slice2 in order to confirm its identity. Importantly, an electron diffraction pattern was captured of the Pt layer (deposited onto the top of each slice during the milling process) at the same magnification as the electron patterns produced for both Rhynie3 Slice1 and Rhynie3 Slice2 – allowing proper calibration of the calculated d-spacings. Figure 31 presents the miller index assignments of the diffraction patterns for both Rhynie3 Slice1 and Rhynie3 Slice2.

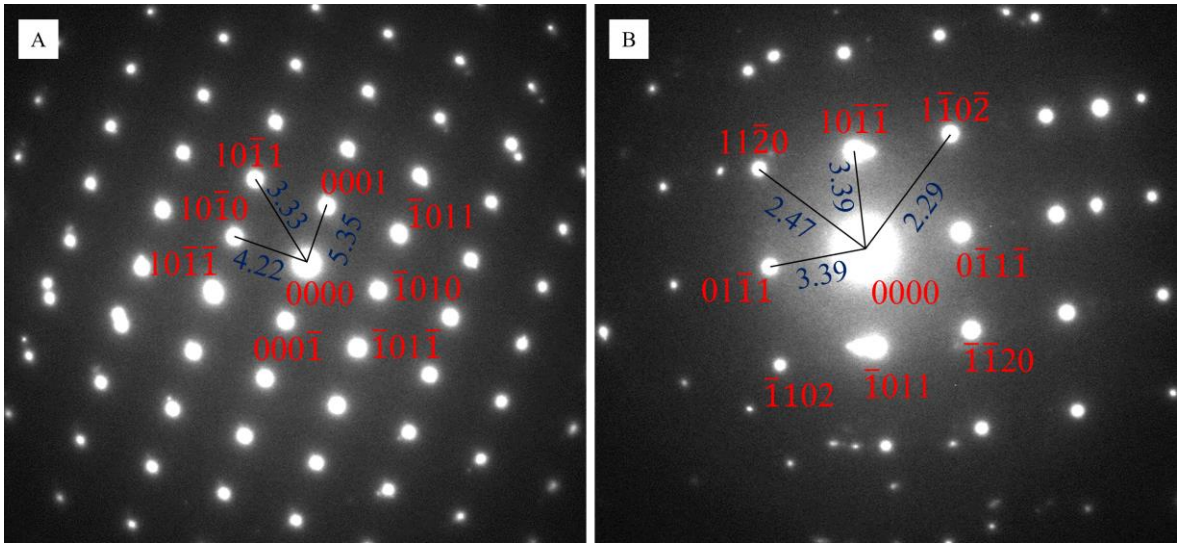

Figure 31 – TEM-produced electron diffraction patterns for A) Rhynie3 Slice1 and B) Rhynie3 Slice2. Annotating both images are miller index assignments (in red) in the standard form of hkil, and calculated d-spacings (Å) in dark blue. Miller indices, d-spacings, and inter-planar angles are all consistent (within reasonable distance and angle measurement error) with a hexagonal structure and cell parameters of a = 4.913 Å and c = 5.405 Å – as expected of quartz (Antao *et al.*, 2008).

These results (*i.e.* miller indices, angles, and d-spacings being consistent with quartz cell parameters (Antao *et al.*, 2008)) confirm the identity of the crystalline material abundant within each slice to be quartz – as expected of the Rhynie chert.

The FEI TEM was used to collect bright-field images of both slices. Bright-field images observed at different stage tilts revealed a non-crystalline inclusion in amongst the crystalline (chert) matrix of Rhynie3 Slice1 which was postulated to potentially be organic carbon preserved within the cell wall of the fossilised fungal species. Figure 32 presents bright-field images of the entirety of Rhynie3 Slice1 and of the non-crystalline inclusion.

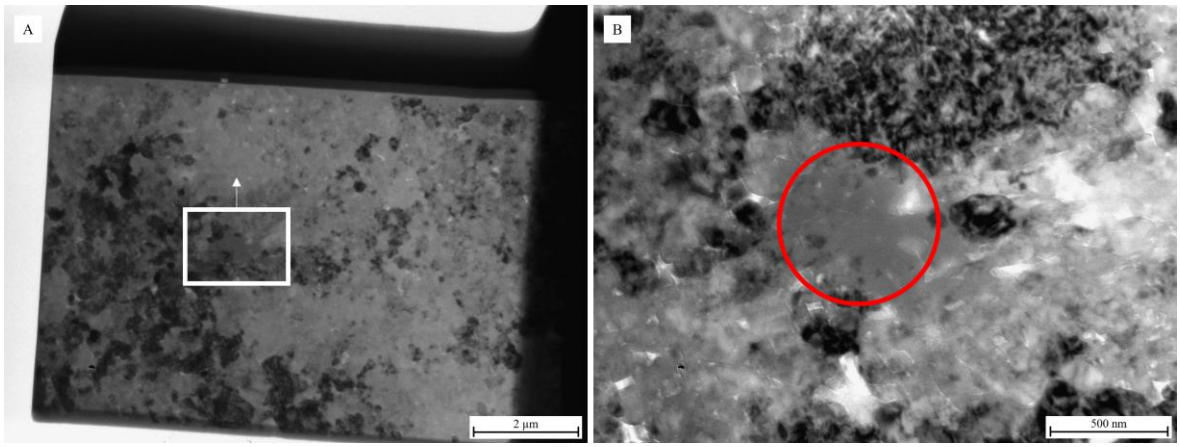

Figure 32 – A) is a bright-field TEM image of the entirety of Rhynie3 Slice1 annotated with a white square outlining the location of bright-field image B) (where the white arrow represents the upwards direction). The mostly-monochromatic grey inclusion within the annotated red circle in B) was postulated to be non-crystalline (and thus potentially organic) based on its unchanging appearance at varying orientations (unlike the encapsulating quartz crystals which changed greatly in contrast upon differing stage tilts).

The identification of this potentially-organic inclusion within Rhynie3 Slice1 (Figure 32 B)) prompted further analysis by STEM and, thus, two further electron-transparent slices were lifted from Rhynie3 AreaC and two electron-transparent slices were lifted from Yellowstone1 AreaA. Figure 33 and Figure 34 detail the approximate location of these incisions.

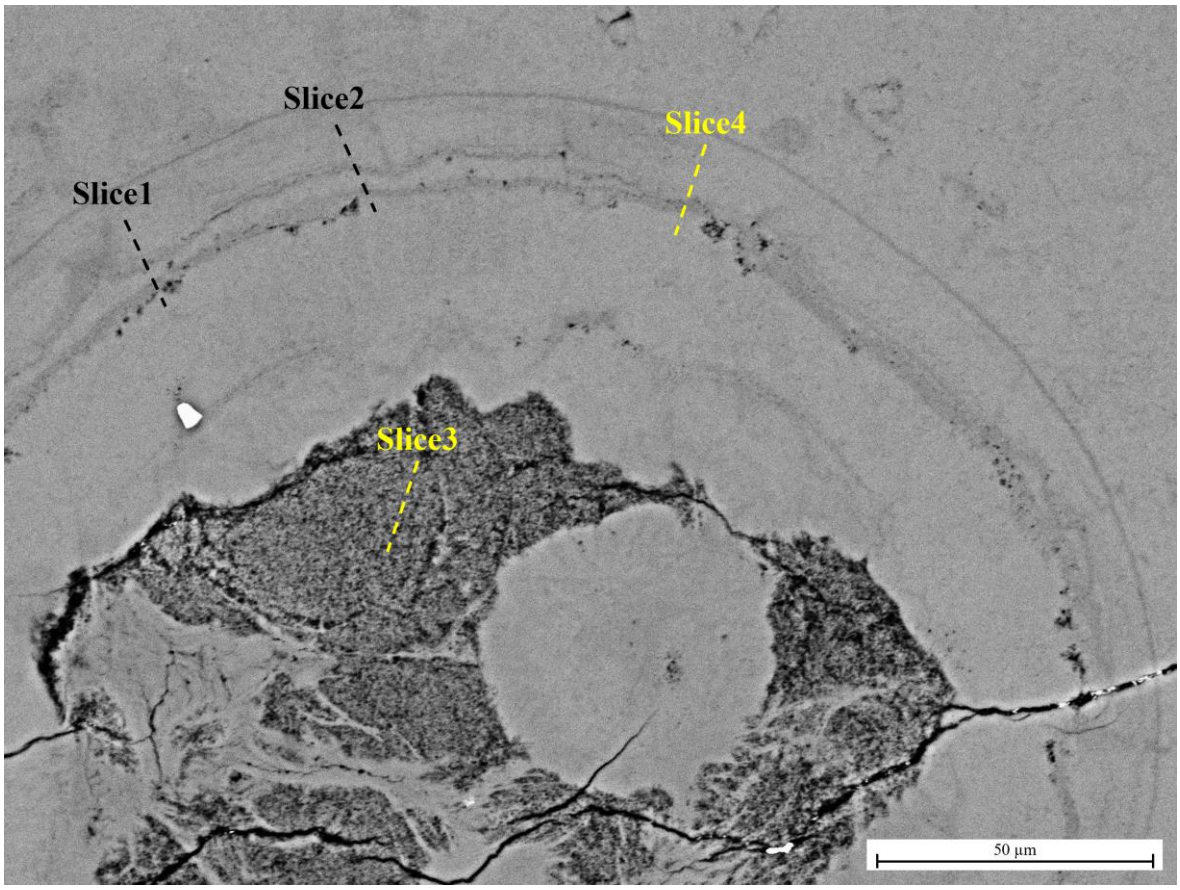

Figure 33 – BSE image of Rhynie3 AreaC with dashed black lines detailing the location of the previous two FIB mills (Rhynie3 Slice1 and Rhynie3 Slice2) and dashed yellow lines annotating where the further two electron-transparent slices (Rhynie3 Slice3 and Rhynie3 Slice4) were taken from.

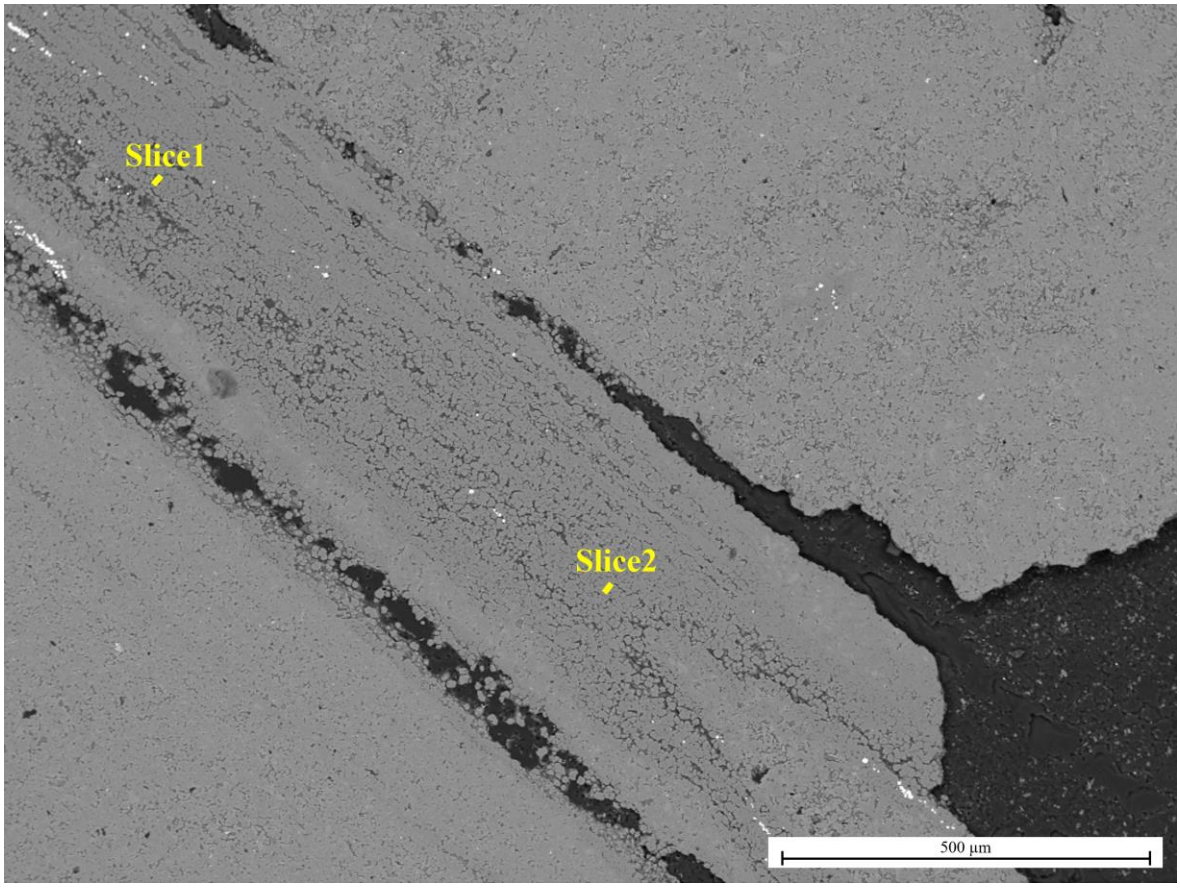

Figure 34 – BSE image of Yellowstone1 AreaA with yellow lines annotating the location of the milled electron-transparent slices (Yellowstone1 Slice1 and Yellowstone1 Slice2). It should be noted that the yellow lines have been increased in size for clarity and do not represent the exact size of the milled slices.

Contrast in high-angle annular dark-field (HAADF) images, owing to the high angle of detection, is heavily influenced by atomic number – *i.e.* a strong Z-contrast (Lee, 2010). Thus, HAADF should allow the distinction between the important carbon and the slightly-heavier encapsulating oxygen and silicon. The JEOL TEM was used to acquire HAADF images of each new slice. These are in Figure 35 and Figure 36.

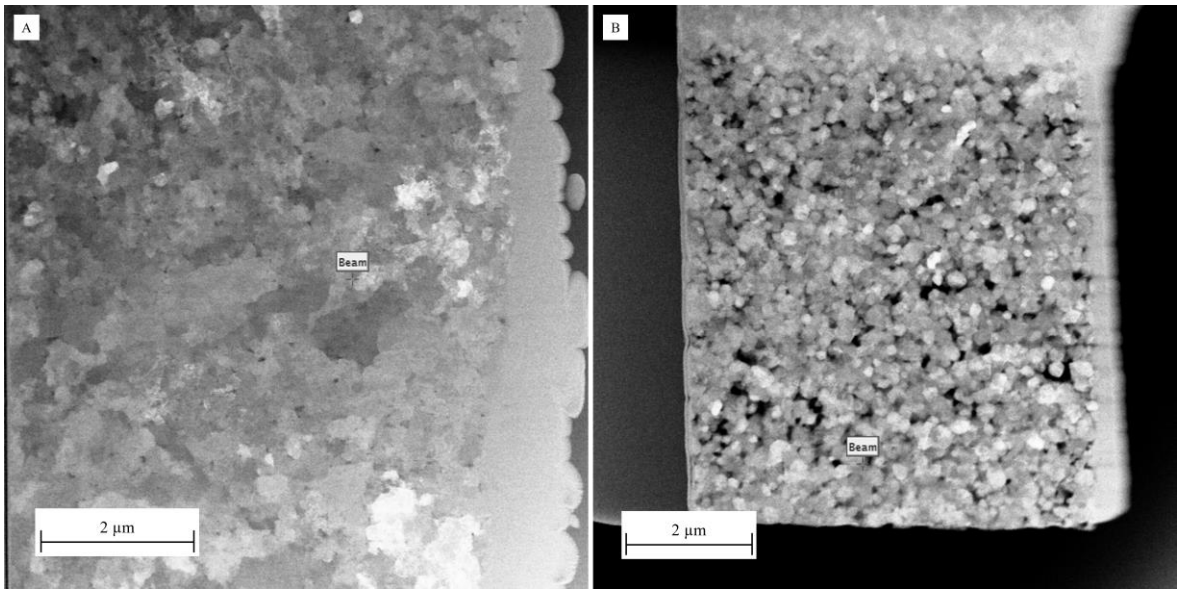

Figure 35 – HAADF images of the entirety of A) Rhynie3 Slice3 and B) Rhynie3 Slice4. The "Beam" textbox and crosshairs in each image are merely digital artefacts annotated atop the images.

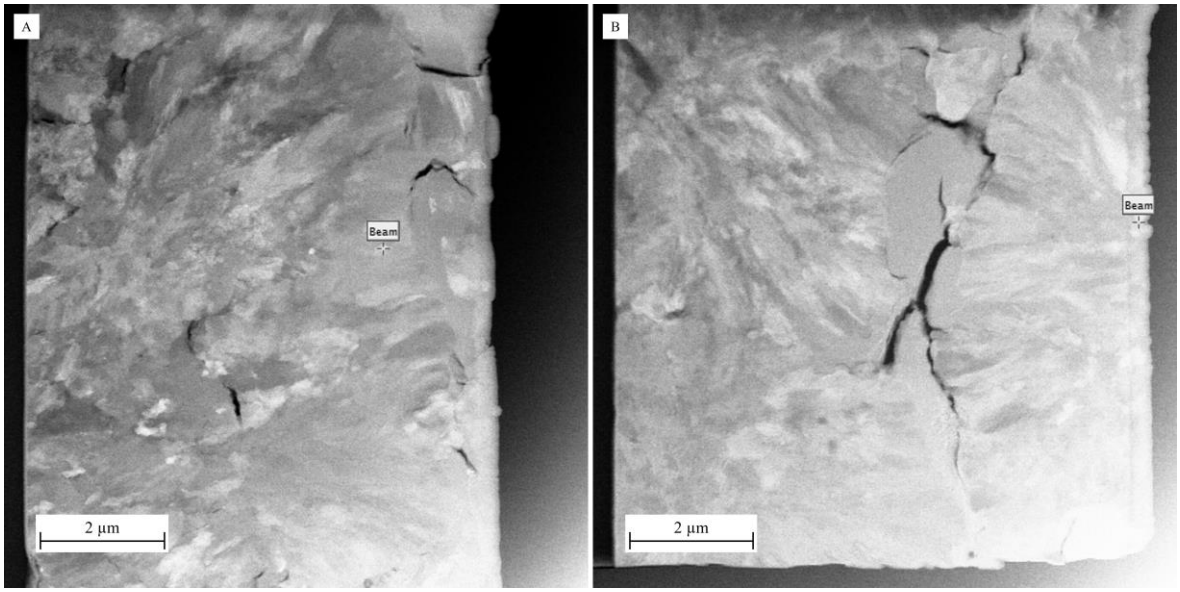

Figure 36 – HAADF images of the entirety of A) Yellowstone1 Slice1 and B) Yellowstone1 Slice2. The "Beam" textbox and crosshairs in each image are merely digital artefacts annotated atop the images.

Dark areas in these HAADF images are interpreted to be the lower atomic number carbon, whereas the lighter areas are interpreted as chert (silicon and oxygen). For the Rhynie chert slices (especially Rhynie3 Slice4), these darker areas are spread throughout the whole sample. The darker areas in the Yellowstone slices are concentrated into larger streaks.

STEM and EELS were then used to directly investigate the composition of the darker areas present within the HAADF images of both the Rhynie slices (Figure 35) and the Yellowstone slices (Figure 36). STEM HAADF images in combination with STEM EELS maps of Rhynie3 Slice4 and Yellowstone1 Slice1 are in Figure 37 and Figure 38, respectively.

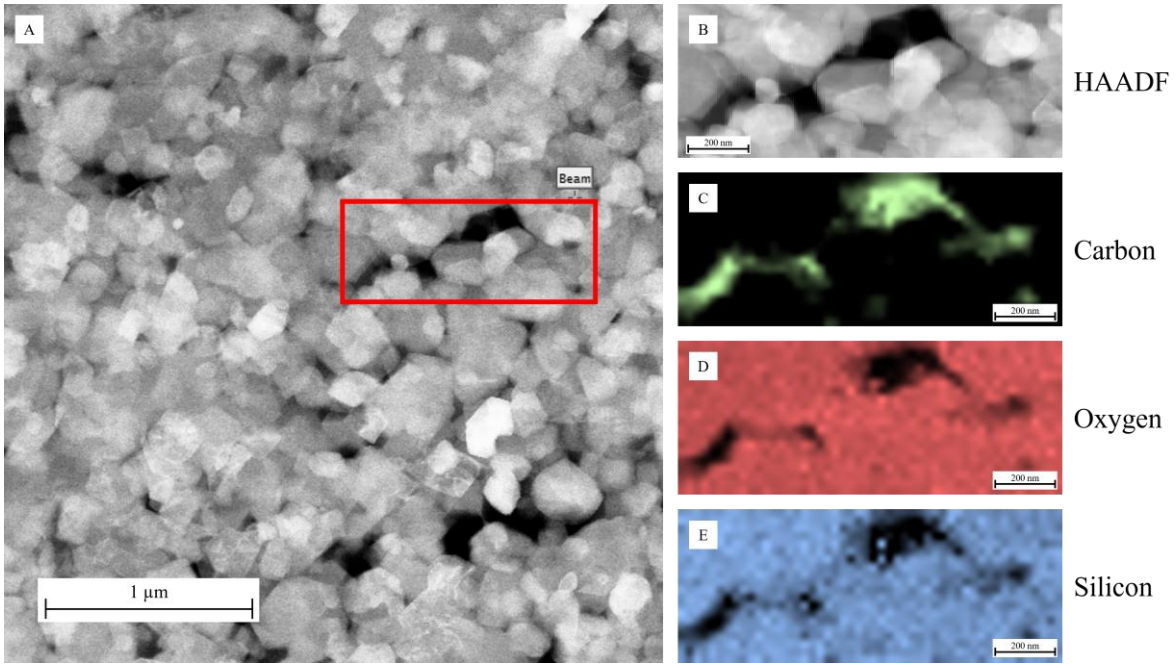

Figure 37 – A) is a standard TEM HAADF image of Rhynie3 Slice4 which is annotated with a red square that denotes the precise location of B) a STEM HAADF image of a darker region in A). The "Beam" textbox and crosshairs in A) are merely digital artefacts annotated atop the image. C) – E) are artificially-coloured STEM EELS maps detailing the distribution of carbon, oxygen, and silicon within the region of interest imaged in B) – confirming that the dark areas within B) correspond to areas of carbon.

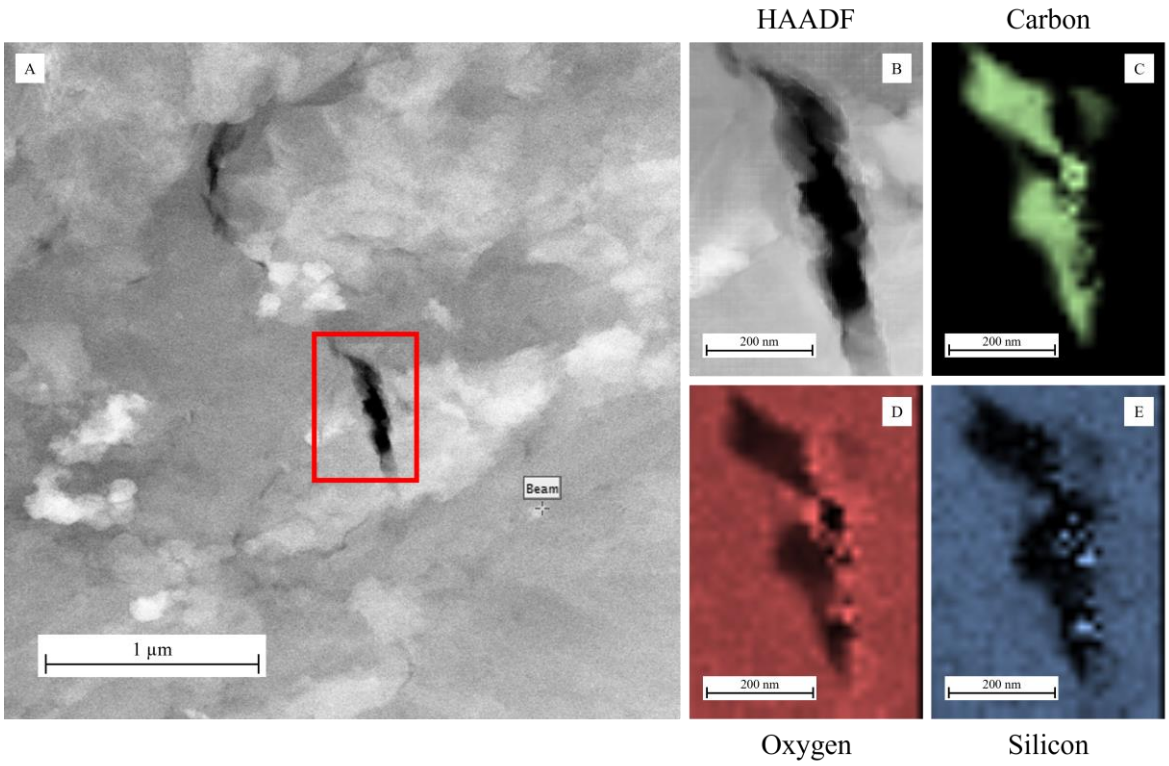

Figure 38 – A) is a standard TEM HAADF image of Yellowstone1 Slice1 which is annotated with a red square that indicates the precise location of B) a STEM HAADF image of a darker region in A). The "Beam" textbox and crosshairs in A) are merely digital artefacts annotated atop the image. C) – E) are artificially-coloured STEM EELS maps detailing the distribution of carbon, oxygen, and silicon within the region of interest imaged in B) – confirming that the dark areas within B) broadly correspond to areas of carbon.

From Figure 37 and Figure 38 (along with further data not displayed), STEM EELS data confirmed that the dark regions in HAADF images across the four electron-transparent slices generally corresponded to areas of carbon within both the Rhynie chert and Yellowstone samples. Carbon in the Rhynie chert slices is dispersed throughout in areas roughly 100 – 300 nm in size, meanwhile carbon in the Yellowstone slices is concentrated into larger streaks roughly 0.5 – 2.5 μm long. Decreased oxygen and silicon content coinciding with these areas of increased carbon suggests that carbon is inhabiting the space between quartz crystals (SiO_2) – detailing the nm-scale incorporation of carbon within these siliceously preserved fossils.

This concludes the Results chapter, where the results of this project's investigation into Martian meteorites and Mars terrestrial analogues were reported. The following chapter, Discussion, will interpret these results in the context of the project goals and their relation to the broader literature.

4. Discussion

4.1 Martian Meteorites

4.1.1 Insight into Iddingsite

Iddingsite is a complex mixture of materials including hydrous silicates, iron oxides, and iron oxyhydroxides (Lee *et al.*, 2018). The literature compilation produced in this project provides a detailed overview of the oxide composition of iddingsite within a sizable selection of nakhlites. Iddingsite's average composition ranges from roughly 3 – 11 wt% MgO, 0.3 – 3.8 wt% Al_2O_3, 38 – 43 wt% SiO_2, 0 – 2.1 wt% SO_2, 0.1 – 2.7 wt% CaO, 0.5 – 1.6 wt% MnO, and 28 – 39 wt% FeO across the 11 nakhlites – representing a wide range of compositions.

The compilation graphs in Figure 8, plotting bulk rock composition versus olivine-hosted iddingsite composition, also reveal interesting trends with potential implications for the nakhlite alteration at 633 Ma. A strong positive correlation is observed between the bulk rock MgO content and iddingsite MgO content. This relationship was also observed in Lee *et al.* (2018), considering only four of the 11 nakhlites included in the present project. It is simultaneously observed (in the present project) that other oxides (*e.g.* Al_2O_3 and CaO) do not follow this directly proportional relationship. SiO_2 content exhibits little variation (relatively) which is expected since a major component of iddingsite are silicates. Iddingsite FeO is observed to decrease as bulk rock FeO increases. This may be explained by the incorporation of iron in iddingsite being a more complicated process – largely determined by the oxidation of the altering fluid (Gay and LeMaitre, 1961). Bulk rock Al_2O_3 content displays a clear bimodal distribution in Figure 8. It is postulated that this difference in Al_2O_3 content arises from the differing amount of mesostasis present in the meteorite. Figure 39 is a graph of the bulk rock Al_2O_3 content (wt%) produced in this project versus the bulk rock mesostasis content in volume percentage (vol%) from Corrigan *et al*. (2015).

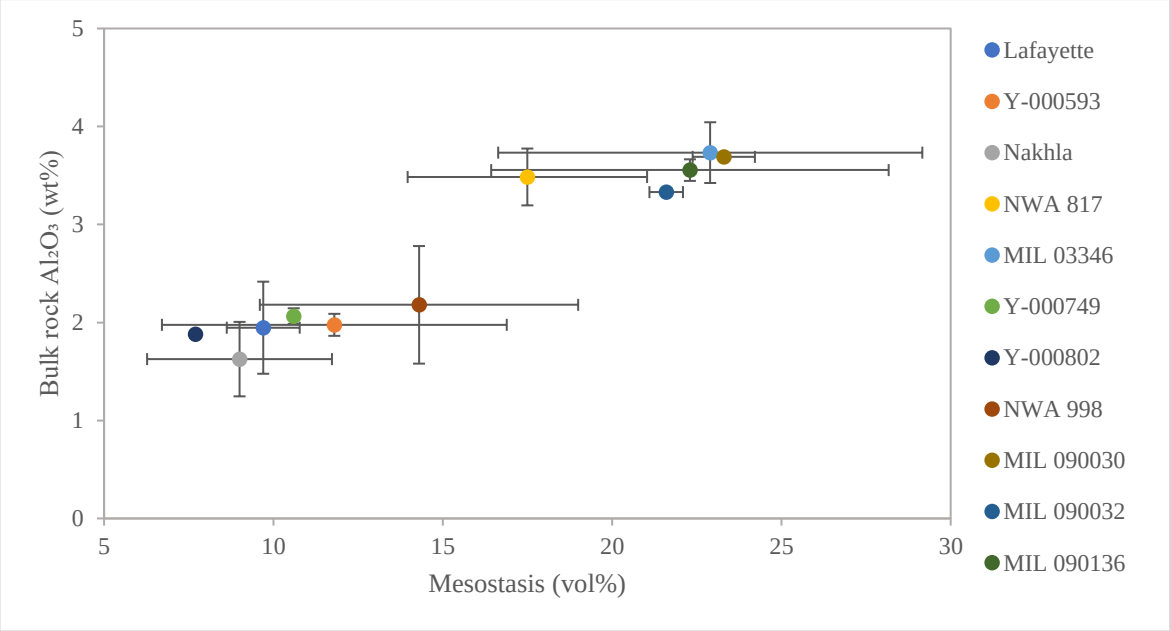

Figure 39 – Graph of bulk rock Al_2O_3 (wt%) versus mesostasis content (vol%) taken from a compilation by Corrigan *et al.* (2015). Black bars are standard deviations. Where not shown, the standard deviation is zero or not applicable (since the value is an "average" of only 1 value).

Figure 39 shows that the bulk rock Al_2O_3 content correlates to the mesostasis content of the meteorite – supporting the hypothesis that the mesostasis content explains the bimodal distribution of bulk rock Al_2O_3 content observed in Figure 8. The 'gap' in an otherwise continuous trend in bulk rock Al_2O_3 versus mesostasis content may be filled by including other nakhlites not considered in this study (*e.g.* NWA 11013 and Governador Valadares).

Regarding the composition versus crystallisation age graphs in Figure 9, it is important to consider that, for crystallisation age to accurately reflect depth below the surface, it is necessary to make the large assumption that the nakhlite launch site was a simple stack of lava flows with no other complications. With this assumption in mind, these graphs detail the varying composition of olivine-hosted iddingsite with depth below the surface for five nakhlites. Observe iddingsite MgO and bulk rock MgO content exhibiting the same trend with age. This is in agreement with findings in Lee *et al.* (2018), where they also observe the same trend in both bulk rock and iddingsite MgO content with crystallisation age. Other oxides (*e.g.* Al_2O_3 and CaO) do not exhibit an identical relationship with varying crystallisation age between the iddingsite and bulk rock content. The total wt% can be seen to decrease with increase age which, assuming a lower total wt% insinuates a greater water content, implies an increase in the water content of iddingsite at greater depths below the surface. Although, it is important to note that total wt%, as determined by EDX or electron probe microanalysis, can be affected by other factors (*e.g.* porosity) – not just water content.

The Nakhlite1 APT reconstruction and isosurfaces in Figure 10 allow valuable insight into the nanostructure of iddingsite and the incorporation of water within NWA 817. The water-species-dense region towards the top of the reconstruction is identified as an opal-A nanoparticle, based on similarities to work by Lee *et al*. (2015). They find that opal-A nanoparticles comprise the majority of the hydrous Mg- and Fe-rich silicate that is a main component of iddingsite in Nakhla. TEM and EELS data in their paper reveal that these opal-A deposits are 5 – 29 nm in diameter and have a lower Mg and Fe content compared to the encapsulating material. This is consistent with the present project, where the water-dense region shown in Figure 10 is roughly 20 nm in diameter and has lower Fe and Mg content compared to the rest of the reconstruction. Areas of low density in the isosurfaces could represent areas of porosity in the iddingsite and areas of high density could be reflecting areas richer in iron oxides or iron oxyhydroxides (further supported by these high-density regions typically overlapping with areas of higher water species density). This observation of opal-A in NWA 817 iddingsite builds upon work by Lee *et al*. (2015), which looked only at iddingsite in Nakhla, and, as they discussed, carries implications for the properties of the altering Martian fluid. For example, they conclude that the retention of opal-A nanoparticles suggests little-to-no further water interaction after iddingsite formation (since the nanoparticles would be further altered to opal-CT and then microcrystalline quartz otherwise).

The Nakhlite2 reconstruction and isosurfaces in Figure 11 detail the distribution of elements across an olivine-iddingsite interface in NWA 817. Iddingsite is observed to have greater Al, Mn, Ca, and Fe concentrations compared to its host (olivine), and a greater concentration of water species – as expected of the aqueously altered material. The 1-dimensional concentration profile in Figure 12 allows the gradients of species through the olivine-iddingsite boundary to be evaluated. Passing from olivine into iddingsite, a decrease in Mg is accompanied by an increase in calcium, hydrogen, and water species. Fe is observed to initially rise and then fall again past the interface and Mn and Al can be seen to slightly increase. Before the sharp changes in concentrations at roughly 55 – 60 nm, species can be observed to marginally increase or decrease in concentration over the preceding 15 – 20 nm (*e.g.* Mg concentration trends slightly downwards from around 35 – 55 nm before sharply dropping). This observation is consistent with work by Daly *et al*. (2019a), where they highlight that this provides insight into the mechanism of the nakhlite alteration (favouring a diffusion coupled hydration model).

4.1.2 Aqueous Environment at the Nakhlite Launch Site

The objective of this project's Martian meteorite study was to build upon and extract new information concerning the past habitability of Mars by investigating the nakhlite aqueous alteration. Accordingly, this section will interpret the nakhlite results and analyses in the context of this research goal. Considering the nakhlite launch site, there are two scenarios, with largely different habitability implications, for the alteration of the nakhlites at 633 Ma:

> **Scenario A:** An active hydrothermal system (either volcanic (Lee *et al.*, 2018) or impact-induced (Daly *et al.*, 2019b)) provided a constant source of thermal energy which caused melted permafrost and ground water to circulate in the Martian subsurface for potentially millions of years (Abramov and Kring, 2005; Li *et al.*, 2014).
>
> **Scenario B:** A transient water source (*e.g.* ice melted by a nearby event) only briefly permeated the nakhlite rocks.

Figure 40 is a depiction of these two scenarios.

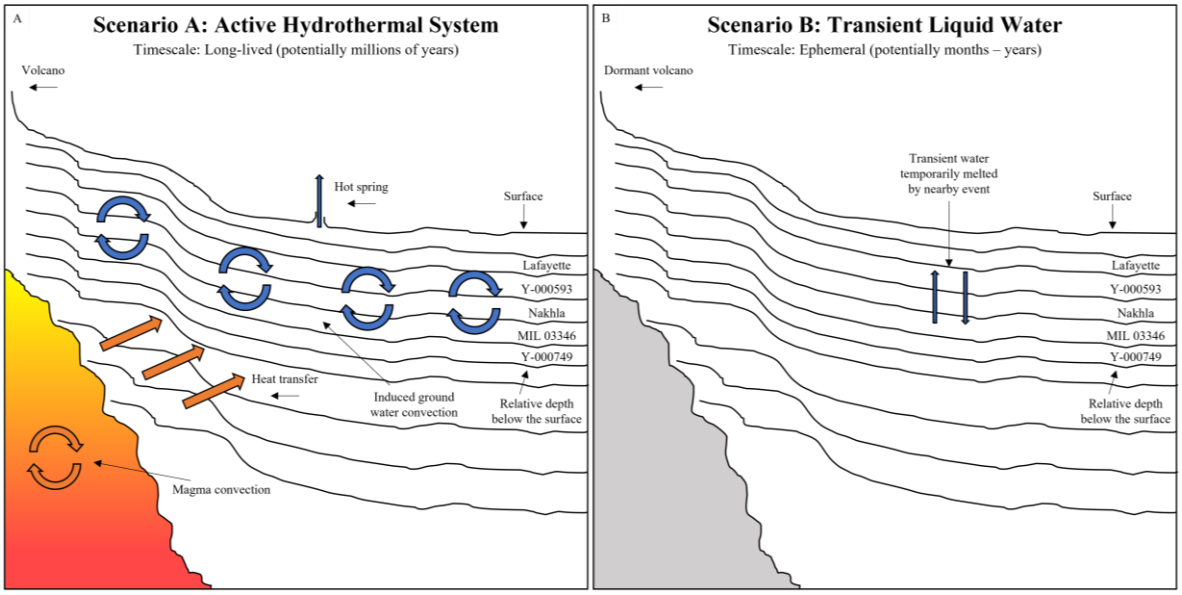

Figure 40 – Illustration of two potential end-case scenarios of the aqueous alteration of the nakhlite meteorites at 633 Ma. A) Scenario A represents an active hydrothermal system (in this case, the diagram is of a simplified volcanic hydrothermal system, but an impact-induced hydrothermal system is also possible). The thermal energy provided by the magmatic (in the volcanic case) heat source could have melted permafrost and ground ice – inducing a cycle of circulating ground water within the Martian subsurface. Hydrothermal systems, such as these, have been shown to last for potentially millions of years (Abramov and Kring, 2005; Li *et al.*, 2014) and can result in the birth of hot springs (Osinski *et al.*, 2001; Cady *et al.*, 2018). B) Scenario B represents an environment in which a nearby event (*e.g.* an adjacent volcanic eruption) provided enough energy to temporarily melt ground ice that would create a source of transient liquid water that briefly percolated the nakhlite rocks. In both diagrams, the relative depth below the surface (as crystallisation ages determined by Cohen *et al.* (2017) suggest) of a subset of the nakhlite meteorites is presented (although, these nakhlites are not necessarily of neighbouring origin and there may be other nakhlites in between). It should be noted that these diagrams are not to scale, and the exact lateral position of the nakhlite rocks (*i.e.* their proximity to the magma source) is not suggested by their position on the diagram.

Importantly, Scenario A and Scenario B present vastly different habitability potentials for the past Martian environment:

Scenario A habitability factors:

- Constant inflow of heat serves to sustain temperatures that are favourable to known life (Cockell *et al.*, 2016).
- Melted permafrost and ground ice provide a source of liquid water which is essential for all known life (Cockell *et al.*, 2016).
- The dynamic liquid water circulation (orchestrated by the magmatic heating) may, via water-rock reactions, maintain an environment which produces thermodynamic disequilibria that can fuel chemolithotrophs (a life-necessary source of energy (Cockell *et al.*, 2016; Ramkissoon *et al.*, 2021)).
- May be accompanied by resultant hot springs which present a favourable environment to the proliferation (and preservation) of life (Walter and Des Marais, 1993; Cady *et al.*, 2018).
- Environment can persist for millions of years (Abramov and Kring, 2005; Li *et al.*, 2014) – allowing time for any life to establish and flourish.

Scenario B habitability factors:

- Does not necessarily possess a persisting thermal energy source that would maintain temperatures conducive to life – potentially impeding metabolic activity (Cockell *et al.*, 2016).
- Water-rock ratios could be very low which would limit microbial access to a key resource – liquid water (Cockell *et al.*, 2016).
- Absence of a lasting heat source likely precludes the development and sustainment of hot spring systems – excluding a life-favourable environment (Cady *et al.*, 2018).
- The transient liquid water may not persist for any substantial amount of time before refreezing – possibly preventing any microbial life from propagating (Cockell *et al.*, 2016).

These different environments may be reflected in the extent and characteristics of the aqueous alteration present in the nakhlites (Changela and Bridges, 2010; Lee *et al.*, 2018; Daly *et al.*, 2019b). Thus, the high-habitability-potential Scenario A and the low-habitability-potential Scenario B can be differentiated by understanding the conditions of the nakhlite aqueous alteration. In a high water-rock ratio environment (Scenario A), the composition of the iddingsite will be primarily controlled by the composition of the altering

fluid. Whereas, in a low water rock-ratio system (Scenario B), the iddingsite composition will be dominated by that of the bulk rock. Thus, in Scenario B, it is expected that iddingsite oxide composition versus bulk rock oxide composition graphs will exhibit directly proportional relationships – where a greater bulk rock composition will result in a greater iddingsite composition for a specific oxide. It would also be expected that the iddingsite composition versus crystallisation age (and thus depth) relationship will essentially mirror that of the bulk rock composition versus crystallisation age. That is, although bulk rock values will not necessarily exhibit any explicit trend with depth below the surface, the iddingsite composition of rocks at a specific depth will reflect the bulk rock composition at that depth – resulting in the same trend versus crystallisation age for both iddingsite and bulk rock oxides.

Two observations agree with these factors defining a low-water rock ratio environment. That is, a strong direct relationship between iddingsite MgO and bulk rock MgO, and the same relationship with age (depth) for both iddingsite MgO and bulk rock MgO. These observations are consistent with Scenario B – predicting a static and less-hospitable ephemeral alteration of the nakhlites at 633 Ma. Meanwhile, other factors are inconsistent with this rock-controlled scenario. These being no direct relationship between iddingsite and bulk rock for Al_2O_3 and CaO, and different age relations between the iddingsite and bulk rock content for both Al_2O_3 and CaO. By contradicting the low water-rock ratio Scenario B, these observations support the dynamic and high-water rock ratio Scenario A for the nakhlite alteration.

APT, if given more attention, holds the potential to assist in deciding between these two scenarios. For example, this project's APT work identified an opal-A nanoparticle in NWA 817 iddingsite. Opal-A retention can suggest little-to-no further water-rock interaction after iddingsite formation (Lee *et al.*, 2015) – which is consistent with a transient alteration, *i.e.* Scenario B. Further, the 1-dimensional concentration profile revealed that olivine is enriched in water species (*e.g.* OH) in the 15 – 20 nm preceding the iddingsite interface. This outward diffusion of water from iddingsite into the surrounding olivine could potentially be used to constrain the longevity of aqueous alteration by understanding the time that this outward diffusion takes. Since the two scenarios for the nakhlite launch site have differing timescales of alteration, this line of investigation may assist in deciding between an ephemeral or long-lived aqueous alteration of the nakhlites.

Thus, evidence is presented supporting both Scenario A and Scenario B for the alteration of the nakhlites and APT holds the potential to further assist in deciding between these scenarios. Scenario B is ultimately favoured as the true nature of the nakhlite launch site because of the clear direct relationship between bulk rock and iddingsite MgO and their agreeing relationships with crystallisation age (plus opal-A in NWA 817) – heavily suggesting a rock-controlled low water-rock ratio environment.

4.1.3 MSR Implications

The Perseverance rover on Mars has recently identified olivine, pyroxene, and their aqueous alteration materials within rocks in the Jezero crater (Farley *et al.*, 2022; Y. Liu *et al.*, 2022), where it is currently collecting samples for their eventual return to Earth (as early as 2033 (mars.nasa.gov, 2022)). Since the primary constituents of the nakhlite meteorites are these minerals (and their alteration products (Lee *et al.*, 2018)), in-depth laboratory investigation of the nakhlites potentially presents the most suitable analogue for the complex on-Earth analyses (Beaty *et al.*, 2019) of returned samples. The present project has demonstrated how compositional trends in alteration materials in the nakhlites can be investigated to better understand the nature of their aqueous alteration. It is also hoped that the nakhlite APT work (investigating mineralogy, incorporation of water, and elemental distributions in iddingsite at the atomic scale) has contributed to displaying the exceptional value of APT in investigations of this nature – building on the efforts of Daly *et al*. (2020, 2021). Thus, viewing this nakhlite study as an analogue, this project can inform and guide the analysis of the samples returned via an MSR mission (*e.g.* concerning the aqueous alteration of rocks in the Jezero crater – which will be a key facet of interrogation of the dried-up crater lake (Beaty *et al.*, 2019)).

4.1.4 Further Work

This work, whilst increasing the number of meteorites considered in Lee *et al.* (2018) from four to 11, is not a comprehensive review of the nakhlites. Ideally, a more complete study would include even more nakhlites (*e.g.* Governador Valadares, NWA 11013, NWA 10153, *etc*.) and would also consider pyroxene-hosted iddingsite veins (not just olivine-hosted). However, there was a lack of published data for some nakhlites (*e.g.* NWA 11013 and Y-000802) concerning the composition of the bulk rock and of the iddingsite. Data from these

remaining meteorites would allow a more thorough review of the iddingsite versus bulk rock composition relationships – assisting in deciding between Scenario A and Scenario B for the alteration of the nakhlites. To ensure consistency, iddingsite and bulk rock oxide compositions were compared against crystallisation age data collected in a singular study (by Cohen *et al*. (2017)). Although improving the set of considered meteorites from the three in Lee *et al*. (2018) to five by now including the age data for Y-000593 and Y-000749, the robustness of observed trends with crystallisation age is still limited. Ideally, there would be a single study where the crystallisation ages of a larger number of nakhlites would be determined under the same conditions and in the same laboratory. This would allow trends against age (like versus iddingsite and bulk composition performed here) to be examined with much greater confidence and depth – facilitating insight into the nature of the nakhlite alteration.

It should be noted that, despite attempts to do so, the APT mass spectra for both the Nakhlite1 and Nakhlite2 reconstructions are not fully assigned, and proper assignment of the Fe and Si peaks was not possible due to isobaric interference – resulting in figures being not entirely representative of the samples. Ideally, mass spectra would be fully assigned and isotopes with unique atomic weights examined to properly distinguish the Fe and Si content (*e.g.* as done by J. Liu *et al*. (2022)). An APT study across a wider range of iddingsite samples across multiple nakhlite meteorites would allow deeper and likely novel insight into the nature of their aqueous alteration – further assisting in deciding between Scenario A and Scenario B for the nakhlite launch site.

4.2 Terrestrial Analogues

4.2.1 Insight into Preserved Fossils

This project investigated fossiliferous Rhynie chert and Yellowstone hydrothermal samples via an analytical pipeline – resulting in good insight into the fossils preserved within. Rhynie chert investigations revealed fossils of *Asteroxylon* plant cells and fungal species (fungal spores, chlamydospores, and chytrids) very well preserved within the chert matrix by siliceous permineralization. Yellowstone investigations identified fossilised plant cells from a siliceously-preserved *Magnolia spectabilis* leaf.

Raman investigations were able to confirm the presence of carbonaceous material within the fossils across both samples and also rule out the epoxy resin (used in thin section production) as the source of these signals. Deconvolution of these carbonaceous material peaks suggests a peak metamorphic temperature of 100 – 210 °C for the Rhynie sample and 125 – 185 °C for YellowstoneA – acting as a geothermometer probing the thermal history of these samples and environments. Although, the Yellowstone sample will not have been heated for as long as the Rhynie chert, so the calculated "metamorphic" temperature may not be accurate. The Rhynie result is agreement with work by Qu *et al*. (2015), where they calculated a peak metamorphic temperature of roughly 190 – 310 °C for the Rhynie chert sample but admit that the remarkable preservation of fossils in the Rhynie chert likely implies peak temperatures of only 200 °C. Since these peak metamorphic temperatures are less than 360 °C (for both the Rhynie chert and Yellowstone samples), it is expected that a lower R-value will correlate with lower structural order of the carbonaceous material (Qu *et al.*, 2015). Subsequent R-value investigations probed the structural order of the carbonaceous material in the fossils across both the Rhynie chert and Yellowstone samples. Figure 22 map D), an R-value map of a fungal fossil in the Rhynie chert sample, reveals a lower R-value (thus implying a lower structural order) in the wall of the cell compared to the intracellular material. This finding is inconsistent with results by Qu *et al*. (2015), where they concluded that Rhynie chert fossilised plant cells displayed higher structural order in cell walls compared to the plant protoplasm. Although, plant cells may not be directly comparable to the fungal cells tested in the present project. Further, Figure 22 map D) was produced before baseline removal – where no explicit trends are observed in the same Raman map after the baseline was removed (Figure 22 G)). For the Yellowstone Raman R-value map (Figure 23 D)), there is little information except a difference in R-values observed between the fossilised plant cells and the surrounding rock. This may have been due to the scale at which this map was captured being too large to resolve any R-value (and thus structural order) differences on the cellular level.

SE imagery detailed the topography of a fungal fossil in the Rhynie chert and fossilised *Magnolia spectabilis* leaf cells in the Yellowstone sample. EDX then revealed that areas of increased carbon counts generally corresponded to areas deeper in the thin section. This may be due to deeper areas exposing more of the preserved fossils to the surface or areas of thicker carbon coating (applied in sample preparation) due to the differing topography. Electron diffraction patterns confirmed the identity of the material encapsulating the fossils in the Rhynie chert to be quartz – as expected. Bright-field images revealed a non-crystalline

inclusion in a sample from the cell wall of a fungal fossil in the Rhynie chert – which was postulated to be preserved organic carbon. Subsequent STEM and EELS work on both the Rhynie chert and Yellowstone samples was conducted to further investigate the preserved carbon. EELS data revealed that dark areas in HAADF images corresponded to carbon. The identity of this carbon is presumed to be the actual preserved carbon, and not simply the carbon coating, since the electron-transparent slices have been milled from the thin sections – extending up to 10 µm deep (where the applied carbon coating likely could not reach) – yet carbon is still observed. Epoxy resin cannot be definitively discounted, but the preceding Raman work suggests that there is non-epoxy-resin carbonaceous material in the fossils – improving confidence that the observed carbon is the actual preserved carbon. TEM and STEM HAADF images could then be used to understand the distribution of carbon within the whole electron-transparent samples, rather than just the areas already interrogated by EELS. This revealed a difference in the distribution of preserved carbon between Rhynie chert and Yellowstone fossils. Carbon in the cell wall of the Rhynie chert fungal fossil was scattered throughout the whole electron-transparent slice – appearing to inhabit the space between crystals. Meanwhile, carbon in the fossilised Yellowstone plant cells was mainly concentrated into larger streaks within the samples. Overall, this TEM work revealed that, despite the fossils in both the Rhynie chert and Yellowstone samples appearing to consist of abundant and continuous organic matter under optical microscopy (*e.g.* as seen in Figure 15 and Figure 16), preserved carbon is actually sporadic and discontinuous at the nm scale.

4.2.2 Ancient versus Recent Preservation

Since Martian hydrothermal systems are mostly long since extinct (Turner *et al.*, 2016), the better understanding of the effect of such timescales on the preservation of biosignatures is vital in the search for Martian biosignatures and, thus, the analysis of returned Martian samples. The Rhynie chert and Yellowstone samples were chosen as the Mars analogues in this project in part because of the comparison they allow between recent versus ancient preservation of biosignatures. Yellowstone fossils were preserved recently compared to over 400 million years ago for Rhynie chert fossils (Mark *et al.*, 2011; Parry *et al.*, 2013). In the present project, a difference in the distribution of preserved carbon is observed between Rhynie chert and Yellowstone fossils. This could be the result of geological timescales on the preservation of biosignatures (fossils) or simply differences in the nature of their siliceous preservation. To expand on this idea, a study could survey the nm-scale preservation of fossils in a greater number of samples in the Rhynie chert, Yellowstone, and

potentially other fossiliferous hydrothermal samples of differing ages – further investigating this MSR-relevant effect.

4.2.3 Guiding MSR Biosignature Investigations

A goal of this project was to guide the investigation of returned Martian samples by analysing Mars analogues. This section will summarise the value of each technique in the pipeline regarding the study of preserved fossils – highlighting how these techniques could be collaboratively employed to investigate analogous returned Martian samples in the search for preserved biosignatures.

Optical Microscopy: Provided mineralogical characterisations of samples and identified the presence, abundance, and distribution of preserved fossils. Also probed the depth of fossils in the thin section – important for later surface-sensitive techniques.

Raman Spectroscopy: Identified the presence of carbonaceous material within preserved fossils. Detailed the thermal history of the samples and investigated the structural order of preserved carbon in the fossils.

SEM: Detailed topography and elemental composition of fossils. Assisted in locating fossils in subsequent milling by FIB.

TEM: Confirmed the identity of encapsulating crystalline material. Provided exceptional insight into the identity, distribution, and incorporation of organic carbon within the preserved fossils at the nm scale.

In summary, the analytical pipeline was effectively utilised to identify, investigate, and characterise siliceously preserved fossils within two Mars terrestrial analogue samples from the whole-rock scale down to the nm scale – demonstrating and informing how these techniques could be collaboratively employed on future returned Martian samples in the search for preserved biosignatures. Remarkably, the pipeline displayed the ability to directly investigate carbon preserved within fossils of some of the oldest known plant life on Earth (Rhynie fossils (Rice *et al.*, 2002)) – a favourable sign for MSR investigations where any hydrothermally-preserved fossils are likely to be ancient (Turner *et al.*, 2016). Figure 41 is a summary of the analytical pipeline as employed to investigate fossils in the Rhynie chert and Yellowstone samples.

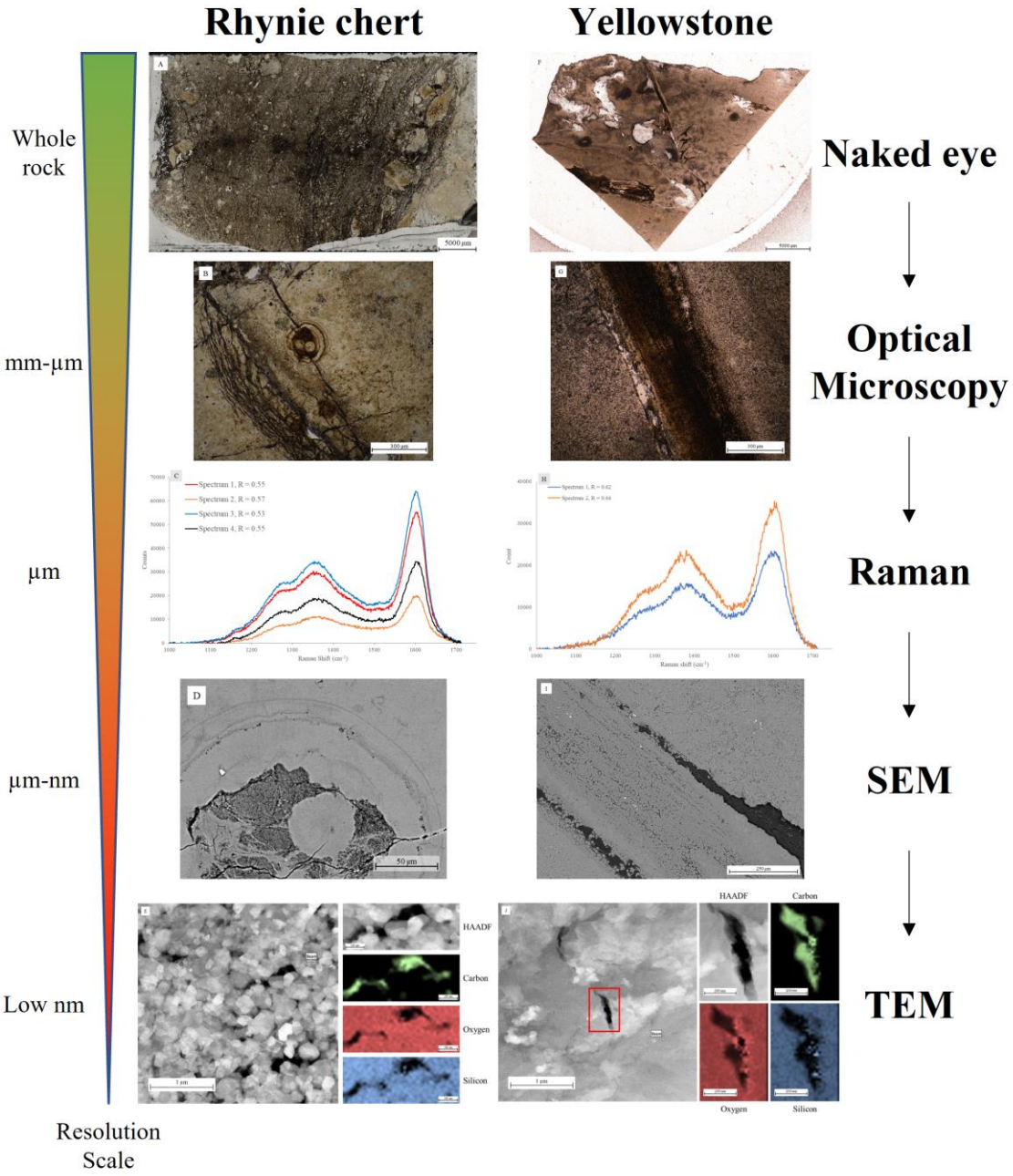

Figure 41 – The the analytical pipeline as employed to investigate fossils in the Rhynie chert and Yellowstone samples. Tapered bar on the left illustrates the ever-increasing resolution of the pipeline, highlighting the scientific power arising from the correlative and successive usage of employed analytical techniques. Note: the resolution steps in the bar are not to relative scale and are instead representative of the achievable resolution at each step in the pipeline. The first column (images A) – E)) corresponds to this project's utilisation of the analytical pipeline on the Rhynie chert samples to investigate the supposed fungal spore or chytrid from Rhynie3 AreaC – progressing from the whole-rock scale down to the nm scale. Specifically, A) is an optical microscopy collage image of the whole Rhynie3 polished thin section (used to represent the whole-rock scale); B) is an optical microscopy image of the fossil; C) is overlayed Raman spectra of regions within the fossil with annotated R-values; D) is a BSE image of the fossil acquired by SEM; and E) is a TEM HAADF image of an electron-transparent slice lifted from the fossil with a STEM HAADF image and three EELS maps to the right that are labelled with the respective element that they represent. The second column (images F) – J)) similarly represents this project's employment of the analytical pipeline on the preserved *Magnolia spectabilis* leaf within the Yellowstone samples. Specifically, F) is an optical microscopy collage image of the entirety of Yellowstone1 (representing the whole-rock scale); G) is an optical microscopy image of Yellowstone1 AreaA; H) is two overlayed Raman spectra from Yellowstone1 AreaA with their R-values annotated; I) is an SEM BSE image of Yellowstone1 AreaA; and J) is a TEM HAADF image of an electron-transparent slice milled from Yellowstone1 AreaA with a STEM HAADF image to the right accompanying EELS maps representing the carbon, oxygen, and silicon content. The last column details the respective stage in the analytical pipeline that the information to the left was acquired in. This figure highlights how the pipeline can be utilised to go from the whole-rock scale to in-depth investigations into features at the nm scale (*e.g.* preserved carbon in fossils) – displaying the prowess of this analytical method and, thus, advocating for its eventual usage on returned Martian samples in the search for preserved biosignatures.

Despite the wealth of information produced concerning fossils within the Rhynie chert and Yellowstone samples, the analytical pipeline possessed potential pitfalls and areas that could be improved.

4.2.4 Analytical Pipeline Recommendations

In accordance with a main project goal (*i.e.* developing and evaluating the analytical pipeline), this section will discuss key issues encountered throughout this project's use of the analytical pipeline in the analysis of terrestrial analogues – whilst proposing potential solutions and improvements for the hypothetical eventual usage of this methodology in the interrogation of returned Martian samples in the search for preserved biosignatures.

Recommendation 1: Establish a large catalogue of near-surface features early in the analytical workflow.

Later instruments in the analytical pipeline (*e.g.* SEM and FIB) require features to be sufficiently close to the surface of the thin section in order to be accessed – which was feared to have been an issue encountered by the fossils examined by SEM EDX in this project. It is here recommended that a future utilisation of this analytical pipeline on returned Martian samples (or otherwise) in the search for preserved biosignatures should expend sufficient effort in the identification of a large library of potentially-close-to-the-surface features before progressing to the later steps in the workflow. It is also recommended that ample attention is given to the methodology by which surface proximity is determined – ideally combining thorough reflected light inspection and in-depth z-stack interrogation. In doing so, there will be an increased likelihood that features chosen to be further inspected will be shallow enough to be accessed by the surface-sensitive techniques – potentially avoiding wasting time and resources interrogating features which ultimately cannot be further investigated due to their depth within the thin section.

Recommendation 2: Introduce infrared spectroscopy (henceforth IR spectroscopy) to complement initial characterisations by Raman spectroscopy.

Although Raman spectroscopy was able to provide valuable information regarding the preserved fossils in the Rhynie chert and Yellowstone samples (*e.g.* structural order of preserved carbon), insight into the nature of preserved organics was limited. It is thus recommended that future interrogations concerning preserved biosignatures (in returned

Martian samples or otherwise) further incorporate the highly-complementary technique – IR spectroscopy (Olcott Marshall and Marshall, 2015; Farber *et al.*, 2019). As demonstrated by Qu *et al*. (2015), the correlative utilisation of IR spectroscopy with Raman spectroscopy can permit strong insights into the identity of preserved organics – where they were successfully able to interrogate the organic precursor molecules and the nature of preservation of carbonaceous material within siliceously preserved fossils. Additionally, there exists literature attesting to the potential ability of combined IR spectroscopy and Raman spectroscopy to assess the biogenicity of fossils (Igisu *et al.*, 2006; Olcott Marshall and Marshall, 2015) – a crucial factor in potential biosignature investigations (Ohmoto *et al.*, 2008). These examples highlight the potential of IR spectroscopy to complement an analytical workflow's Raman organic investigations (*e.g.* into future returned Martian samples in the search for preserved biosignatures).

Recommendation 3: Consider inspecting thin sections under SEM and EDX prior to coating the sample.

Confidence in this project's SEM EDX data was potentially impeded by the conductive coatings that were applied to the surface of the thin sections prior to inspection under the SEM – where the roughly 15 nm gold coating was presumed to be possibly inhibiting signals and the roughly 20 nm carbon coating was hypothesised to be interfering with the collection of true carbon signals. It is thus recommended that future preserved biosignature investigations (*e.g.* on returned Martian samples) should attempt, if practical, to inspect any produced thin sections via SEM before any conductive coating is applied. In doing so, any interference that the coating may exert on data collection can be avoided. Although, in order to reduce surface charging in the absence of a conductive coating, different countermeasures are required (*e.g.* operating in lower vacuum conditions) which can result in lower image quality and additional artefacts in EDX (Newbury, 2002; Nylese *et al.*, 2015). This methodology (*i.e.* performing SEM and EDX analyses before applying a coating) is demonstrated by Nakamura *et al*. (2021) on returned Ryugu samples. They were able to utilise EDX (along with SEM imaging and TEM) on non-coated samples to produce a detailed description of the mineralogy and elemental distribution of the samples. The setbacks experienced by the present project, along with the returned asteroid example, further highlight the option of SEM and EDX analyses taking place prior to the coating of future returned Martian samples – to potentially procure stronger insights into the carbon content of preserved features.

Recommendation 4: Chose features for TEM inspection that are positionally close together on a given thin section.

The FEI Nova Nanolab 200 FIB operated in this project to mill samples to electron-transparency presented an unforeseen drawback when producing TEM samples from the Rhynie chert. It was intended that the FIB would be conducted to mill slices from both Rhynie3 AreaA and Rhynie3 AreaC – to procure a more comprehensive understanding of the sample. However, the FIB utilised in this project possessed a limited accessible stage area which, once the thin section was mounted, was unable to simultaneously encapsulate both Rhynie3 AreaA and Rhynie3 AreaC (which were located at opposite ends of the polished thin section). In order to mill from both areas, it would have required the sample chamber to be vented, the thin section re-mounted, and the vacuum pulled again in the sample chamber – which can be time-consuming (and thus expensive). As such, it was decided to take 2 electron transparent slices from Rhynie3 AreaC which, although providing useful information, potentially limited the scope of the TEM information produced in this utilisation of the pipeline. Therefore, it is here recommended that, where FIB stage size limits thin section access, features chosen for TEM inspection on future returned Martian samples should ideally be close together – permitting milling of desired features without the need for the time-consuming adjustments that would accompany re-mounting of thin sections.

Recommendation 5: Utilise APT as the culminating technique in the pipeline, following analyses by TEM.

As demonstrated by this project's usage in the analysis of the nakhlites, on top of multiple works displaying the prowess of the technique (Daly *et al.*, 2020, 2021; J. Liu *et al.*, 2022; McCarroll *et al.*, 2022), APT stands to serve planetary science research greatly – resulting in isotopically-detailed 3-dimensional reconstructions of a sample at the atomic scale. Thus, although not employed on the analogue samples in this project, it is here recommended that any future utilisations of the analytical pipeline (*e.g.* on returned Martian samples in the search for preserved biosignatures) should consider the usage of APT. It should be noted that, due to the limited size of individual APT samples (*i.e.* up to around 100 nm x 100 nm x 1000 nm (Daly *et al.*, 2020)), it may prove challenging to pinpoint features of interest at small scales without extensive context and guidance built by previous techniques. Figure 42 highlights that an APT needle would need to be precisely milled in order to incorporate any of the key preserved carbon in the Rhynie3 AreaC fossil sample.

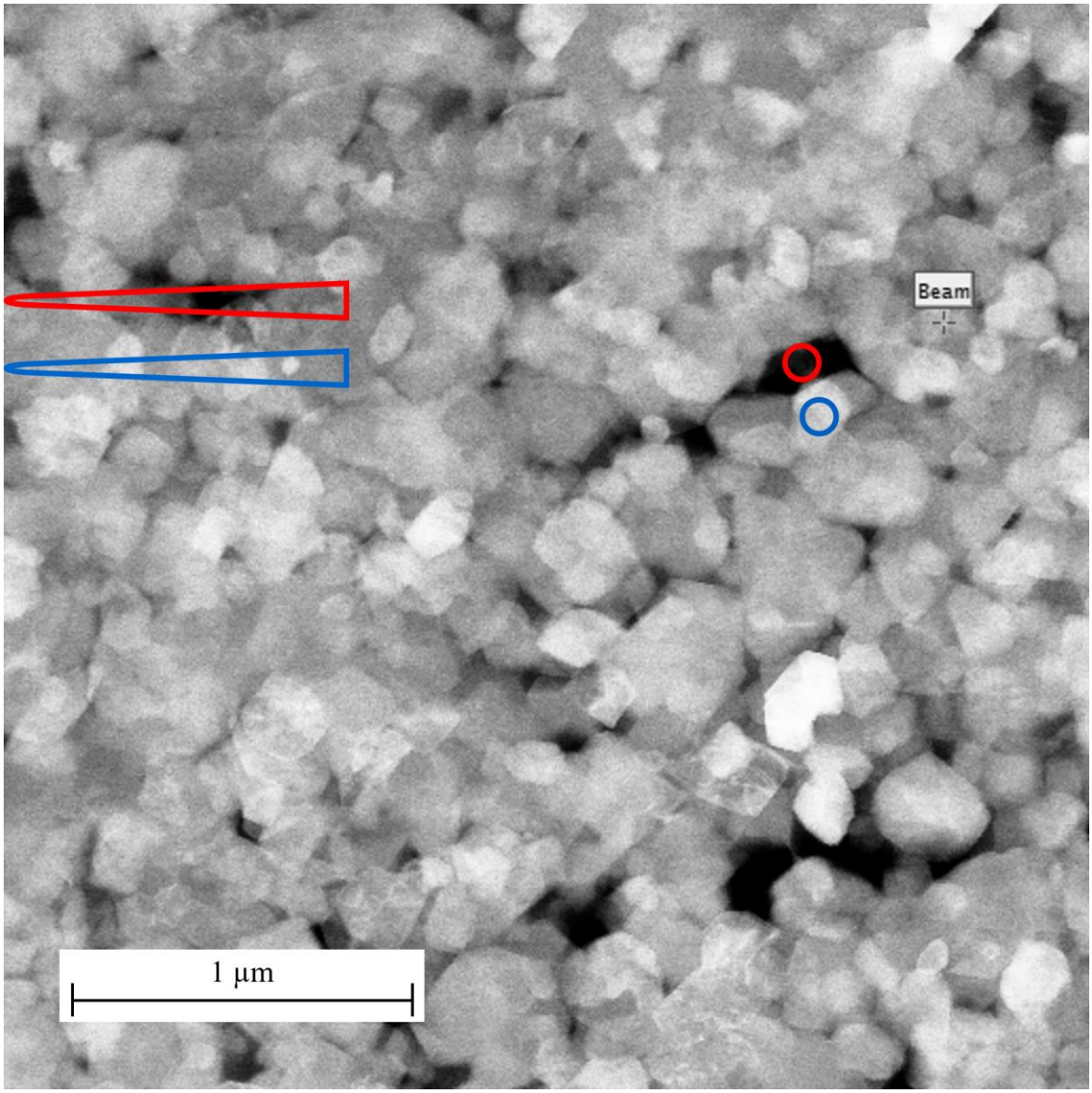

Figure 42 – A standard TEM HAADF image of Rhynie3 Slice4 which is annotated with red and blue circles that represent the maximum size of individual atom probe needles as milled normal to the plane of the image (*i.e.* laterally 100 nm x 100 nm (Daly *et al.*, 2020)) plus annotated red and blue needles representing the maximum size of APT samples as milled in the plane of the image (*i.e.* at 90° to the circles and reaching up to 1000 nm deep (Daly *et al.*, 2020)) – where the left-hand side of the image hypothetically represents the surface of a thin section sample. It is clear that, whilst the red annotations would incorporate some of the key carbon, the blue APT needles would likely not contain any of the preserved carbon despite being mere nanometres off. This highlights the necessity of extensive context built from previous analytical steps (*e.g.* SEM and TEM) to guide the FIB milling of APT samples. The "Beam" textbox and crosshairs are merely digital artefacts annotated atop the image.

Thus, although APT possesses promising prospects for planetary science purposes (Daly *et al.*, 2020, 2021; McCarroll *et al.*, 2022), care should be taken to consider the scale and necessary context for its successful employment in future applications of the pipeline.

This concludes the Discussion chapter of the thesis, where the results have been discussed and interpreted in respect to the project goals and their relation to the literature. The subsequent chapter, Conclusions, will finalise the thesis by summarising the key results in terms of answering the research questions that this thesis set out to answer.

5. Conclusions

This project set out to advance the understanding of Martian habitability in preparation for the eventual return of Martian samples to Earth as part of an MSR mission. Specifically, the research undertaken in this project was orchestrated in order to tackle three main research questions. To summarise:

Question 1 – What further information can be garnered concerning the past habitability of Mars from the investigation of the aqueous alteration of the nakhlite Martian meteorites?

Following work by Lee *et al*. (2018), this project has explored the investigation of nakhlite iddingsite and its potential to illuminate the nature of the nakhlite launch site's aqueous alteration at 633 Ma. In particular, trends in the bulk composition, iddingsite composition, and their relationship with crystallisation age (*i.e.* depth) were investigated to help distinguish between two end-case scenarios for the nakhlite alteration. These are a low water-rock ratio, ephemeral, interaction or a high water-rock ratio, potentially long-lived, hydrothermal environment – which present vastly differing habitability potentials (Cockell *et al.*, 2016). It was found that:

- Observed trends supporting an ephemeral interaction and a hydrothermal environment as the true nature of the Nakhlite launch site's aqueous alteration.
- A low water-rock ratio transient alteration is ultimately favoured.
- APT holds the potential to provide novel insight into the nakhlite alteration – assisting in discerning between these end-case scenarios.

Thus, in accordance with the first main project goal, this project has further developed the interrogation of Martian meteorites in order to garner deeper insights into the past habitability of Mars.

Question 2 – Can the interrogation of the Rhynie chert and Yellowstone Mars terrestrial analogue sites guide and inform the analysis of returned Martian samples in the search for preserved biosignatures?

One purpose of the inspection of the Rhynie chert and Yellowstone samples under the analytical pipeline was to demonstrate how these techniques could be collaboratively employed to gain strong insights into preserved fossils – serving to guide and inform the

eventual analysis of returned Martian samples in the search for preserved biosignatures using this analytical strategy. It was shown that:

- Methodology detailed in this project produced a wealth of information regarding preserved fossils – demonstrating their potential usage on returned samples.
- Highlighted analytical avenues can be useful lines of investigation for interrogating preserved organic features in returned samples.

Therefore, fulfilling the second main research goal, the successful utilisation of the analytical pipeline on the Rhynie chert and Yellowstone fossils (and the analytical avenues explored therein) can serve as a demonstration of the correlative usage of these techniques on future returned Martian samples in the search for preserved biosignatures.

Question 3 – Can the analysis of terrestrial analogues develop and evaluate the effectiveness of the analytical pipeline for planetary science applications?

The analytical pipeline was utilised to investigate the Rhynie chert and Yellowstone analogue samples to better describe and understand the siliceously preserved fossils within. The results obtained were used to evaluate the effectiveness of the pipeline in this specific application and its potential effectiveness on returned Martian samples in the search for preserved biosignatures. Furthermore, drawbacks with the pipeline encountered throughout this project's utilisation on the terrestrial analogue samples were discussed in order to improve the pipeline. In summary:

- Strong insights into fossils in the analogue samples displayed the effectiveness of the analytical pipeline.
- Multiple recommendations were proposed to improve the effectiveness of the pipeline in response to key issues – developing the pipeline for future usage (*e.g.* on returned Martian samples).

As such, it has been shown that the analysis of terrestrial analogues can both assess the effectiveness of the analytical pipeline and illuminate areas of potential improvement – ultimately serving to further advocate for the usage of this analytical strategy (and specifically APT) on returned Martian samples in the investigation of preserved biosignatures (and further planetary science applications), thus achieving the final main project goal.

Appendix

Appendix 1 – Nakhlite Compilation Supplementary Information

The nakhlite compilation was updated by incorporating new nakhlite iddingsite composition data obtained by EDX measurements concerning nine nakhlites (Y-000593, Nakhla, Y-000749, Y-000802, NWA 998, NWA 11013, MIL 090030, MIL 090032, and MIL 090136). The EDX data for these nakhlites was collected by Sammy Griffin on the Carl ZEISS Sigma Variable Pressure Analytical SEM at the University of Glasgow, which is equipped with an Oxford Instruments X-Max silicon-drift EDX detector, directed by AZtec microanalysis software. The data was collected following procedure outlined by Lee *et al*. (2018) – *i.e.* using a 20 kV beam with 1 nA current, 60 s count time, high vacuum conditions, and calibrated using similar mineral standards (specifically jadeite, periclase, apatite, pyrite, wollastonite, rutile, rhodonite, almandine garnet, Ni-metal, diopside). Additionally, bulk rock composition data for Y-000802 was included in the compilation as a new data point. This was acquired by James Day following the same procedures, and in the same laboratory, as outlined in both Udry and Day (2018) and Day *et al*. (2018) – *i.e.* by conventional Teflon bomb digestion at the Scripps Isotope Geochemistry Laboratory, where the sample was digested in Teflon-distilled HF and HNO_3 and, after further processing (*e.g.* heating to 150 °C for 72 hours and doping with indium), major element abundances were determined using a ThermoScientific iCAP Qc quadrupole inductively coupled plasma mass spectrometer. This was done such that all of their bulk analyses of the Martian meteorites would be directly comparable.

The new EDX data set was filtered such that the values better reflected those of iddingsite. To do this, a compilation of already published olivine-hosted iddingsite composition values was produced for each nakhlite considered in this study – and the average of the sum of the oxides (*i.e.* the average total weight percentage) was calculated. To then reduce the new data set to be incorporated in this work, data points which had total weight percentages that fell within ±5% of this calculated literature average total weight percentage (for each individual meteorite) were considered to be accurately reflecting EDX measurements of iddingsite and, thus, were to be included in this study. These now-reduced values were then averaged into a single oxide composition value and this average was then incorporated into the olivine-hosted iddingsite composition as an extra data point. Finally, this new compilation (containing the original published literature composition values and the new (reduced and

averaged) value) was averaged and these oxide weight percentage values would then serve as the olivine-hosted iddingsite oxide composition values in subsequent analyses. An example utilisation of this process for Y-000593 is presented in the following working (Appendix Table 1, Appendix Table 2, and Appendix Table 3).

Appendix Table 1 – Example literature-only olivine-hosted iddingsite composition compilation for Y-000593

			Literature-only Olivine Iddingsite Composition (wt%)										
Meteorite		Author(s)	MgO	Al_2O_3	SiO_2	P_2O_5	SO_2	CaO	TiO_2	MnO	FeO	NiO	Total
Y-000593	Vein	Imae *et al*., 2005 (A)	4.80	1.15	52.00	0.00	-	0.04	0.04	0.51	26.25	0.02	84.81
		Imae *et al*., 2005 (B)	4.18	0.07	24.75	0.06	0.86	0.38	0.02	1.74	57.40	-	89.46
		Noguchi *et al*., 2009	3.80	0.56	51.35	-	2.23	0.08	-	0.22	25.66	-	83.90
		Hicks *et al*., 2014	2.50	1.1	37.80	0.10	1.52	0.30	-	1.00	37.89	-	82.21
											Average:		**85.10**

"-" indicates that this value was below detection limits, not tested for, or not stated in the original source material
"(A, B, C, …)" is used to differentiate multiple separate value sets taken from the same source publication

1. ±5% of the average total value from literature

(80.845 —— 85.10 —— 89.355)

Lower Bound (-5%) Upper Bound (+5%)

2. Average of the values with a total lying within these bounds from the new Y-000593 data set

Appendix Table 2 – Example of reduced and averaged new Y-000593 olivine-hosted iddingsite composition values

			Olivine Iddingsite Composition (wt%)										
Meteorite		Author(s)	MgO	Al_2O_3	SiO_2	P_2O_5	SO_2	CaO	TiO_2	MnO	FeO	NiO	Total
Y-000593	Vein	Reduced New Data (Average of 16)	4.22	0.82	40.54	0.12	0.19	0.43	0.03	1.38	35.10	0.03	82.85

3. This average value is added to the literature compilation

Appendix Table 3 – Example of the final, updated, olivine-hosted iddingsite oxide composition compilation for Y-000593

			Olivine Iddingsite Composition (wt%)										
Meteorite		Author(s)	MgO	Al_2O_3	SiO_2	P_2O_5	SO_2	CaO	TiO_2	MnO	FeO	NiO	Total
Y-000593	Vein	Imae *et al*., 2005 (A)	4.80	1.15	52.00	0.00	-	0.04	0.04	0.51	26.25	0.02	84.81
		Imae *et al*., 2005 (B)	4.18	0.07	24.75	0.06	0.86	0.38	0.02	1.74	57.40	-	89.46
		Noguchi *et al*., 2009	3.80	0.56	51.35	-	2.23	0.08	-	0.22	25.66	-	83.90
		Hicks *et al*., 2014	2.50	1.10	37.80	0.10	1.52	0.30	-	1.00	37.89	-	82.21
		Reduced New Data (Average of 16)	4.22	0.82	40.54	0.12	0.19	0.43	0.03	1.38	35.10	0.03	82.85
		Average:	**3.90**	**0.74**	**41.29**	**0.07**	**1.20**	**0.25**	**0.03**	**0.97**	**36.46**	**0.02**	**84.65**

"-" indicates that this value was below detection limits, not tested for, or not stated in the original source material
"(A, B, C, …)" is used to differentiate multiple separate value sets taken from the same source publication

4. New average values used as the Y-000593 olivine-hosted iddingsite vein values in further analyses

It should be noted that for Y-000802, since no literature olivine-hosted iddingsite composition values were found, this process was altered such that the average literature-only total weight percentage (that would serve as the basis for determining the ±5% bounds) was instead calculated by taking the average of the average literature-only total weight percentage of Y-000593 and Y-000749 (which are both paired meteorites of Y-000802). Additionally, due to the inability to locate iddingsite vein composition data, the lack of paired meteorites being considered in this study, and the quality of data which the new EDX data presented, NWA 11013 was excluded from this process – and thus also excluded from further analyses. Similarly, due to a lack of discovered pyroxene-hosted iddingsite composition data and the varied quality of data present in the new EDX data sets, work concerning the relationships of pyroxene-hosted iddingsite was also excluded from further analyses.

Below are the raw data tables for the nakhlite literature compilation, including the new EDX data. These include the individual values, the final averages, and their standard deviations.

Appendix Table 4 – Updated compilation of bulk rock and olivine-hosted iddingsite composition data for the nakhlites

			Oxide Composition (wt%)										
Meteorite		Author(s)	MgO	Al_2O_3	SiO_2	P_2O_5	SO_2	CaO	TiO_2	MnO	FeO	NiO	Total
Lafayette	Vein	Treiman *et al.*, 1993	13.90	4.77	49.10	0.09	0.55	0.70	0.01	0.48	29.01	0.10	98.71
		Kuebler *et al.*, 2004	9.90	4.55	42.20	-	-	1.18	0.04	0.48	27.20	-	85.55
		Changela and Bridges, 2010	9.29	3.02	41.00	-	0.12	1.26	0.06	0.91	27.70	-	83.36
		Hicks *et al.*, 2014	11.30	3.00	41.20	-	0.08	0.90	0.10	0.60	28.59	-	85.77
	Bulk	Boctor *et al.*, 1976	12.90	1.55	46.90	-	-	13.40	0.33	0.79	22.70	-	98.57
		Lodders, 1998	12.90	2.47	46.90	0.45	0.08	13.40	0.42	0.50	21.60	-	98.72
		Udry and Day, 2018	12.00	1.82	49.90	0.12	-	13.50	0.29	0.53	21.40	-	99.56
Y-000593	Vein	Imae *et al.*, 2005 (A)	4.80	1.15	52.00	0.00	-	0.04	0.04	0.51	26.25	0.02	84.81
		Imae *et al.*, 2005 (B)	4.18	0.07	24.75	0.06	0.86	0.38	0.02	1.74	57.40	-	89.46
		Noguchi *et al.*, 2009	3.80	0.56	51.35	-	2.23	0.08	-	0.22	25.66	-	83.90
		Hicks *et al.*, 2014	2.50	1.10	37.80	0.10	1.52	0.30	-	1.00	37.89	-	82.21
		New data set (average of 16)	4.22	0.82	40.54	0.12	0.19	0.43	0.03	1.38	35.10	0.03	82.85
	Bulk	Shirai *et al.*, 2002	10.39	1.88	47.57	0.00	-	14.27	0.29	0.51	19.67	-	94.58
		Imae *et al.*, 2003	11.10	1.91	47.93	0.29	-	14.71	0.47	0.59	21.71	-	98.71
		Oura *et al.*, 2003	10.20	2.00	47.60	-	-	14.30	0.41	0.52	22.40	-	97.43
		Udry and Day, 2018	10.28	2.13	52.00	0.13	-	14.80	0.39	0.48	19.10	-	99.31
Nakhla	Vein	Hallis *et al.*, 2012	6.48	0.16	41.50	-	0.06	0.16	0.05	-	33.20	-	81.61
		Hicks *et al.*, 2014	7.50	0.10	32.00	-	0.08	0.50	-	0.60	36.29	-	77.07
		Lee and Chatzitheodoridis, 2016	8.02	3.29	41.33	-	-	0.76	-	0.41	27.36	-	81.17
		New data set (average of 23)	5.42	0.89	37.95	0.05	0.09	0.49	0.03	0.68	34.62	0.02	80.24
	Bulk	Prior, 1912 (A)	12.00	1.74	48.97	-	-	15.17	0.38	0.09	20.79	-	99.14
		Prior, 1912 (B)	12.20	1.65	49.98	-	-	15.12	-	-	19.58	-	98.53
		Prior, 1912 (C)	14.61	0.69	47.40	-	-	15.20	-	0.85	20.80	-	99.55
		McCarthy *et al.*, 1974	12.47	1.45	48.24	0.12	-	15.08	0.29	0.54	20.63	-	98.82
		Bunch and Reid, 1975	11.80	1.57	47.90	-	-	15.40	0.30	0.50	18.50	-	95.97
		Dreibus *et al.*, 1982	11.82	1.64	49.33	0.10	-	14.30	0.35	0.55	21.70	-	99.79
		Lodders, 1998	12.10	1.68	48.60	0.13	-	14.70	0.34	0.49	20.60	-	98.64
		Anand *et al.*, 2005	11.43	2.09	48.80	0.12	-	14.36	0.34	0.52	21.71	-	99.37
		Udry and Day, 2018 (A)	11.60	1.73	50.00	0.11	-	15.00	0.32	0.51	20.10	-	99.37
		Udry and Day, 2018 (B)	11.30	2.02	50.20	0.10	-	15.00	0.35	0.50	19.80	-	99.27
NWA 817	Vein	Gillet *et al.*, 2002	5.69	0.21	42.82	-	-	0.25	0.06	0.55	36.45	-	86.03
		Sautter *et al.*, 2002 (A)	5.96	0.80	41.26	0.00	-	0.84	0.01	0.72	38.36	0.04	87.99
		Sautter et al., 2002 (B)	5.99	0.02	43.06	0.00	-	0.10	0.03	0.53	34.19	0.00	83.92
		Hicks *et al.*, 2014	5.20	0.30	43.10	-	0.08	0.10	-	0.50	34.00	-	83.28
	Bulk	Sautter *et al.*, 2002	10.31	3.28	50.80	-	-	13.07	0.61	0.53	19.84	-	98.44
		Udry and Day, 2018	9.17	3.69	51.00	0.35	-	13.10	0.64	0.46	19.90	-	98.31

MIL 03346	Vein	Day *et al*., 2006 (A)	3.21	0.21	44.90	-	-	0.08	0.05	0.66	37.60	-	86.71
		Day *et al*., 2006 (B)	3.09	0.14	44.90	-	-	0.06	0.05	0.62	35.10	-	83.96
		Day *et al*., 2006 (C)	3.20	0.11	44.60	-	-	0.09	0.06	0.70	38.10	-	86.86
		Day *et al*., 2006 (D)	2.91	0.41	45.50	-	-	0.06	0.04	0.62	35.80	-	85.34
		Sautter *et al*., 2006	2.66	0.26	40.56	0.20	0.92	0.02	0.07	0.59	37.29	-	82.57
		Imae and Ikeda, 2007 (A)	5.75	0.09	32.36	0.00	-	0.13	0.05	1.27	55.53	-	95.18
		Imae and Ikeda, 2007 (B)	3.57	2.26	46.78	0.01	-	0.21	0.03	0.52	30.57	-	83.95
		Hallis *et al*., 2012	3.19	0.13	42.70	0.04	0.52	0.18	-	-	36.98	-	83.74
		Stopar *et al*., 2013	3.10	0.10	42.40	-	0.80	0.14	-	0.63	37.80	-	84.97
		Hicks *et al*., 2014	3.10	0.70	45.00	-	0.40	0.20	0.10	0.50	33.46	-	83.46
		Daly *et al*., 2019b	3.26	1.35	45.53	-	0.46	0.12	0.07	0.54	32.63	-	83.96
	Bulk	Anand *et al*., 2005	9.33	3.59	49.20	0.22	-	15.00	0.07	0.45	19.23	-	97.09
		Day *et al*., 2006	9.26	4.09	49.50	0.23	0.05	14.40	0.68	0.46	19.10	-	97.77
		Udry and Day, 2018	9.26	3.52	51.50	0.19	-	14.90	0.62	0.44	18.20	-	98.63
Y-000749	Vein	Noguchi *et al*., 2009	3.55	0.41	50.12	0.14	1.40	0.14	-	0.24	27.85	-	83.85
		Hicks *et al*., 2014	4.80	0.80	39.50	0.30	2.72	0.20	-	0.50	33.19	-	82.01
		New data set (average of 21)	5.36	1.87	34.19	0.97	0.32	1.16	0.04	0.97	38.38	0.02	83.28
	Bulk	Imae *et al*., 2003	11.08	2.01	48.77	0.13	-	15.08	0.46	0.58	21.16	-	99.27
		Udry and Day, 2018	10.51	2.12	51.00	0.13	-	13.60	0.37	0.50	21.00	-	99.23
Y-000802	Vein	New data set (average of 25)	3.54	0.99	39.33	0.43	2.13	0.56	0.03	1.59	34.78	0.01	83.38
	Bulk	James Day*	11.09	1.88	46.92	0.12	-	13.82	0.36	0.52	22.01	-	96.72
NWA 998	Vein	Treiman and Irving, 2008 (A)	4.46	2.10	35.42	-	-	2.97	0.15	1.00	39.07	-	85.17
		Treiman and Irving, 2008 (B)	4.16	0.39	37.86	-	-	3.06	0.00	0.71	40.69	-	86.87
		Treiman and Irving, 2008 (C)	3.81	0.56	39.04	-	-	3.09	0.02	0.72	39.21	-	86.45
		New data set (average of 3)	7.99	0.93	37.81	0.21	0.02	1.56	0.08	0.79	36.13	0.02	85.53
	Bulk	Treiman and Irving, 2008 (A)	11.70	2.00	47.40	-	-	13.8	0.50	0.50	20.11	-	96.01
		Treiman and Irving, 2008 (B)	11.70	2.80	49.10	0.10	-	14.00	0.50	0.50	19.22	-	97.92
		Udry and Day, 2018 (A)	12.30	1.42	50.70	0.01	-	14.20	0.33	0.50	20.10	-	99.56
		Udry and Day, 2018 (B)	9.80	2.50	56.80	0.21	-	11.40	0.52	0.40	17.30	-	98.93
NWA 11013	Bulk	Udry and Day, 2018	7.61	4.68	53.70	0.31	-	13.90	0.71	0.38	16.70	-	97.99
MIL 090030	Vein	Hallis and Taylor, 2011 (A)	6.25	0.36	42.96	-	0.42	0.15	-	0.57	32.52	-	83.23
		Hallis and Taylor, 2011 (B)	3.19	0.13	42.71	0.04	0.52	0.18	-	-	37.03	-	83.80
		New data set (average of 34)	4.66	0.33	44.06	0.04	0.55	0.16	0.04	0.61	31.38	0.01	81.83
	Bulk	Udry and Day, 2018	10.77	3.69	45.80	0.24	-	13.8	0.67	0.54	23.10	-	98.61
MIL 090032	Vein	Hallis and Taylor, 2011	3.34	0.42	43.16	0.48	-	0.28	0.03	0.65	32.81	-	81.17
		New data set (average of 28)	2.37	0.27	40.99	0.06	0.57	0.22	0.03	0.60	34.99	0.01	80.11
	Bulk	Udry and Day, 2018	9.60	3.33	51.80	0.14	-	14.50	0.61	0.45	18.30	-	98.73

MIL 090136	Vein	Hallis and Taylor, 2011	4.66	0.24	42.66	0.02	0.48	0.08	-	0.78	35.79	-	84.71
		New data set (average of 23)	3.13	0.23	43.42	0.04	0.74	0.19	0.05	0.70	33.86	0.01	82.37
	Bulk	Udry and Day, 2018 (A)	9.23	3.48	52.00	0.19	-	13.60	0.62	0.46	19.10	-	98.68
		Udry and Day, 2018 (B)	9.69	3.63	49.50	0.24	-	14.30	0.66	0.48	20.10	-	98.60

"-" indicates that this value was below detection limits, not tested for, or not stated in the original source material
"(A, B, C, …)" used to differentiate multiple separate value sets taken from the same source material
* This is the unpublished Y-000802 bulk value from analyses performed by James Day

Appendix Table 4 draws on multiple literature sources to compile a collection of bulk rock and olivine-hosted iddingsite oxide composition values for Lafayette (Boctor *et al.*, 1976; Treiman *et al.*, 1993; Lodders, 1998; Kuebler *et al.*, 2004; Changela and Bridges, 2010; Hicks *et al.*, 2014; Udry and Day, 2018), Y-000593 (Shirai *et al.*, 2002; Imae *et al.*, 2003, 2005; Oura *et al.*, 2003; Noguchi *et al.*, 2009; Hicks *et al.*, 2014; Udry and Day, 2018), Nakhla (Prior, 1912; McCarthy *et al.*, 1974; Bunch and Reid, 1975; Dreibus *et al.*, 1982; Lodders, 1998; Anand *et al.*, 2005; Hallis *et al.*, 2012; Hicks *et al.*, 2014; Lee and Chatzitheodoridis, 2016; Udry and Day, 2018), NWA 817 (Sautter *et al.*, 2002; Gillet *et al.*, 2002; Hicks *et al.*, 2014; Udry and Day, 2018), MIL 03346 (Sautter *et al.*, 2002; Anand *et al.*, 2005; Day *et al.*, 2006; Imae and Ikeda, 2007; Hallis *et al.*, 2012; Stopar *et al.*, 2013; Hicks *et al.*, 2014; Udry and Day, 2018; Daly *et al.*, 2019b), Y-000749 (Imae *et al.*, 2003; Noguchi *et al.*, 2009; Hicks *et al.*, 2014; Udry and Day, 2018), Y-000802, NWA 998 (Treiman and Irving, 2008; Udry and Day, 2018), NWA 11013 (Udry and Day, 2018), MIL 090030 (Hallis and Taylor, 2011; Udry and Day, 2018), MIL 090032 (Hallis and Taylor, 2011; Udry and Day, 2018), and MIL 090136 (Hallis and Taylor, 2011; Udry and Day, 2018). Appendix Table 5 is the final oxide values, and Appendix Table 6 is their associated standard deviations.

Appendix Table 5 – Final updated average olivine-hosted iddingsite and bulk rock composition values used in the nakhlite composition graphs

	Updated Average Olivine-hosted Iddingsite and Bulk Rock Oxide composition (wt%)																					
	MgO		Al_2O_3		SiO_2		P_2O_5		SO_2		CaO		TiO_2		MnO		FeO		NiO		Total	
Meteorite	Vein (wt%)	Bulk (wt%)	Vein (wt%)	Bulk (wt%)	Vein (wt%)	Bulk (wt%)	Vein (wt%)	Bulk (wt%)	Vein (wt%)	Bulk (wt%)	Vein (wt%)	Bulk (wt%)	Vein (wt%)	Bulk (wt%)	Vein (wt%)	Bulk (wt%)	Vein (wt%)	Bulk (wt%)	Vein (wt%)	Bulk (wt%)	Vein (wt%)	Bulk (wt%)
Lafayette	11.10	12.60	3.84	1.95	43.38	47.90	0.09	0.29	0.25	0.08	1.01	13.43	0.05	0.35	0.62	0.61	28.13	21.90	0.10	-	88.35	98.95
Y-000593	3.90	10.49	0.74	1.98	41.29	48.78	0.07	0.14	1.20	-	0.25	14.52	0.03	0.39	0.97	0.53	36.46	20.72	0.02	-	84.65	97.51
Nakhla	6.85	12.13	1.11	1.63	38.20	48.94	0.05	0.11	0.08	-	0.48	14.93	0.04	0.33	0.56	0.51	32.87	20.42	0.02	-	80.02	98.85
NWA 817	5.71	9.74	0.33	3.49	42.56	50.90	0.00	0.35	0.08	-	0.32	13.09	0.03	0.63	0.58	0.50	35.75	19.87	0.02	-	85.31	98.38
MIL 03346	3.37	9.28	0.52	3.73	43.20	50.07	0.06	0.21	0.62	0.05	0.12	14.77	0.06	0.46	0.67	0.45	37.35	18.84	-	-	85.52	97.83
Y-000749	4.57	10.80	1.03	2.07	41.27	49.89	0.47	0.13	1.48	-	0.50	14.34	0.04	0.42	0.57	0.54	33.14	21.08	0.02	-	83.05	99.25
Y-000802	3.54	11.09	0.99	1.88	39.33	46.92	0.43	0.12	2.13	-	0.56	13.82	0.03	0.36	1.59	0.52	34.78	22.01	0.01	-	83.38	96.72
NWA 998	5.10	11.38	0.99	2.18	37.53	51.00	0.21	0.11	0.02	-	2.67	13.35	0.06	0.46	0.80	0.48	38.78	19.18	0.02	-	86.01	98.11
NWA 11013	-	7.61	-	4.68	-	53.70	-	0.31	-	-	-	13.90	-	0.71	-	0.38	-	16.70	-	-	89.78	97.99
MIL 090030	4.70	10.77	0.27	3.69	43.24	45.80	0.04	0.24	0.50	-	0.16	13.80	0.04	0.67	0.59	0.54	33.64	23.10	0.01	-	82.95	98.61
MIL 090032	2.86	9.60	0.34	3.33	42.07	51.80	0.27	0.14	0.57	-	0.25	14.50	0.03	0.61	0.63	0.45	33.90	18.30	0.01	-	80.64	98.73
MIL 090136	3.89	9.46	0.24	3.56	43.04	50.75	0.03	0.22	0.61	-	0.13	13.95	0.05	0.64	0.74	0.47	34.83	19.60	0.01	-	83.54	98.64

"-" indicates that there was no data located or produced for this value, thus an average could not be calculated

Note that the "Total" column is not a summation of the averaged oxide values, but an average of the individual total weight percentages for each quantity

Appendix Table 6 – Standard deviation of the respective average iddingsite or bulk oxide composition values reported in Appendix Table 5

	Standard Deviation of: Iddingsite vs Bulk Composition (wt%) - Updated Literature Veins (only olivine) + Literature Bulk Averages																					
	MgO		Al_2O_3		SiO_2		P_2O_5		SO_2		CaO		TiO_2		MnO		FeO		NiO		Total	
Meteorite	Vein (wt%)	Bulk (wt%)	Vein (wt%)	Bulk (wt%)	Vein (wt%)	Bulk (wt%)	Vein (wt%)	Bulk (wt%)	Vein (wt%)	Bulk (wt%)	Vein (wt%)	Bulk (wt%)	Vein (wt%)	Bulk (wt%)	Vein (wt%)	Bulk (wt%)	Vein (wt%)	Bulk (wt%)	Vein (wt%)	Bulk (wt%)	Vein (wt%)	Bulk (wt%)
Lafayette	2.05 (4)	0.52 (3)	0.96 (4)	0.47 (3)	3.85 (4)	1.73 (3)	-	0.23 (2)	0.26 (3)	-	0.26 (4)	0.06 (3)	0.04 (4)	0.07 (3)	0.20 (4)	0.16 (3)	0.82 (4)	0.70 (3)	-	-	6.99 (4)	0.53 (3)
Y-000593	0.86 (5)	0.41 (4)	0.44 (5)	0.11 (4)	11.21 (5)	2.16 (4)	0.05 (4)	0.15 (3)	0.87 (4)	-	0.18 (5)	0.27 (4)	0.01 (3)	0.07 (4)	0.62 (5)	0.05 (4)	12.88 (5)	1.58 (4)	0.01 (2)	-	2.87 (5)	2.10 (4)
Nakhla	1.15 (4)	0.94 (10)	1.50 (4)	0.38 (10)	4.44 (4)	0.94 (10)	-	0.01 (6)	0.02 (3)	-	0.25 (4)	0.36 (10)	0.02 (2)	0.03 (8)	0.14 (3)	0.19 (9)	3.88 (4)	0.97 (10)	-	-	2.05 (4)	1.09 (10)
NWA 817	0.37 (4)	0.81 (2)	0.33 (4)	0.29 (2)	0.88 (4)	0.14 (2)	0.00 (2)	-	-	-	0.35 (4)	0.02 (2)	0.03 (3)	0.02 (2)	0.10 (4)	0.05 (2)	2.07 (4)	0.04 (2)	0.03 (2)	-	2.14 (4)	0.09 (2)
MIL 03346	0.82 (11)	0.04 (3)	0.69 (11)	0.31 (3)	4.00 (11)	1.25 (3)	0.09 (4)	0.02 (3)	0.23 (5)	-	0.06 (11)	0.32 (3)	0.02 (9)	0.34 (3)	0.22 (10)	0.01 (3)	6.50 (11)	0.56 (3)	-	-	3.47 (11)	0.77 (3)
Y-000749	0.93 (3)	0.40 (2)	0.76 (3)	0.08 (2)	8.11 (3)	1.58 (2)	0.44 (3)	0.00 (2)	1.20 (3)	-	0.57 (3)	1.05 (2)	-	0.06 (2)	0.37 (3)	0.06 (2)	5.26 (3)	0.11 (2)	-	-	0.94 (3)	0.03 (2)
Y-000802	-	-	-	-	-	-	-	-	-	-	-	-	-	-	-	-	-	-	-	-	-	-
NWA 998	1.94 (4)	1.09 (4)	0.77 (4)	0.60 (4)	1.52 (4)	4.09 (4)	-	0.10 (3)	-	-	0.74 (4)	1.31 (4)	0.07 (4)	0.09 (4)	0.13 (4)	0.05 (4)	1.91 (4)	1.32 (4)	-	-	0.79 (4)	1.55 (4)
NWA 11013	-	-	-	-		-	-	-	-	-	-	-	-	-	-	-	-	-	-	-	-	-
MIL 090030	1.53 (3)	-	0.13 (3)	-	0.72 (3)	-	0.00 (2)	-	0.07 (3)	-	0.02 (3)	-	-	-	0.03 (2)	-	2.99 (3)	-	-	-	1.01 (3)	-
MIL 090032	0.68 (2)	-	0.11 (2)	-	1.54 (2)	-	0.30 (2)	-	-	-	0.04 (2)	-	0.00 (2)	-	0.03 (2)	-	1.54 (2)	-	-	-	0.75 (2)	-
MIL 090136	1.08 (2)	0.33 (2)	0.00 (2)	0.11 (2)	0.54 (2)	1.77 (2)	0.02 (2)	0.04 (2)	0.18 (2)	-	0.08 (2)	0.49 (2)	-	0.03 (2)	0.06 (2)	0.01 (2)	1.36 (2)	0.71 (2)	-	-	1.66 (2)	0.06 (2)

"-" indicates where standard deviation was not applicable since the respective value is an "average" of either one or zero values

"(n)" represents the number of values that form the respective average value

Note that the "Total" column does not represent a summation of the oxide standard deviation values, but instead reflects the standard deviation of the average total weight percentage for each quantity

Appendix 2 – Nakhlite APT Supplementary Information

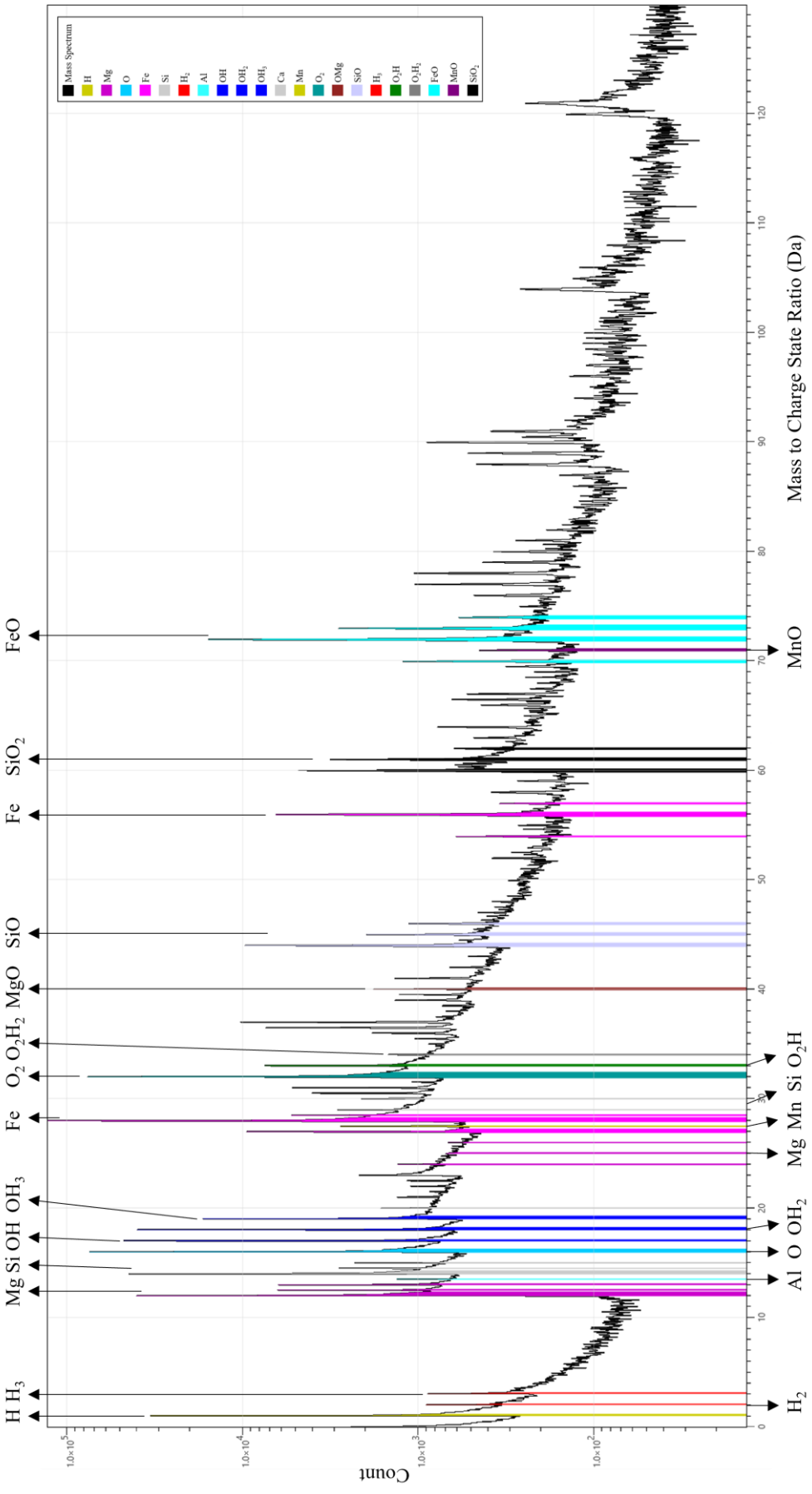

Appendix Figure 1 – Assigned and annotated mass spectrum of Nakhlite1. Spectrum involves the same colour scheme as the Nakhlite1 reconstruction in Figure 10.

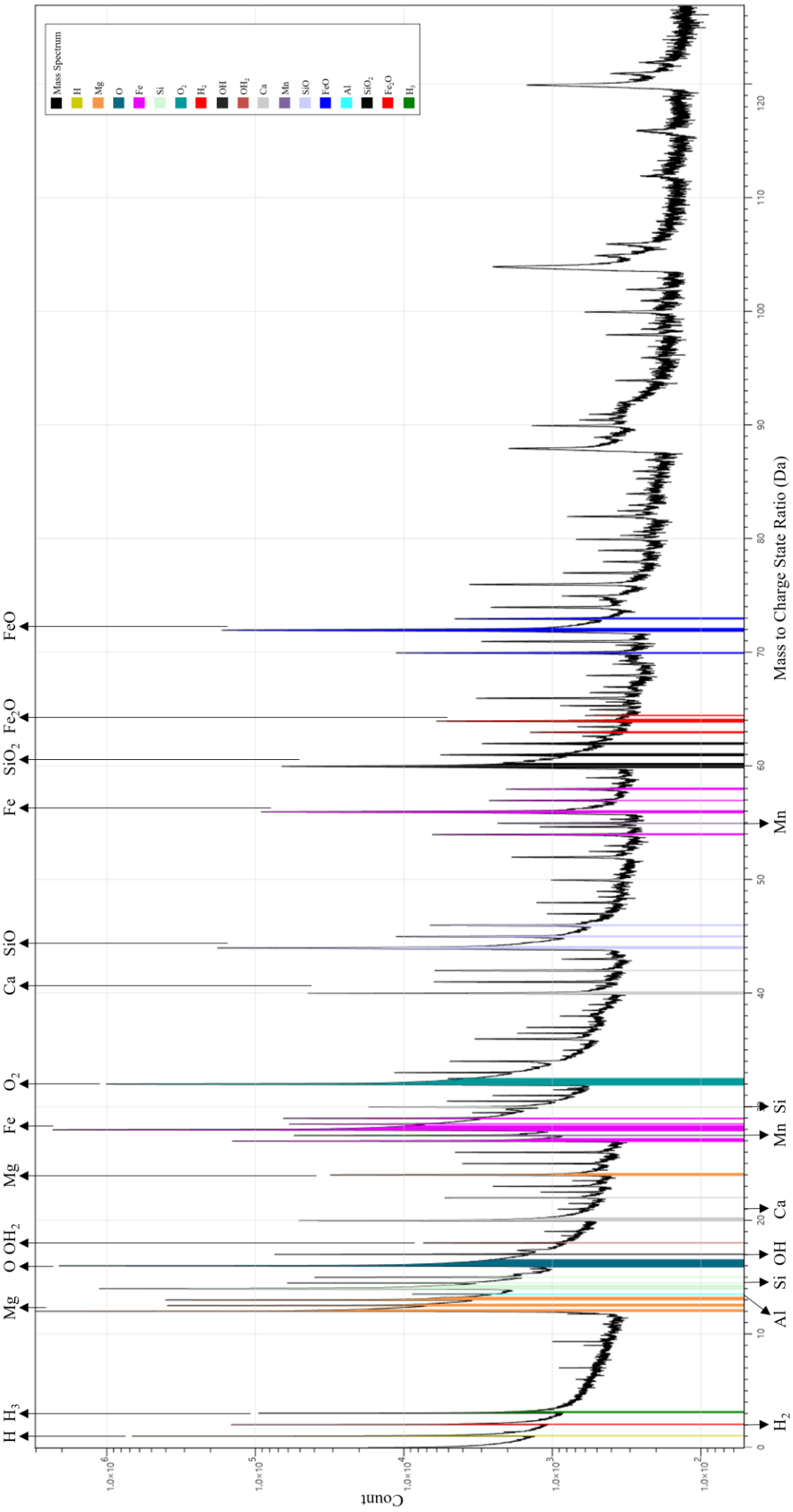

Appendix Figure 2 – Assigned and annotated mass spectrum of Nakhlite2. Figure utilises the same colours as used to produce the Nakhlite2 reconstruction in Figure 11.

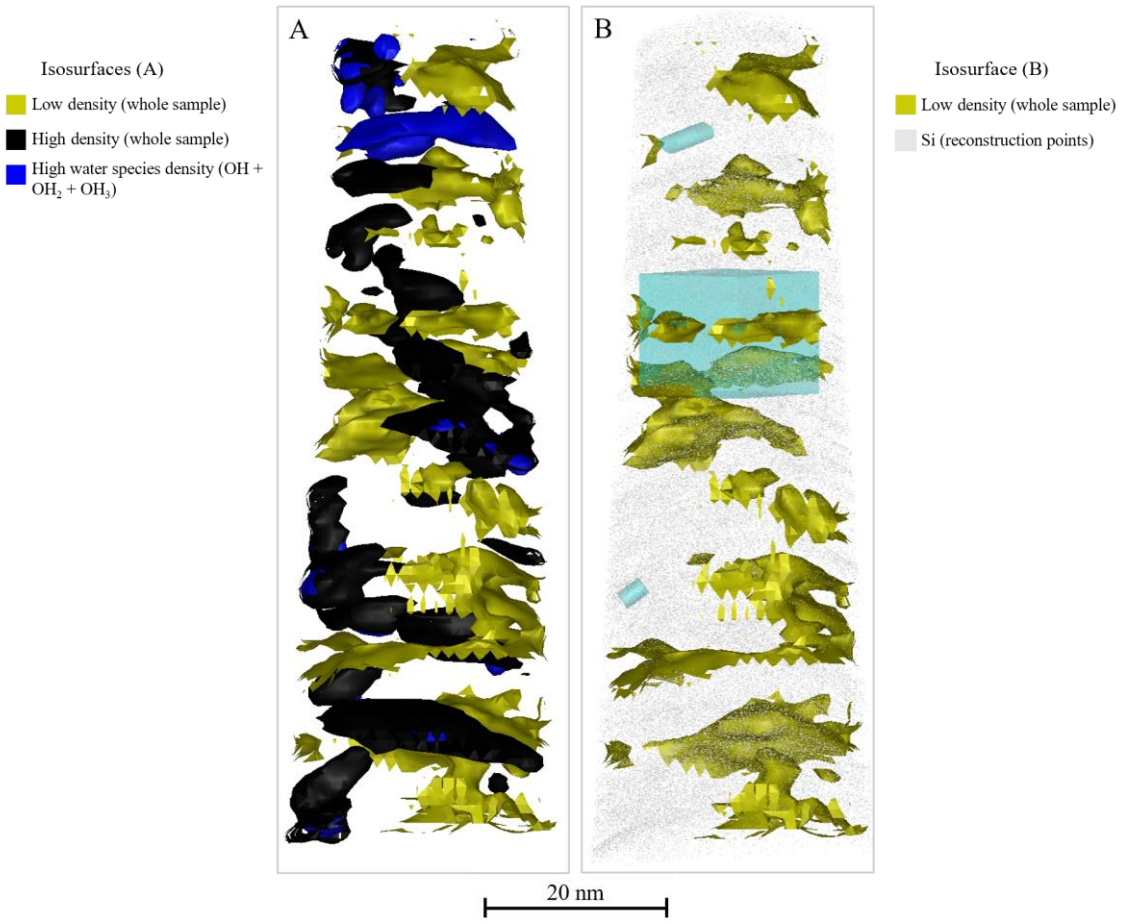

Appendix Figure 3 – A) represents an isosurface diagram of Nakhlite1 (the same as in Figure 10) included in this figure to serve as a frame of reference for B) – an isosurface diagram displaying areas of low sample density plus Si reconstruction points. Also included in B), near the top of the diagram, is a small cylinder corresponding to the "True water cylinder" in Table 3 which, upon comparison to A), clearly overlaps with the area of high water species density that is not simply an area of overall high density in the sample. The large cube in the centre depicts where the "Representative cube" was taken from (in an area specifically chosen to avoid areas of high water species density) and the small cylinder in the lower left relates to the "Pseudo water cylinder" volume (intentionally taken from area of high water species density that corresponds with an area of overall high density in the sample).

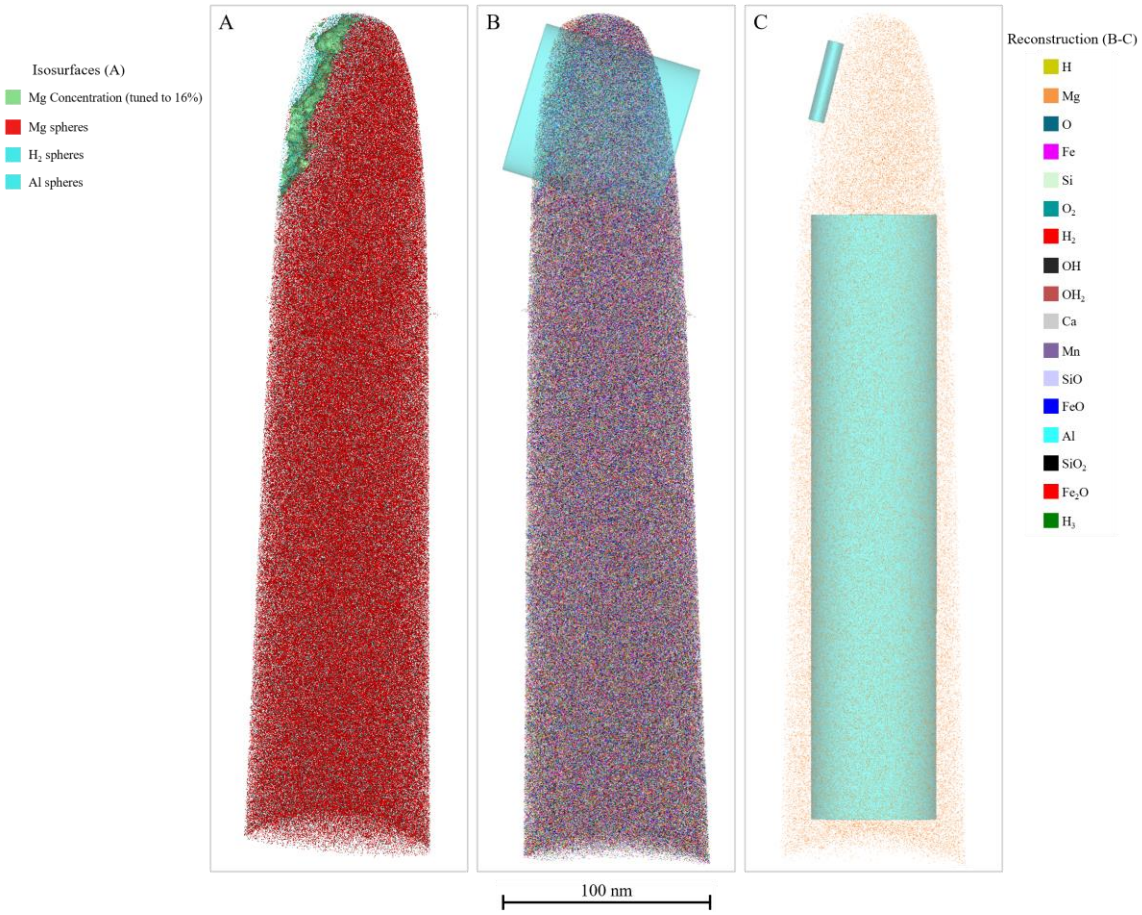

Appendix Figure 4 – A) is a combination of a reconstruction of Nakhlite2 along with a magnesium concentration isosurface tuned to accentuate the olivine-iddingsite interface present within the sample. B) represents the full reconstruction of Nakhlite2 with an annotated cylindrical volume from which the 1-dimensional concentration profile intersecting the olivine-iddingsite interface was produced (along the centre of the cylinder). C) is another reconstruction of Nakhlite2 (only displaying Mg points for clarity) that indicates the location of the "Olivine cylinder" volume (large cylinder in the bottom portion overlapping with the large olivine section of the sample) and the "Iddingsite cylinder" (smaller cylinder in the top left corresponding to the small iddingsite part of Nakhlite2) which are discussed in Table 3.

References

Abramov O. and Kring D. A. (2005) Impact-induced hydrothermal activity on early Mars. *J. Geophys. Res.* **110**, E12S09.

Acuña M. H., Connerney J. E. P., Wasilewski P., Lin R. P., Anderson K. A., Carlson C. W., McFadden J., Curtis D. W., Mitchell D., Reme H., Mazelle C., Sauvaud J. A., d'Uston C., Cros A., Medale J. L., Bauer S. J., Cloutier P., Mayhew M., Winterhalter D. and Ness N. F. (1998) Magnetic Field and Plasma Observations at Mars: Initial Results of the Mars Global Surveyor Mission. *Science*.

Acuña M. H., Connerney J. E. P., Wasilewski P., Lin R. P., Mitchell D., Anderson K. A., Carlson C. W., McFadden J., Rème H., Mazelle C., Vignes D., Bauer S. J., Cloutier P. and Ness N. F. (2001) Magnetic field of Mars: Summary of results from the aerobraking and mapping orbits. *J. Geophys. Res.* **106**, 23403–23417.

Aerts J. W., Riedo A., Melton D. J., Martini S., Flahaut J., Meierhenrich U. J., Meinert C., Myrgorodska I., Lindner R. and Ehrenfreund P. (2020) Biosignature Analysis of Mars Soil Analogs from the Atacama Desert: Challenges and Implications for Future Missions to Mars. *Astrobiology* **20**, 766–784.

Agee C. B., Wilson N. V., McCubbin F. M., Ziegler K., Polyak V. J., Sharp Z. D., Asmerom Y., Nunn M. H., Shaheen R., Thiemens M. H., Steele A., Fogel M. L., Bowden R., Glamoclija M., Zhang Z. and Elardo S. M. (2013) Unique Meteorite from Early Amazonian Mars: Water-Rich Basaltic Breccia Northwest Africa 7034. *Science* **339**, 780–785.

Ahn C. C. ed. (2004) *Transmission Electron Energy Loss Spectrometry in Materials Science and The EELS Atlas*. 1st ed., Wiley.

Alexander C. M. O., Bowden R., Fogel M. L., Howard K. T., Herd C. D. K. and Nittler L. R. (2012) The Provenances of Asteroids, and Their Contributions to the Volatile Inventories of the Terrestrial Planets. *Science* **337**, 721–723.

Allwood A. C., Rosing M. T., Flannery D. T., Hurowitz J. A. and Heirwegh C. M. (2018) Reassessing evidence of life in 3,700-million-year-old rocks of Greenland. *Nature* **563**, 241–244.

Anand M., Williams C. T., Russell S. S., Jones G., James S. and Grady M. M. (2005) Petrology and geochemistry of nakhlite MIL 03346: A new Martian meteorite from Antarctica. In 36th Lunar and Planetary Science Conference. Houston, Texas, USA.

Antao S. M., Hassan I., Wang J., Lee P. L. and Toby B. H. (2008) STATE-OF-THE-ART HIGH-RESOLUTION POWDER X-RAY DIFFRACTION (HRPXRD) ILLUSTRATED WITH RIETVELD STRUCTURE REFINEMENT OF QUARTZ, SODALITE, TREMOLITE, AND MEIONITE. *The Canadian Mineralogist* **46**, 1501–1509.

Antunes A., Olsson-Francis K. and McGenity T. J. (2020) Exploring Deep-Sea Brines as Potential Terrestrial Analogues of Oceans in the Icy Moons of the Outer Solar System. *Curr Issues Mol Biol* **38**, 123–162.

Bains W., Petkowski J. J., Seager S., Ranjan S., Sousa-Silva C., Rimmer P. B., Zhan Z., Greaves J. S. and Richards A. M. S. (2021) Phosphine on Venus Cannot Be Explained by Conventional Processes. *Astrobiology* **21**, 1277–1304.

Baker V. R. (2014) Terrestrial analogs, planetary geology, and the nature of geological reasoning. *Planetary and Space Science* **95**, 5–10.

Banfield J. F., Moreau J. W., Chan C. S., Welch S. A. and Little B. (2001) Mineralogical Biosignatures and the Search for Life on Mars. *Astrobiology* **1**, 447–465.

Beaty D. W., Grady M. M., McSween H. Y., Sefton-Nash E., Carrier B. L., Altieri F., Amelin Y., Ammannito E., Anand M., Benning L. G., Bishop J. L., Borg L. E., Boucher D., Brucato J. R., Busemann H., Campbell K. A., Czaja A. D., Debaille V., Des Marais D. J., Dixon M., Ehlmann B. L., Farmer J. D., Fernandez-Remolar D. C., Filiberto J., Fogarty J., Glavin D. P., Goreva Y. S., Hallis L. J., Harrington A. D., Hausrath E. M., Herd C. D. K., Horgan B., Humayun M., Kleine T., Kleinhenz J., Mackelprang R., Mangold N., Mayhew L. E., McCoy J. T., McCubbin F. M., McLennan S. M., Moser D. E., Moynier F., Mustard J. F., Niles P. B., Ori G. G., Raulin F., Rettberg P., Rucker M. A., Schmitz N., Schwenzer S. P., Sephton M. A., Shaheen R., Sharp Z. D., Shuster D. L., Siljeström S., Smith C. L., Spry J. A., Steele A., Swindle T. D., ten Kate I. L., Tosca N. J., Usui T., Van Kranendonk M. J., Wadhwa M., Weiss B. P., Werner S. C., Westall F., Wheeler R. M., Zipfel J. and Zorzano M. P. (2019) The potential science and engineering value of samples delivered to Earth by Mars sample return. *Meteoritics & Planetary Science* **54**, S3–S152.

Bishop J. L., Murad E., Lane M. D. and Mancinelli R. L. (2004) Multiple techniques for mineral identification on Mars:: a study of hydrothermal rocks as potential analogues for astrobiology sites on Mars. *Icarus* **169**, 311–323.

Bishop J. L., Loizeau D., McKeown N. K., Saper L., Dyar M. D., Des Marais D. J., Parente M. and Murchie S. L. (2013) What the ancient phyllosilicates at Mawrth Vallis can tell us about possible habitability on early Mars. *Planetary and Space Science* **86**, 130–149.

Blum T. B., Darling J. R., Kelly T. F., Larson D. J., Moser D. E., Perez-Huerta A., Prosa T. J., Reddy S. M., Reinhard D. A., Saxey D. W., Ulfig R. M. and Valley J. W. (2017) Best Practices for Reporting Atom Probe Analysis of Geological Materials. In *Geophysical Monograph Series* (eds. D. E. Moser, F. Corfu, J. R. Darling, S. M. Reddy, and K. Tait). John Wiley & Sons, Inc., Hoboken, NJ, USA. pp. 369–373.

Boctor N. Z., Meyer H. O. A. and Kullerud G. (1976) Lafayette meteorite: petrology and opaque mineralogy. *Earth and Planetary Science Letters* **32**, 69–76.

Bogard D. D. and Johnson P. (1983) Martian Gases in an Antarctic Meteorite? *Science* **221**, 651–654.

Boggs S. (2011) *Principles of sedimentology and stratigraphy*. 5th ed., Pearson, Boston.

Borg L. and Drake M. J. (2005) A review of meteorite evidence for the timing of magmatism and of surface or near-surface liquid water on Mars. *Journal of Geophysical Research: Planets* **110**.

Bosak T., Moore K. R., Gong J. and Grotzinger J. P. (2021) Searching for biosignatures in sedimentary rocks from early Earth and Mars. *Nat Rev Earth Environ* **2**, 490–506.

Bouvier A., Blichert-Toft J., Vervoort J. D. and Albarède F. (2005) The age of SNC meteorites and the antiquity of the Martian surface. *Earth and Planetary Science Letters* **240**, 221–233.

Bouvier A., Blichert-Toft J. and Albarède F. (2009) Martian meteorite chronology and the evolution of the interior of Mars. *Earth and Planetary Science Letters* **280**, 285–295.

Brack A., Horneck G., Cockell C. s., Bérces A., Belisheva N. k., Eiroa C., Henning T., Herbst T., Kaltenegger L., Léger A., Liseau R., Lammer H., Selsis F., Beichman C., Danchi W., Fridlund M., Lunine J., Paresce F., Penny A., Quirrenbach A., Röttgering H., Schneider J., Stam D., Tinetti G. and White G. J. (2010) Origin and Evolution of Life on Terrestrial Planets. *Astrobiology* **10**, 69–76.

Bradley J. P., Harvey R. P., McSween H. Y., Gibson E., Thomas-Keprta K. and Vali H. (1997) No 'nanofossils' in martian meteorite. *Nature* **390**, 454–455.

Brass G. W. (1980) Stability of brines on Mars. *Icarus* **42**, 20–28.

Brennecka G. A., Borg L. E. and Wadhwa M. (2014) Insights into the Martian mantle: The age and isotopics of the meteorite fall Tissint. *Meteorit Planet Sci* **49**, 412–418.

Bridges J. C. and Schwenzer S. P. (2012) The nakhlite hydrothermal brine on Mars. *Earth and Planetary Science Letters* **359–360**, 117–123.

Bunch T. E. and Reid A. M. (1975) THE NAKHLITES PART I: PETROGRAPHY AND MINERAL CHEMISTRY. *Meteoritics* **10**, 303–315.

Cady S. L., Farmer J. D., Grotzinger J. P., Schopf J. W. and Steele A. (2003) Morphological Biosignatures and the Search for Life on Mars. *Astrobiology* **3**, 351–368.

Cady S. L., Skok J. R., Gulick V. G., Berger J. A. and Hinman N. W. (2018) Siliceous Hot Spring Deposits: Why They Remain Key Astrobiological Targets. In *From Habitability to Life on Mars* Elsevier. pp. 179–210.

cameca.com (2022a) Cameca - Introduction to APT.https://www.cameca.com/products/apt/technique (2022) Accessed January 24, 2022

cameca.com (2022b) CAMECA LEAP 5000 Atom Probe.https://www.cameca.com/products/apt/leap-5000 (2022) Accessed July 7, 2022

Carr M. H., Baum W. A., Briggs G. A., Masursky H., Wise D. W. and Montgomery D. R. (1972) Imaging experiment: The Viking Mars orbiter. *Icarus* **16**, 17–33.

Carr M. H. (1996) Channels and valleys on Mars: cold climate features formed as a result of a thickening cryosphere. *Planetary and Space Science* **44**, 1411–1423.

Carr M. H. and Head J. W. (2010) Geologic history of Mars. *Earth and Planetary Science Letters* **294**, 185–203.

Carr M. H. and Head J. W. (2019) Mars: Formation and fate of a frozen Hesperian ocean. *Icarus* **319**, 433–443.

Carter J., Poulet F., Bibring J.-P., Mangold N. and Murchie S. (2013) Hydrous minerals on Mars as seen by the CRISM and OMEGA imaging spectrometers: Updated global view: HYDROUS MINERALS ON MARS: GLOBAL VIEW. *J. Geophys. Res. Planets* **118**, 831–858.

Centro de Astrobiología (2017) Weather report Mars Year 33, month 11.http://cab.inta-csic.es/rems/en/weather-report-mars-year-33-month-11/, http://cab.inta-csic.es/rems/en/weather-report-mars-year-33-month-11/ (2017) Accessed March 18, 2022

Changela H. G. and Bridges J. C. (2010) Alteration assemblages in the nakhlites: Variation with depth on Mars: Alteration assemblages in the nakhlites. *Meteoritics & Planetary Science* **45**, 1847–1867.

Channing A. and Edwards D. (2009) SILICIFICATION OF HIGHER PLANTS IN GEOTHERMALLY INFLUENCED WETLANDS: YELLOWSTONE AS A LOWER DEVONIAN RHYNIE ANALOG. *PALAIOS* **24**, 505–521.

Chassefière E., Leblanc F. and Langlais B. (2007) The combined effects of escape and magnetic field histories at Mars. *Planetary and Space Science* **55**, 343–357.

Christiansen R. L. (2001) *The Quaternary and Pliocene Yellowstone Plateau Volcanic Field of Wyoming, Idaho, and Montana*., U.S. Department of the Interior, U.S. Geological Survey.

Citron R. I., Manga M. and Hemingway D. J. (2018) Timing of oceans on Mars from shoreline deformation. *Nature* **555**, 643–646.

Clayton R. N. (1993) Antarctic Meteorite Newsletter 16(3).

Clayton R. N. and Mayeda T. K. (1996) Oxygen isotope studies of achondrites. *Geochimica et Cosmochimica Acta* **60**, 1999–2017.

Clemett S. J., Dulay M. T., Gillette J. S., Chillier X. D. F., Mahajan T. B. and Zare R. N. (1998) Evidence for the extraterrestrial origin of polycyclic aromatic hydrocarbons in the Martian meteorite ALH84001. *Faraday Discuss.* **109**, 417–436.

Cockell C. S., Balme M., Bridges J. C., Davila A. and Schwenzer S. P. (2012) Uninhabited habitats on Mars. *Icarus* **217**, 184–193.

Cockell C. s., Bush T., Bryce C., Direito S., Fox-Powell M., Harrison J. p., Lammer H., Landenmark H., Martin-Torres J., Nicholson N., Noack L., O'Malley-James J., Payler S. j., Rushby A., Samuels T., Schwendner P., Wadsworth J. and Zorzano M. p. (2016) Habitability: A Review. *Astrobiology* **16**, 89–117.

Cohen B. E., Mark D. F., Cassata W. S., Lee M. R., Tomkinson T. and Smith C. L. (2017) Taking the pulse of Mars via dating of a plume-fed volcano. *Nat Commun* **8**, 640.

Colthup N. B., Daly L. H. and Wiberly S. E. (1975) *Introduction to Infrared and Raman Spectroscopy*., Elsevier.

Corrigan C. M., Velbel M. A. and Vicenzi E. P. (2015) Modal abundances of pyroxene, olivine, and mesostasis in nakhlites: Heterogeneity, variation, and implications for nakhlite emplacement. *Meteorit Planet Sci* **50**, 1497–1511.

Costard F., Séjourné A., Lagain A., Ormö J., Rodriguez J. A. P., Clifford S., Bouley S., Kelfoun K. and Lavigne F. (2019) The Lomonosov Crater Impact Event: A Possible Mega-Tsunami Source on Mars. *J. Geophys. Res. Planets* **124**, 1840–1851.

Craddock R. A. and Howard A. D. (2002) The case for rainfall on a warm, wet early Mars: RAINFALL ON MARS. *J.-Geophys.-Res.* **107**, 21-1-21–36.

Daly L., Lee M. R., Bagot P. A. J., Hallis L. J., Halpin J., Smith W. and McFadzean S. (2019a) Insights into Martian fluid-rock reactions by atom probe tomography of the interface between nakhlite olivine and iddingsite. In 50th Lunar and Planetary Science Conference 2019.

Daly L., Lee M. R., Piazolo S., Griffin S., Bazargan M., Campanale F., Chung P., Cohen B. E., Pickersgill A. E., Hallis L. J., Trimby P. W., Baumgartner R., Forman L. V. and Benedix G. K. (2019b) Boom boom pow: Shock-facilitated aqueous alteration and evidence for two shock events in the Martian nakhlite meteorites. *Sci. Adv.* **5**, eaaw5549.

Daly L., Lee M. R., Bagot P., Halpin J., Smith W., Mcfadzean S., O'Brien A. C., Griffin S., Hallis L. J. and Cohen B. E. (2020) Exploring Mars at the nanoscale: Applications of transmission electron microscopy and atom probe tomography in planetary exploration. *IOP Conf. Ser.: Mater. Sci. Eng.* **891**, 012008.

Daly L., Lee M. R., Darling J. R., McCarrol I., Yang L., Cairney J., Forman L. V., Bland P. A., Benedix G. K., Fougerouse D., Rickard W. D. A., Saxey D. W., Reddy S. M., Smith W. and Bagot P. A. J. (2021) Developing Atom Probe Tomography of Phyllosilicates in Preparation for Extra-Terrestrial Sample Return. *Geostandards and Geoanalytical Research* **45**, 427–441.

Dartnell L. (2011) Biological constraints on habitability. *Astronomy & Geophysics* **52**, 1.25-1.28.

Davila A. F., Duport L. G., Melchiorri R., Jänchen J., Valea S., de los Rios A., Fairén A. G., Möhlmann D., McKay C. P., Ascaso C. and Wierzchos J. (2010a) Hygroscopic Salts and the Potential for Life on Mars. *Astrobiology* **10**, 617–628.

Davila A. F., Skidmore M., Fairén A. G., Cockell C. and Schulze-Makuch D. (2010b) New Priorities in the Robotic Exploration of Mars: The Case for In Situ Search for Extant Life. *Astrobiology* **10**, 705–710.

Day J. M. D., Taylor L. A., Floss C. and Mcsween H. Y. (2006) Petrology and chemistry of MIL 03346 and its significance in understanding the petrogenesis of nakhlites on Mars. *Meteoritics & Planetary Science* **41**, 581–606.

Day J. M. D., Tait K. T., Udry A., Moynier F., Liu Y. and Neal C. R. (2018) Martian magmatism from plume metasomatized mantle. *Nat Commun* **9**, 4799.

D'Elia M., Blanco A., Galiano A., Orofino V., Fonti S., Mancarella F., Guido A., Russo F. and Mastandrea A. (2017) SEM morphological studies of carbonates and the search for ancient life on Mars. *International Journal of Astrobiology* **16**, 137–142.

Des Marais D. J., Nuth J. A., Allamandola L. J., Boss A. P., Farmer J. D., Hoehler T. M., Jakosky B. M., Meadows V. S., Pohorille A., Runnegar B. and Spormann A. M. (2008) The NASA Astrobiology Roadmap. *Astrobiology* **8**, 715–730.

Devaraj A., Colby R., Hess W. P., Perea D. E. and Thevuthasan S. (2013) Role of Photoexcitation and Field Ionization in the Measurement of Accurate Oxide Stoichiometry by Laser-Assisted Atom Probe Tomography. *J. Phys. Chem. Lett.* **4**, 993–998.

DiAchille G. and Hynek B. M. (2010) 8 - Deltas and valley networks on Mars: Implications for a global hydrosphere. In *Lakes on Mars* (eds. N. A. Cabrol and E. A. Grin). Elsevier, Amsterdam. pp. 223–248.

Dokland T. (2006) *Techniques in Microscopy for Biomedical Applications*., World Scientific.

Dreibus G., Palme H., Rammensee W., Spettel B., Weckwerth G. and Wanke H. (1982) Composition of Shergotty Parent Body: Further Evidence for a Two Component Model of Planet Formation. , 186–187.

Dypvik H., Hellevang H., Krzesińska A., Sætre C., Viennet J.-C., Bultel B., Ray D., Poulet F., Loizeau D., Veneranda M., Rull F., Cousin A. and Werner S. C. (2021) The Planetary Terrestrial Analogues Library (PTAL) – An exclusive lithological selection of possible martian earth analogues. *Planetary and Space Science* **208**, 105339.

Edwards C. S. and Christensen P. R. (2013) Microscopic emission and reflectance thermal infrared spectroscopy: instrumentation for quantitative in situ mineralogy of complex planetary surfaces. *Appl. Opt., AO* **52**, 2200–2217.

Edwards H. G. M., Jorge Villar S. E., Pullan D., Hargreaves M. D., Hofmann B. A. and Westall F. (2007) Morphological biosignatures from relict fossilised sedimentary geological specimens: a Raman spectroscopic study. *Journal of Raman Spectroscopy* **38**, 1352–1361.

Elkins-Tanton L. T. (2008) Linked magma ocean solidification and atmospheric growth for Earth and Mars. *Earth and Planetary Science Letters* **271**, 181–191.

Eugster O., Weigel A. and Polnau E. (1997) Ejection times of Martian meteorites. *Geochimica et Cosmochimica Acta* **61**, 2749–2757.

Fairén A. G., Chevrier V., Abramov O., Marzo G. A., Gavin P., Davila A. F., Tornabene L. L., Bishop J. L., Roush T. L., Gross C., Kneissl T., Uceda E. R., Dohm J. M., Schulze-Makuch D., Rodríguez J. A. P., Amils R. and McKay C. P. (2010a) Noachian and more recent phyllosilicates in impact craters on Mars. *Proc. Natl. Acad. Sci. U.S.A.* **107**, 12095–12100.

Fairén A. G., Davila A. F., Lim D., Bramall N., Bonaccorsi R., Zavaleta J., Uceda E. R., Stoker C., Wierzchos J., Dohm J. M., Amils R., Andersen D. and McKay C. P. (2010b) Astrobiology through the Ages of Mars: The Study of Terrestrial Analogues to Understand the Habitability of Mars. *Astrobiology* **10**, 821–843.

Farber C., Li J., Hager E., Chemelewski R., Mullet J., Rogachev A. Yu. and Kurouski D. (2019) Complementarity of Raman and Infrared Spectroscopy for Structural Characterization of Plant Epicuticular Waxes. *ACS Omega* **4**, 3700–3707.

Farinella P., Gonczi R., Froeschlé Ch. and Froeschlé C. (1993) The Injection of Asteroid Fragments into Resonances. *Icarus* **101**, 174–187.

Farley K. A., Williford K. H., Stack K. M., Bhartia R., Chen A., de la Torre M., Hand K., Goreva Y., Herd C. D. K., Hueso R., Liu Y., Maki J. N., Martinez G., Moeller R. C., Nelessen A., Newman C. E., Nunes D., Ponce A., Spanovich N., Willis P. A., Beegle L. W., Bell J. F., Brown A. J., Hamran S.-E., Hurowitz J. A., Maurice S., Paige D. A., Rodriguez-Manfredi J. A., Schulte M. and Wiens R. C. (2020) Mars 2020 Mission Overview. *Space Sci Rev* **216**, 142.

Farley K. A., Stack K. M., Shuster D. L., Horgan B. H. N., Hurowitz J. A., Tarnas J. D., Simon J. I., Sun V. Z., Scheller E. L., Moore K. R., McLennan S. M., Vasconcelos P. M., Wiens R. C., Treiman A. H., Mayhew L. E., Beyssac O., Kizovski T. V., Tosca N. J., Williford K. H., Crumpler L. S., Beegle L. W., Bell J. F., Ehlmann B. L., Liu Y., Maki J. N., Schmidt M. E., Allwood A. C., Amundsen H. E. F., Bhartia R., Bosak T., Brown A. J., Clark B. C., Cousin A., Forni O., Gabriel T. S. J., Goreva Y., Gupta S., Hamran S.-E., Herd C. D. K., Hickman-Lewis K., Johnson J. R., Kah L. C., Kelemen P. B., Kinch K. B., Mandon L., Mangold N., Quantin-Nataf C., Rice M. S., Russell P. S., Sharma S., Siljeström S., Steele A., Sullivan R., Wadhwa M., Weiss B. P., Williams A. J., Wogsland B. V., Willis P. A., Acosta-Maeda T. A., Beck P., Benzerara K., Bernard S., Burton A. S., Cardarelli E. L., Chide B., Clavé E., Cloutis E. A., Cohen B. A., Czaja A. D., Debaille V., Dehouck E., Fairén A. G., Flannery D. T., Fleron S. Z., Fouchet T., Frydenvang J., Garczynski B. J., Gibbons E. F., Hausrath E. M., Hayes A. G., Henneke J., Jørgensen J. L., Kelly E. M., Lasue J., Le Mouélic S., Madariaga J. M., Maurice S., Merusi M., Meslin P.-Y., Milkovich S. M., Million C. C., Moeller R. C., Núñez J. I., Ollila A. M., Paar G., Paige D. A., Pedersen D. A. K., Pilleri P., Pilorget C., Pinet P. C., Rice J. W., Royer C., Sautter V., Schulte M., Sephton M. A., Sharma S. K., Sholes S. F., Spanovich N., St. Clair M., Tate C. D., Uckert K., VanBommel S. J., Yanchilina A. G. and Zorzano M.-P. (2022) Aqueously altered igneous rocks sampled on the floor of Jezero crater, Mars. *Science*, eabo2196.

Fassett C. I. and Head III J. W. (2005) Fluvial sedimentary deposits on Mars: Ancient deltas in a crater lake in the Nili Fossae region. *Geophysical Research Letters* **32**.

Fassett C. I. and Head I. James W. (2006) Valleys on Hecates Tholus, Mars: origin by basal melting of summit snowpack. *Planetary and Space Science* **54**, 370–378.

Fassett C. I. and Head J. W. (2007) Valley formation on martian volcanoes in the Hesperian: Evidence for melting of summit snowpack, caldera lake formation, drainage and erosion on Ceraunius Tholus. *Icarus* **189**, 118–135.

Fassett C. I., Dickson J. L., Head J. W., Levy J. S. and Marchant D. R. (2010) Supraglacial and proglacial valleys on Amazonian Mars. *Icarus* **208**, 86–100.

Fayers S. R. and Trewin N. H. (2002) A new crustacean from the Early Devonian Rhynie chert, Aberdeenshire, Scotland. *Earth and Environmental Science Transactions of The Royal Society of Edinburgh* **93**, 355–382.

Ferraro J. R., Nakamoto K. and Brown (2003) *Introductory Raman Spectroscopy*., Elsevier.

Fisk M. R. and Giovannoni S. J. (1999) Sources of nutrients and energy for a deep biosphere on Mars. *J. Geophys. Res.* **104**, 11805–11815.

Franchi I. A., Wright I. P., Sexton A. S. and Pillinger C. T. (1999) The oxygen-isotopic composition of Earth and Mars. *Meteoritics & Planetary Science* **34**, 657–661.

Garwood R. J., Oliver H. and Spencer A. R. T. (2020) An introduction to the Rhynie chert. *Geological Magazine* **157**, 47–64.

Gattacceca J., McCubbin F. M., Bouvier A. and Grossman J. N. (2020) The Meteoritical Bulletin, no. 108. *Meteorit Planet Sci* **55**, 1146–1150.

Gault B. (2016) A Brief Overview of Atom Probe Tomography Research. *Applied Microscopy* **46**, 117–126.

Gay P. and LeMaitre R. W. (1961) Some observations on "iddingsite." *American Mineralogist* **46**, 92–111.

Geiss J. and Hess D. C. (1958) Argon-Potassium Ages and the Isotopec Composition of Argon from Meteorites. *The Astrophysical Journal* **127**, 224.

Geuser F. D. and Gault B. (2017) Reflections on the Projection of Ions in Atom Probe Tomography. *Microscopy and Microanalysis* **23**, 238–246.

Gibson E. K., McKay D. S., Thomas-Keprta K. L., Wentworth S. J., Westall F., Steele A., Romanek C. S., Bell M. S. and Toporski J. (2001) Life on Mars: evaluation of the evidence within Martian meteorites ALH84001, Nakhla, and Shergotty. *Precambrian Research* **106**, 15–34.

Gibson E. K., Thomas-Keprta K. L., Clemett S. J. and McKay D. S. (2016) Martian Biosignatures: Tantalizing Evidence Within Martian Meteorites. **1912**, 2052.

Gilichinsky D. a., Wilson G. s., Friedmann E. i., Mckay C. p., Sletten R. s., Rivkina E. m., Vishnivetskaya T. a., Erokhina L. g., Ivanushkina N. e., Kochkina G. a., Shcherbakova V. a., Soina V. s., Spirina E. v., Vorobyova E. a., Fyodorov-Davydov D. g., Hallet B., Ozerskaya S. m., Sorokovikov V. a., Laurinavichyus K. s., Shatilovich A. v., Chanton J. p., Ostroumov V. e. and Tiedje J. m. (2007) Microbial Populations in Antarctic Permafrost: Biodiversity, State, Age, and Implication for Astrobiology. *Astrobiology* **7**, 275–311.

Gillet Ph., Barrat J. A., Deloule E., Wadhwa M., Jambon A., Sautter V., Devouard B., Neuville D., Benzerara K. and Lesourd M. (2002) Aqueous alteration in the Northwest Africa 817 (NWA 817) Martian meteorite. *Earth and Planetary Science Letters* **203**, 431–444.

Golden D. C., Ming D. W., Schwandt C. S., Morris R. V., Yang S. V. and Lofgren G. E. (2000) An experimental study on kinetically-driven precipitation of calcium-magnesium-iron carbonates from solution: Implications for the low-temperature formation of carbonates in martian meteorite Allan Hills 84001. *Meteoritics & Planetary Science* **35**, 457–465.

Golden D. C., Ming D. W., Schwandt C. S., Lauer H. V., Socki R. A., Morris R. V., Lofgren G. E. and Mckay G. A. (2001) Letter. A simple inorganic process for formation of carbonates, magnetite, and sulfides in martian meteorite ALH84001. *American Mineralogist* **86**, 370–375.

Golombek M. P. (1997) The Mars Pathfinder Mission. *J. Geophys. Res.* **102**, 3953–3965.

Golombek M. P., Cook R. A., Economou T., Folkner W. M., Haldemann A. F. C., Kallemeyn P. H., Knudsen J. M., Manning R. M., Moore H. J., Parker T. J., Rieder

R., Schofield J. T., Smith P. H. and Vaughan R. M. (1997) Overview of the Mars Pathfinder Mission and Assessment of Landing Site Predictions. *Science*.

Gooding J. L., Wentworth S. J. and Zolensky M. E. (1991) Aqueous alteration of the Nakhla meteorite. *Meteoritics* **26**, 135–143.

Goudge T. A., Head J. W., Mustard J. F. and Fassett C. I. (2012) An analysis of open-basin lake deposits on Mars: Evidence for the nature of associated lacustrine deposits and post-lacustrine modification processes. *Icarus* **219**, 211–229.

Goudge T. A., Aureli K. L., Head J. W., Fassett C. I. and Mustard J. F. (2015) Classification and analysis of candidate impact crater-hosted closed-basin lakes on Mars. *Icarus* **260**, 346–367.

Grant J. and Golombek M. (2018) Fourth Landing site Workshop - final recommendations made to NASA.https://marsnext.jpl.nasa.gov/workshops/2018-10/M2020_LSW_FinalOutcomeLetter_for_MMeyer_181023.pdf (2018) Accessed December 3, 2021

Greaves J. S., Richards A. M. S., Bains W., Rimmer P. B., Sagawa H., Clements D. L., Seager S., Petkowski J. J., Sousa-Silva C., Ranjan S., Drabek-Maunder E., Fraser H. J., Cartwright A., Mueller-Wodarg I., Zhan Z., Friberg P., Coulson I., Lee E. and Hoge J. (2021a) Phosphine gas in the cloud decks of Venus. *Nat Astron* **5**, 655–664.

Greaves J. S., Richards A. M. S., Bains W., Rimmer P. B., Clements D. L., Seager S., Petkowski J. J., Sousa-Silva C., Ranjan S. and Fraser H. J. (2021b) Reply to: No evidence of phosphine in the atmosphere of Venus from independent analyses. *Nat Astron* **5**, 636–639.

Greaves J. S., Richards A. M. S., Bains W., Rimmer P. B., Sagawa H., Clements D. L., Seager S., Petkowski J. J., Sousa-Silva C., Ranjan S., Drabek-Maunder E., Fraser H. J., Cartwright A., Mueller-Wodarg I., Zhan Z., Friberg P., Coulson I., Lee E. and Hoge J. (2021c) Addendum: Phosphine gas in the cloud deck of Venus. *Nat Astron* **5**, 726–728.

Greeley R. and Schneid B. D. (1991) Magma Generation on Mars: Amounts, Rates, and Comparisons with Earth, Moon, and Venus. *Science* **254**, 996–998.

Green J., Boardsen S. and Dong C. (2021) Magnetospheres of Terrestrial Exoplanets and Exomoons: Implications for Habitability and Detection. *ApJL* **907**, L45.

Grotzinger J. P., Crisp J., Vasavada A. R., Anderson R. C., Baker C. J., Barry R., Blake D. F., Conrad P., Edgett K. S., Ferdowski B., Gellert R., Gilbert J. B., Golombek M., Gómez-Elvira J., Hassler D. M., Jandura L., Litvak M., Mahaffy P., Maki J., Meyer M., Malin M. C., Mitrofanov I., Simmonds J. J., Vaniman D., Welch R. V. and Wiens R. C. (2012) Mars Science Laboratory Mission and Science Investigation. *Space Sci Rev* **170**, 5–56.

Guedel M., Dvorak R., Erkaev N., Kasting J., Khodachenko M., Lammer H., Pilat-Lohinger E., Rauer H., Ribas I. and Wood B. E. (2014) Astrophysical Conditions for Planetary Habitability. *arXiv:1407.8174 [astro-ph]*.

Guidry S. A. and Chafetz H. S. (1999) Preservation of Microbes in Geyserite and Siliceous Sinter: Yellowstone National Park, Wyoming. , 1152.

Guidry S. A. and Chafetz H. S. (2003) Siliceous Shrubs in Yellowstone's Hot Springs: Implications for Exobiological Investigations. *Lunar and Planetary Science XXXIV*.

Haberle R. M. (2015) SOLAR SYSTEM/SUN, ATMOSPHERES, EVOLUTION OF ATMOSPHERES | Planetary Atmospheres: Mars. In *Encyclopedia of Atmospheric Sciences (Second Edition)* (eds. G. R. North, J. Pyle, and F. Zhang). Academic Press, Oxford. pp. 168–177.

Halevy I. and Head III J. W. (2014) Episodic warming of early Mars by punctuated volcanism. *Nature Geosci* **7**, 865–868.

Hallis L. J. and Taylor G. J. (2011) Comparisons of the four Miller Range nakhlites, MIL 03346, 090030, 090032 and 090136: Textural and compositional observations of primary and secondary mineral assemblages: Comparisons of the four Miller Range nakhlites. *Meteoritics & Planetary Science* **46**, 1787–1803.

Hallis L. J., Taylor G. J., Nagashima K., Huss G. R., Needham A. W., Grady M. M. and Franchi I. A. (2012) Hydrogen isotope analyses of alteration phases in the nakhlite martian meteorites. *Geochimica et Cosmochimica Acta* **97**, 105–119.

Hartmann W. K. and Neukum G. (2001) Cratering Chronology and the Evolution of Mars. *Space Science Reviews* **96**, 165–194.

Head J. W. (2002) Northern lowlands of Mars: Evidence for widespread volcanic flooding and tectonic deformation in the Hesperian Period. *J. Geophys. Res.* **107**, 5003.

Head J. W., Forget F., Wordsworth R., Turbet M., Cassanelli J. and Palumbo A. (2018) Two oceans on Mars?: History, problems and prospects. In *The Ninth Moscow Solar System Symposium 9M-S3* pp. 15–18.

Heldmann J. L., Pollard W., McKay C. P., Marinova M. M., Davila A., Williams K. E., Lacelle D. and Andersen D. T. (2013) The high elevation Dry Valleys in Antarctica as analog sites for subsurface ice on Mars. *Planetary and Space Science* **85**, 53–58.

Hellman M. J. and Ramsey M. S. (2004) Analysis of hot springs and associated deposits in Yellowstone National Park using ASTER and AVIRIS remote sensing. *Journal of Volcanology and Geothermal Research* **135**, 195–219.

Hewins R. H., Humayun M., Barrat J.-A., Zanda B., Lorand J.-P., Pont S., Assayag N., Cartigny P., Yang S. and Sautter V. (2020) Northwest Africa 8694, a ferroan chassignite: Bridging the gap between nakhlites and chassignites. *Geochimica et Cosmochimica Acta* **282**, 201–226.

Hicks L. J., Bridges J. C. and Gurman S. J. (2014) Ferric saponite and serpentine in the nakhlite martian meteorites. *Geochimica et Cosmochimica Acta* **136**, 194–210.

Horowitz N. H. (1976) The search for life in the solar system. *Acc. Chem. Res.* **9**, 1–7.

Horvath D. G. and Andrews-Hanna J. C. (2017) Reconstructing the past climate at Gale crater, Mars, from hydrological modeling of late-stage lakes: Lake Hydrology at Gale Crater. *Geophys. Res. Lett.* **44**, 8196–8204.

Hu S., Lin Y., Zhang J., Hao J., Xing W., Zhang T., Yang W. and Changela H. (2019) Ancient geologic events on Mars revealed by zircons and apatites from the Martian regolith breccia NWA 7034. *Meteoritics & Planetary Science* **54**, 850–879.

Hu S., Lin Y., Zhang J., Hao J., Yamaguchi A., Zhang T., Yang W. and Changela H. (2020) Volatiles in the martian crust and mantle: Clues from the NWA 6162 shergottite. *Earth and Planetary Science Letters* **530**, 115902.

Huang B. (2010) Super-resolution optical microscopy: multiple choices. *Current Opinion in Chemical Biology* **14**, 10–14.

Huber R., Eder W., Heldwein S., Wanner G., Huber H., Rachel R. and Stetter K. O. (1998) Thermocrinis ruber gen. nov., sp. nov., a Pink-Filament-Forming Hyperthermophilic Bacterium Isolated from Yellowstone National Park. *Applied and Environmental Microbiology*.

Hurwitz S. and Lowenstern J. B. (2014) Dynamics of the Yellowstone hydrothermal system: YELLOWSTONE HYDROTHERMAL SYSTEM. *Rev. Geophys.* **52**, 375–411.

Hynek B. M., Beach M. and Hoke M. R. T. (2010) Updated global map of Martian valley networks and implications for climate and hydrologic processes. *J. Geophys. Res.* **115**, E09008.

Igisu M., Nakashima S., Ueno Y., Awramik S. M. and Maruyama S. (2006) *In situ* Infrared Microspectroscopy of ~850 Million-Year-Old Prokaryotic Fossils. *Appl Spectrosc* **60**, 1111–1120.

Imae N., Ikeda Y., Shinoda K., Kojima H. and Iwata N. (2003) Yamato nahklites: Petrography and mineralogy. *Antarctic Meteorite Research* **16**, 13–33.

Imae N., Ikeda Y. and Kojima H. (2005) Petrology of the Yamato nakhlites. *Meteoritics & Planetary Science* **40**, 1581–1598.

Imae N. and Ikeda Y. (2007) Petrology of the Miller Range 03346 nakhlite in comparison with the Yamato-000593 nakhlite. *Meteoritics & Planetary Science* **42**, 171–184.

Ingersoll A. P. (1970) Mars: Occurrence of Liquid Water. *Science* **168**, 972–973.

Jakosky B. M. and Phillips R. J. (2001) Mars' volatile and climate history. *Nature* **412**, 237–244.

Jakosky B. M., Nealson K. H., Bakermans C., Ley R. E. and Mellon M. T. (2003) Subfreezing Activity of Microorganisms and the Potential Habitability of Mars' Polar Regions. *Astrobiology* **3**, 343–350.

Jones B. (2021) Siliceous sinters in thermal spring systems: Review of their mineralogy, diagenesis, and fabrics. *Sedimentary Geology* **413**, 105820.

Jones J. H. (1986) A discussion of isotopic systematics and mineral zoning in the shergottites: Evidence for a 180 m.y. igneous crystallization age. *Geochimica et Cosmochimica Acta* **50**, 969–977.

Jones J. H. (2015) Various aspects of the petrogenesis of the Martian shergottite meteorites. *Meteoritics & Planetary Science* **50**, 674–690.

Karahka M., Xia Y. and Kreuzer H. J. (2015) The mystery of missing species in atom probe tomography of composite materials. *Appl. Phys. Lett.* **107**, 062105.

Kelly T. F. and Larson D. J. (2012) Atom Probe Tomography 2012. *Annu. Rev. Mater. Res.* **42**, 1–31.

Kenrick P., Wellman C. H., Schneider H. and Edgecombe G. D. (2012) A timeline for terrestrialization: consequences for the carbon cycle in the Palaeozoic. *Philosophical Transactions of the Royal Society B: Biological Sciences* **367**, 519–536.

Kidston R. and Lang W. H. (1921) XXXIII.—On Old Red Sandstone Plants showing Structure, from the Rhynie Chert Bed, Aberdeenshire. Part V. The Thallophyta occurring in the Peat-Bed; the Succession of the Plants throughout a Vertical Section of the Bed, and the Conditions of Accumulation and Preservation of the Deposit. *Earth and Environmental Science Transactions of The Royal Society of Edinburgh* **52**, 855–902.

King A. J., Schofield P. F. and Russell S. S. (2017) Type 1 aqueous alteration in CM carbonaceous chondrites: Implications for the evolution of water-rich asteroids. *Meteorit Planet Sci* **52**, 1197–1215.

Klein H. P., Lederberg J., Rich A., Horowitz N. H., Oyama V. I. and Levin G. V. (1976) The Viking Mission search for life on Mars. *Nature* **262**, 24–27.

Klein H. P. (1979) The Viking mission and the search for life on Mars. *Rev. Geophys.* **17**, 1655.

Klein H. P. (1998) The search for life on Mars: What we learned from Viking. *J. Geophys. Res.* **103**, 28463–28466.

Klein H. P. (1999) Did Viking Discover Life on Mars? *Orig Life Evol Biosph* **29**, 625–631.

Kouketsu Y., Mizukami T., Mori H., Endo S., Aoya M., Hara H., Nakamura D. and Wallis S. (2014) A new approach to develop the Raman carbonaceous material geothermometer for low-grade metamorphism using peak width. *Island Arc* **23**, 33–50.

Krasnopolsky V. A., Maillard J. P. and Owen T. C. (2004) Detection of methane in the martian atmosphere: evidence for life? *Icarus* **172**, 537–547.

Kuebler K., Jolliff B. L., Wang A. and Haskin L. A. (2004) A Survey of Olivine Alteration Products Using Raman Spectroscopy. *Lunar and Planetary Science XXXV: Martian Meteorites: Chemical Weathering*.

Lapen T. J., Righter M., Brandon A. D., Debaille V., Beard B. L., Shafer J. T. and Peslier A. H. (2010) A Younger Age for ALH84001 and Its Geochemical Link to Shergottite Sources in Mars. *Science* **328**, 347–351.

Larson D. J., Prosa T. J., Ulfig R. M., Geiser B. P. and Kelly T. F. (2013) History of APT and LEAP. In *Local Electrode Atom Probe Tomography: A User's Guide* (eds. D. J. Larson, T. J. Prosa, R. M. Ulfig, B. P. Geiser, and T. F. Kelly). Springer, New York, NY. pp. 1–23.

Lasne J., Noblet A., Szopa C., Navarro-González R., Cabane M., Poch O., Stalport F., François P., Atreya S. k. and Coll P. (2016) Oxidants at the Surface of Mars: A Review in Light of Recent Exploration Results. *Astrobiology* **16**, 977–996.

Lasue J., Clifford S. M., Conway S. J., Mangold N. and Butcher F. E. G. (2019) Chapter 7 - The Hydrology of Mars Including a Potential Cryosphere. In *Volatiles in the Martian Crust* (eds. J. Filiberto and S. P. Schwenzer). Elsevier. pp. 185–246.

Lauro S. E., Pettinelli E., Caprarelli G., Guallini L., Rossi A. P., Mattei E., Cosciotti B., Cicchetti A., Soldovieri F., Cartacci M., Di Paolo F., Noschese R. and Orosei R. (2021) Multiple subglacial water bodies below the south pole of Mars unveiled by new MARSIS data. *Nat Astron* **5**, 63–70.

Lee M. R., Bland P. A. and Graham G. (2003) Preparation of TEM samples by focused ion beam (FIB) techniques: applications to the study of clays and phyllosilicates in meteorites. *Mineral. mag.* **67**, 581–592.

Lee M. R. (2010) Transmission electron microscopy (TEM) of Earth and planetary materials: A review. *Mineral. mag.* **74**, 1–27.

Lee M. R., Tomkinson T., Mark D. F., Stuart F. M. and Smith C. L. (2013) Evidence for silicate dissolution on Mars from the Nakhla meteorite. *Meteorit Planet Sci* **48**, 224–240.

Lee M. R., MacLaren I., Andersson S. M. L., Kovács A., Tomkinson T., Mark D. F. and Smith C. L. (2015) Opal-A in the Nakhla meteorite: A tracer of ephemeral liquid water in the Amazonian crust of Mars. *Meteoritics & Planetary Science* **50**, 1362–1377.

Lee M. R. and Chatzitheodoridis E. (2016) Replacement of glass in the Nakhla meteorite by berthierine: Implications for understanding the origins of aluminum-rich phyllosilicates on Mars. *Meteorit Planet Sci* **51**, 1643–1653.

Lee M. R., Daly L., Cohen B. E., Hallis L. J., Griffin S., Trimby P., Boyce A. and Mark D. F. (2018) Aqueous alteration of the Martian meteorite Northwest Africa 817: Probing fluid–rock interaction at the nakhlite launch site. *Meteoritics & Planetary Science* **53**, 2395–2412.

Léveillé R. (2010) A half-century of terrestrial analog studies: From craters on the Moon to searching for life on Mars. *Planetary and Space Science* **58**, 631–638.

Levin G. V. and Levin R. L. (1998) Liquid water and life on Mars. In *Instruments, Methods, and Missions for Astrobiology* Instruments, Methods, and Missions for Astrobiology. SPIE. pp. 30–41.

Levin G. V. and Straat P. A. (2016) The Case for Extant Life on Mars and Its Possible Detection by the Viking Labeled Release Experiment. *Astrobiology* **16**, 798–810.

Li J.-W., Vasconcelos P. M., Zhou M.-F., Deng X.-D., Cohen B., Bi S.-J., Zhao X.-F. and Selby D. (2014) Longevity of magmatic–hydrothermal systems in the Daye Cu–Fe–Au District, eastern China with implications for mineral exploration. *Ore Geology Reviews* **57**, 375–392.

Lillis R. J., Robbins S., Manga M., Halekas J. S. and Frey H. V. (2013) Time history of the Martian dynamo from crater magnetic field analysis: TIME HISTORY OF THE MARTIAN DYNAMO. *J. Geophys. Res. Planets* **118**, 1488–1511.

Limaye S. S., Mogul R., Smith D. J., Ansari A. H., Słowik G. P. and Vaishampayan P. (2018) Venus' Spectral Signatures and the Potential for Life in the Clouds. *Astrobiology* **18**, 1181–1198.

Lipschutz M. E. and Schultz L. (2014) Chapter 28 - Meteorites. In *Encyclopedia of the Solar System (Third Edition)* (eds. T. Spohn, D. Breuer, and T. V. Johnson). Elsevier, Boston. pp. 625–655.

Liu J., Taylor S. D., Qafoku O., Arey B. W., Colby R., Eaton A., Bartrand J., Shutthanandan V., Manandhar S. and Perea D. E. (2022) Visualizing the Distribution of Water in Nominally Anhydrous Minerals at the Atomic Scale: Insights From Atom Probe Tomography on Fayalite. *Geophysical Research Letters* **49**.

Liu Y., Tice M. M., Schmidt M. E., Treiman A. H., Kizovski T. V., Hurowitz J. A., Allwood A. C., Henneke J., Pedersen D. A. K., VanBommel S. J., Jones M. W. M., Knight A. L., Orenstein B. J., Clark B. C., Elam W. T., Heirwegh C. M., Barber T., Beegle L. W., Benzerara K., Bernard S., Beyssac O., Bosak T., Brown A. J., Cardarelli E. L., Catling D. C., Christian J. R., Cloutis E. A., Cohen B. A., Davidoff S., Fairén A. G., Farley K. A., Flannery D. T., Galvin A., Grotzinger J. P., Gupta S., Hall J., Herd C. D. K., Hickman-Lewis K., Hodyss R. P., Horgan B. H. N., Johnson J. R., Jørgensen J. L., Kah L. C., Maki J. N., Mandon L., Mangold N., McCubbin F. M., McLennan S. M., Moore K., Nachon M., Nemere P., Nothdurft L. D., Núñez J. I., O'Neil L., Quantin-Nataf C. M., Sautter V., Shuster D. L., Siebach K. L., Simon J. I., Sinclair K. P., Stack K. M., Steele A., Tarnas J. D., Tosca N. J., Uckert K., Udry A., Wade L. A., Weiss B. P., Wiens R. C., Williford K. H. and Zorzano M.-P. (2022) An olivine cumulate outcrop on the floor of Jezero crater, Mars. *Science*, eabo2756.

Lodders K. (1998) A survey of shergottite, nakhlite and chassigny meteorites whole-rock compositions. *Meteoritics & Planetary Science* **33**, A183–A190.

Mackie W. (1914) The rock series of Craigbeg and Ord Hill, Rhynie, Aberdeenshire. *Transactions of the Edinburgh Geological Society* **10**, 205–236.

Malin M. C. and Edgett K. S. (1999) Oceans or seas in the Martian northern lowlands: High resolution imaging tests of proposed coastlines. *Geophys. Res. Lett.* **26**, 3049–3052.

Mark D. F., Rice C. M., Fallick A. E., Trewin N. H., Lee M. R., Boyce A. and Lee J. K. W. (2011) 40Ar/39Ar dating of hydrothermal activity, biota and gold mineralization in the Rhynie hot-spring system, Aberdeenshire, Scotland. *Geochimica et Cosmochimica Acta* **75**, 555–569.

mars.nasa.gov (2021) Surface Operations for Perseverance.https://mars.nasa.gov/mars2020/timeline/surface-operations/ (2021) Accessed December 3, 2021

mars.nasa.gov (2022) NASA Will Inspire World When It Returns Mars Samples to Earth in 2033. *NASA Mars Exploration*.https://mars.nasa.gov/news/9233/nasa-will-inspire-world-when-it-returns-mars-samples-to-earth-in-2033 (2022) Accessed July 29, 2022

Martel J., Young D., Peng H.-H., Wu C.-Y. and Young J. D. (2012) Biomimetic Properties of Minerals and the Search for Life in the Martian Meteorite ALH84001. *Annu. Rev. Earth Planet. Sci.* **40**, 167–193.

Marti K., Kim J. S., Thakur A. N., McCoy T. J. and Keil K. (1995) Signatures of the Martian Atmosphere in Glass of the Zagami Meteorite. *Science* **267**, 1981–1984.

Martínez G. M. and Renno N. O. (2013) Water and Brines on Mars: Current Evidence and Implications for MSL. *Space Sci Rev* **175**, 29–51.

Martín-Torres J., Zorzano M.-P., Soria-Salinas Á., Nazarious M. I., Konatham S., Mathanlal T., Ramachandran A. V., Ramírez-Luque J.-A. and Mantas-Nakhai R. (2020) The HABIT (HabitAbility: Brine Irradiation and Temperature) environmental instrument for the ExoMars 2022 Surface Platform. *Planetary and Space Science* **190**, 104968.

Mason B., Nelon J. a., Muir P. and Taylor S. r (1976) The Composition of the Chassigny Meteorite. *Meteoritics* **11**, 21–27.

Matsubara Y., Howard A. D. and Gochenour J. P. (2013) Hydrology of early Mars: Valley network incision: HYDROLOGY OF EARLY MARS: VALLEY INCISION. *J. Geophys. Res. Planets* **118**, 1365–1387.

McCarroll I. E., Daly L., White L. F. and Cairney J. M. (2022) Atom probe tomography and correlative microscopy: Key techniques for future planetary science studies. *MRS Bulletin* **47**, 696–705.

McCarthy T. S., Erlank A. J., Willis J. P. and Ahrens L. H. (1974) NEW CHEMICAL ANALYSES OF SIX ACHONDRITES AND ONE CHONDRITE. *Meteoritics* **9**, 215–221.

McCubbin F. M., Elardo S. M., Shearer C. K., Smirnov A., Hauri E. H. and Draper D. S. (2013) A petrogenetic model for the comagmatic origin of chassignites and nakhlites: Inferences from chlorine-rich minerals, petrology, and geochemistry. *Meteorit Planet Sci* **48**, 819–853.

McCubbin F. M., Boyce J. W., Srinivasan P., Santos A. R., Elardo S. M., Filiberto J., Steele A. and Shearer C. K. (2016) Heterogeneous distribution of H_2O in the Martian interior: Implications for the abundance of H_2O in depleted and enriched mantle sources. *Meteorit Planet Sci* **51**, 2036–2060.

McKay C. P. and Davis W. L. (1991) Duration of liquid water habitats on early Mars. *Icarus* **90**, 214–221.

McKay C. P., Imre Friedman E., Wharton R. A. and Davies W. L. (1992) History of water on Mars: A biological perspective. *Advances in Space Research* **12**, 231–238.

Mckay C. P. (1997) The Search for Life on Mars. In *Planetary and Interstellar Processes Relevant to the Origins of Life* (ed. D. C. B. Whittet). Springer Netherlands, Dordrecht. pp. 263–289.

McKay D. S., Gibson E. K., Thomas-Keprta K. L., Vali H., Romanek C. S., Clemett S. J., Chillier X. D. F., Maechling C. R. and Zare R. N. (1996) Search for Past Life on Mars: Possible Relic Biogenic Activity in Martian Meteorite ALH84001. *Science* **273**, 924–930.

McLoughlin N., Grosch E. G., Vullum P. E., Guagliardo P., Saunders M. and Wacey D. (2019) Critically testing olivine-hosted putative martian biosignatures in the Yamato 000593 meteorite—Geobiological implications. *Geobiology* **17**, 691–707.

McMahon S., Bosak T., Grotzinger J. P., Milliken R. E., Summons R. E., Daye M., Newman S. A., Fraeman A., Williford K. H. and Briggs D. E. G. (2018) A Field Guide to Finding Fossils on Mars. *Journal of Geophysical Research: Planets* **123**, 1012–1040.

McMahon S. and Cosmidis J. (2021) False biosignatures on Mars: anticipating ambiguity. *Journal of the Geological Society*, jgs2021-050.

McSween H. Y. (1994) What we have learned about Mars from SNC meteorites. *Meteoritics* **29**, 757–779.

McSween H. Y. (2015) Petrology on Mars. *American Mineralogist* **100**, 2380–2395.

McSween H. Y. (2019) The Search for Biosignatures in Martian Meteorite Allan Hills 84001. In *Biosignatures for Astrobiology* (eds. B. Cavalazzi and F. Westall). Advances in Astrobiology and Biogeophysics. Springer International Publishing, Cham. pp. 167–182.

McSween H. Y., Grady M., McKeegan K., Beaty D. and Carrier B. (2021) Why Mars Sample Return is a Mission Campaign of Compelling Importance to Planetary Science and Exploration. **53**.

MEPAG Next Decade Science Analysis Group (2008) Science priorities for Mars sample return. *Astrobiology* **8**, 489–435.

Meyer C. (2012) Martian Meteorite Compendium.https://curator.jsc.nasa.gov/antmet/mmc/index.cfm (2012) Accessed March 30, 2022

Michalski J. R., Onstott T. C., Mojzsis S. J., Mustard J., Chan Q. H. S., Niles P. B. and Johnson S. S. (2018) The Martian subsurface as a potential window into the origin of life. *Nature Geosci* **11**, 21–26.

Milbury C., Schubert G., Raymond C. A., Smrekar S. E. and Langlais B. (2012) The history of Mars' dynamo as revealed by modeling magnetic anomalies near Tyrrhenus Mons and Syrtis Major: MARS' DYNAMO HISTORY. *J. Geophys. Res.* **117**.

Mischna M. A., Baker V., Milliken R., Richardson M. and Lee C. (2013) Effects of obliquity and water vapor/trace gas greenhouses in the early martian climate: OBLIQUITY/TRACE GAS GREENHOUSES ON MARS. *J. Geophys. Res. Planets* **118**, 560–576.

Mittelholz A., Johnson C. L., Feinberg J. M., Langlais B. and Phillips R. J. (2020) Timing of the martian dynamo: New constraints for a core field 4.5 and 3.7 Ga ago. *Sci. Adv.* **6**, eaba0513.

Mittlefehldt D. W. (1994) ALH84001, a cumulate orthopyroxenite member of the martian meteorite clan. *Meteoritics* **29**, 214–221.

Moore J. M. and Howard A. D. (2005) Large alluvial fans on Mars. *J. Geophys. Res.* **110**, E04005.

Morbidelli A. and Gladman B. (1998) Orbital and temporal distributions of meteorites originating in the asteroid belt. *Meteoritics & Planetary Science* **33**, 999–1016.

Morbidelli A., Chambers J., Lunine J. I., Petit J. M., Robert F., Valsecchi G. B. and Cyr K. E. (2000) Source regions and timescales for the delivery of water to the Earth. *Meteoritics & Planetary Science* **35**, 1309–1320.

Muirhead B. K., Nicholas A. K., Umland J., Sutherland O. and Vijendran S. (2020) Mars Sample Return Campaign Concept Status. *Acta Astronautica* **176**, 131–138.

Mumma M. J. (2012) The Search for Life on Mars. In Origin of Life Gordon Research Conference.

Nakamura E., Kobayashi K., Tanaka R., Kunihiro T., Kitagawa H., Potiszil C., Ota T., Sakaguchi C., Yamanaka M., Yati Y., Usui T., Tsuda Y., Watanabe S., Abe M., Okada T. and Yada T. (2021) A first look at the interior and exterior of Ryugu preserved in samples collected by Hayabusa2. In Hayabusa Symposium 2021.

Nascimento-Dias B. L., de Oliveira D. F., Machado A. S., Araújo O. M. O., Lopes R. T. and dos Anjos M. J. (2018) Utilization of nondestructive techniques for analysis of the Martian meteorite NWA 6963 and its implications for astrobiology. *X-Ray Spectrometry* **47**, 86–91.

Neish C. D., Hamilton C. W., Hughes S. S., Nawotniak S. K., Garry W. B., Skok J. R., Elphic R. C., Schaefer E., Carter L. M., Bandfield J. L., Osinski G. R., Lim D. and Heldmann J. L. (2017) Terrestrial analogues for lunar impact melt flows. *Icarus* **281**, 73–89.

Nellist P. D. (2019) Scanning Transmission Electron Microscopy. In *Springer Handbook of Microscopy* (eds. P. W. Hawkes and J. C. H. Spence). Springer Handbooks. Springer International Publishing, Cham. pp. 49–99.

Neumann G. and Terrence M. (2007) Goddard Space Flight Center Image Gallery.https://attic.gsfc.nasa.gov/mola/images.html (2007) Accessed March 28, 2022

Neveu M., Hays L. E., Voytek M. A., New M. H. and Schulte M. D. (2018) The Ladder of Life Detection. *Astrobiology* **18**, 1375–1402.

Newbury D. E. (2002) X-ray microanalyses in the variable pressure (environmental) scanning electron microscope. *J. Res. Natl. Inst. Stand. Technol.* **107**, 567.

Noguchi T., Nakamura T., Misawa K., Imae N., Aoki T. and Toh S. (2009) Laihunite and jarosite in the Yamato 00 nakhlites: Alteration products on Mars?: LAIHUNITE AND JAROSITE IN NAKHLITES. *J. Geophys. Res.* **114**, n/a-n/a.

Nylese T. L., Berry A. and Oscher S. (2015) Elemental Analysis of Silicon in Plant Material with Variable-Pressure SEM. *Micros. Today* **23**, 26–31.

Nyquist L. E., Bogard D. D., Shih C.-Y., Greshake A., Stöffler D. and Eugster O. (2001) Ages and Geologic Histories of Martian Meteorites. *Space Science Reviews* **96**, 105–164.

Nyquist L. E., Shih C.-Y., McCubbin F. M., Santos A. R., Shearer C. K., Peng Z. X., Burger P. V. and Agee C. B. (2016) Rb-Sr and Sm-Nd isotopic and REE studies of igneous components in the bulk matrix domain of Martian breccia Northwest Africa 7034. *Meteorit Planet Sci* **51**, 483–498.

Ohmoto H., Runnegar B., Kump L. R., Fogel M. L., Kamber B., Anbar A. D., Knauth P. L., Lowe D. R., Sumner D. Y. and Watanabe Y. (2008) Biosignatures in Ancient Rocks: A Summary of Discussions at a Field Workshop on Biosignatures in Ancient Rocks. *Astrobiology* **8**, 883–907.

Olcott Marshall A. and Marshall C. P. (2015) Vibrational spectroscopy of fossils ed. A. Smith. *Palaeontology* **58**, 201–211.

Ordonez-Etxeberria I., Hueso R. and Sánchez-Lavega A. (2018) A systematic search of sudden pressure drops on Gale crater during two Martian years derived from MSL/REMS data. *Icarus* **299**, 308–330.

Orosei R., Lauro S. E., Pettinelli E., Cicchetti A., Coradini M., Cosciotti B., Di Paolo F., Flamini E., Mattei E., Pajola M., Soldovieri F., Cartacci M., Cassenti F., Frigeri A., Giuppi S., Martufi R., Masdea A., Mitri G., Nenna C., Noschese R., Restano M. and Seu R. (2018) Radar evidence of subglacial liquid water on Mars. *Science* **361**, 490–493.

Osinski G. R., Spray J. G. and Lee P. (2001) Impact-induced hydrothermal activity within the Haughton impact structure, arctic Canada: Generation of a transient, warm, wet oasis. *Meteoritics & Planetary Science* **36**, 731–745.

Oura Y., Shirai N. and Ebihara M. (2003) Chemical composition of Yamato (Y) 000593 and Y000749: Neutron-induced prompt gamma-ray analysis study. *Antarctic Meteorite Research* **16**, 80–93.

Owen T., Biemann K., Rushneck D. R., Biller J. E., Howarth D. W. and Lafleur A. L. (1977) The composition of the atmosphere at the surface of Mars. *Journal of Geophysical Research (1896-1977)* **82**, 4635–4639.

Parker T. J., Stephen Saunders R. and Schneeberger D. M. (1989) Transitional morphology in West Deuteronilus Mensae, Mars: Implications for modification of the lowland/upland boundary. *Icarus* **82**, 111–145.

Parker T. J., Gorsline D. S., Saunders R. S., Pieri D. C. and Schneeberger D. M. (1993) Coastal geomorphology of the Martian northern plains. *J. Geophys. Res.* **98**, 11061.

Parry S. F., Noble S. R., Crowley Q. G. and Wellman C. H. (2013) Reply to Discussion on 'A high-precision U–Pb age constraint on the Rhynie Chert Konservat-Lagerstätte: time scale and other implications': *Journal* , 168, 863–872. *Journal of the Geological Society* **170**, 703–706.

Pavlov A. A., Vasilyev G., Ostryakov V. M., Pavlov A. K. and Mahaffy P. (2012) Degradation of the organic molecules in the shallow subsurface of Mars due to irradiation by cosmic rays: ORGANIC MATTER AND COSMIC RAYS ON MARS. *Geophys. Res. Lett.* **39**, n/a-n/a.

Pavlov A. K., Blinov A. V. and Konstantinov A. N. (2002) Sterilization of Martian surface by cosmic radiation. *Planetary and Space Science* **50**, 669–673.

Peng Z., Vurpillot F., Choi P.-P., Li Y., Raabe D. and Gault B. (2018) On the detection of multiple events in atom probe tomography. *Ultramicroscopy* **189**, 54–60.

Pikuta E. V., Hoover R. B. and Tang J. (2007) Microbial Extremophiles at the Limits of Life. *Critical Reviews in Microbiology* **33**, 183–209.

Poinar G., Kerp H. and Hass H. (2008) Palaeonema phyticum gen. n., sp. n. (Nematoda: Palaeonematidae fam. n.), a Devonian nematode associated with early land plants. *Nematology* **10**, 9–14.

Pollack J. B., Kasting J. F., Richardson S. M. and Poliakoff K. (1987) The case for a wet, warm climate on early Mars. *Icarus* **71**, 203–224.

Preston L. J. and Genge M. J. (2010) The Rhynie Chert, Scotland, and the Search for Life on Mars. *Astrobiology* **10**, 549–560.

Preston L. J. and Dartnell L. R. (2014) Planetary habitability: lessons learned from terrestrial analogues. *International Journal of Astrobiology* **13**, 81–98.

Prieto-Ballesteros O., Rodríguez N., Kargel J. S., Kessler C. G., Amils R. and Remolar D. F. (2003) Tírez Lake as a Terrestrial Analog of Europa. *Astrobiology* **3**, 863–877.

Prior G. T. (1912) The meteoric stones of El Nakhla El Baharia (Egypt). *Mineral. mag. j. Mineral. Soc.* **16**, 274–281.

Prosa T. J., Geiser B. P., Lawrence D., Olson D. and Larson D. J. (2014) Developing detection efficiency standards for atom probe tomography. In *Instrumentation, Metrology, and Standards for Nanomanufacturing, Optics, and Semiconductors VIII* Instrumentation, Metrology, and Standards for Nanomanufacturing, Optics, and Semiconductors VIII. SPIE. pp. 38–45.

Qu Y., Engdahl A., Zhu S., Vajda V. and McLoughlin N. (2015) Ultrastructural Heterogeneity of Carbonaceous Material in Ancient Cherts: Investigating Biosignature Origin and Preservation. *Astrobiology* **15**, 825–842.

Quinn R. C., Martucci H. F. H., Miller S. R., Bryson C. E., Grunthaner F. J. and Grunthaner P. J. (2013) Perchlorate Radiolysis on Mars and the Origin of Martian Soil Reactivity. *Astrobiology* **13**, 515–520.

Ramirez R. M. and Craddock R. A. (2018) The geological and climatological case for a warmer and wetter early Mars. *Nature Geosci* **11**, 230–237.

Ramkissoon N. K., Turner S. M. R., Macey M. C., Schwenzer S. P., Reed M. H., Pearson V. K., Olsson-Francis K. and Glavin D. (2021) Exploring the environments of Martian impact-generated hydrothermal systems and their potential to support life. *Meteorit Planet Sci* **56**, 1350–1368.

Reddy S. M., Saxey D. W., Rickard W. D. A., Fougerouse D., Montalvo S. D., Verberne R. and Riessen A. van (2020) Atom Probe Tomography: Development and Application to the Geosciences. *Geostandards and Geoanalytical Research* **44**, 5–50.

Reimer L. and Kohl H. (2008) *Transmission Electron Microscopy: Physics of Image Formation*., Springer Science & Business Media.

Rice C. M., Trewin N. H. and Anderson L. I. (2002) Geological setting of the Early Devonian Rhynie cherts, Aberdeenshire, Scotland: an early terrestrial hot spring system. *Journal of the Geological Society* **159**, 203–214.

Rivera-Valentín E. G., Chevrier V. F., Soto A. and Martínez G. (2020) Distribution and habitability of (meta)stable brines on present-day Mars. *Nat Astron* **4**, 756–761.

Rodriguez J. A. P., Fairén A. G., Tanaka K. L., Zarroca M., Linares R., Platz T., Komatsu G., Miyamoto H., Kargel J. S., Yan J., Gulick V., Higuchi K., Baker V. R. and Glines N. (2016) Tsunami waves extensively resurfaced the shorelines of an early Martian ocean. *Sci Rep* **6**, 25106.

Ruff S. W. and Farmer J. D. (2016) Silica deposits on Mars with features resembling hot spring biosignatures at El Tatio in Chile. *Nat Commun* **7**, 13554.

Rull F., Martinez-Frias J., Sansano A., Medina J. and Edwards H. G. M. (2004) Comparative micro-Raman study of the Nakhla and Vaca Muerta meteorites. *J. Raman Spectrosc.* **35**, 497–503.

Rull F., Maurice S., Hutchinson I., Moral A., Perez C., Diaz C., Colombo M., Belenguer T., Lopez-Reyes G., Sansano A., Forni O., Parot Y., Striebig N., Woodward S., Howe C., Tarcea N., Rodriguez P., Seoane L., Santiago A., Rodriguez-Prieto J. A., Medina J., Gallego P., Canchal R., Santamaría P., Ramos G., Vago J. L. and on behalf of the R. T. (2017) The Raman Laser Spectrometer for the ExoMars Rover Mission to Mars. *Astrobiology* **17**, 627–654.

Rull F., Veneranda M., Manrique-Martinez J. A., Sanz-Arranz A., Saiz J., Medina J., Moral A., Perez C., Seoane L., Lalla E., Charro E., Lopez J. M., Nieto L. M. and Lopez-Reyes G. (2021) Spectroscopic study of terrestrial analogues to support rover missions to Mars – A Raman-centred review. *Analytica Chimica Acta*, 339003.

Santos A. R., Agee C. B., McCubbin F. M., Shearer C. K., Burger P. V., Tartèse R. and Anand M. (2015) Petrology of igneous clasts in Northwest Africa 7034: Implications for the petrologic diversity of the martian crust. *Geochimica et Cosmochimica Acta* **157**, 56–85.

Sautter V., Barrat J. A., Jambon A., Lorand J. P., Gillet P., Javoy M., Joron J. L. and Lesourd M. (2002) A new Martian meteorite from Morocco: the nakhlite North West Africa 817. *Earth and Planetary Science Letters* **195**, 223–238.

Saxey D. W., Moser D. E., Piazolo S., Reddy S. M. and Valley J. W. (2018) Atomic worlds: Current state and future of atom probe tomography in geoscience. *Scripta Materialia* **148**, 115–121.

Schuerger A. C., Golden D. C. and Ming D. W. (2012) Biotoxicity of Mars soils: 1. Dry deposition of analog soils on microbial colonies and survival under Martian conditions. *Planetary and Space Science* **72**, 91–101.

Schwenzer S. P., Abramov O., Allen C. C., Clifford S. M., Cockell C. S., Filiberto J., Kring D. A., Lasue J., McGovern P. J., Newsom H. E., Treiman A. H., Vaniman D. T. and Wiens R. C. (2012) Puncturing Mars: How impact craters interact with the Martian cryosphere. *Earth and Planetary Science Letters* **335–336**, 9–17.

Schwieterman E. W., Kiang N. Y., Parenteau M. N., Harman C. E., DasSarma S., Fisher T. M., Arney G. N., Hartnett H. E., Reinhard C. T., Olson S. L., Meadows V. S., Cockell C. S., Walker S. I., Grenfell J. L., Hegde S., Rugheimer S., Hu R. and Lyons T. W. (2018) Exoplanet Biosignatures: A Review of Remotely Detectable Signs of Life. *Astrobiology* **18**, 663–708.

Scott E. R. D. (1999) Origin of carbonate-magnetite-sulfide assemblages in Martian meteorite ALH84001. *Journal of Geophysical Research: Planets* **104**, 3803–3813.

Segura T. L., Toon O. B. and Colaprete A. (2008) Modeling the environmental effects of moderate-sized impacts on Mars. *J. Geophys. Res.* **113**, E11007.

Seybold H. J., Kite E. and Kirchner J. W. (2018) Branching geometry of valley networks on Mars and Earth and its implications for early Martian climate. *Science Advances*.

Shirai N., Oura Y. and Ebihara M. (2002) Chemical Composition of Newly Collected Antarctic Nakhlites, Y000593 and Y000749. In Unmixing the SNCs: Chemical, Isotopic, and Petrologic Components of the Martian Meteorites. Lunar and Planetary Institute. p. Abstract \#6017.

Sijbrandij S. J., Larson D. J. and Miller M. K. (1998) Atom Probe Field Ion Microscopy of High Resistivity Materials. *Microscopy and Microanalysis* **4**, 90–91.

Smith D. E., Zuber M. T., Frey H. V., Garvin J. B., Head J. W., Muhleman D. O., Pettengill G. H., Phillips R. J., Solomon S. C., Zwally H. J., Banerdt W. B., Duxbury T. C., Golombek M. P., Lemoine F. G., Neumann G. A., Rowlands D. D., Aharonson O., Ford P. G., Ivanov A. B., Johnson C. L., McGovern P. J., Abshire J. B., Afzal R. S. and Sun X. (2001) Mars Orbiter Laser Altimeter: Experiment summary after the first year of global mapping of Mars. *J. Geophys. Res.* **106**, 23689–23722.

Smith E. and Dent G. (2019) *Modern Raman Spectroscopy: A Practical Approach*., John Wiley & Sons.

Snellen I. a. G., Guzman-Ramirez L., Hogerheijde M. R., Hygate A. P. S. and Tak F. F. S. van der (2020) Re-analysis of the 267 GHz ALMA observations of Venus - No statistically significant detection of phosphine. *A&A* **644**, L2.

Sousa-Silva C., Seager S., Ranjan S., Petkowski J. J., Zhan Z., Hu R. and Bains W. (2020) Phosphine as a Biosignature Gas in Exoplanet Atmospheres. *Astrobiology* **20**, 235–268.

Sparks W., Hough J. H., Germer T. A., Robb F. and Kolokolova L. (2012) Remote sensing of chiral signatures on Mars. *Planetary and Space Science* **72**, 111–115.

Squyres S. W. and Kasting J. F. (1994) Early Mars: How Warm and How Wet? *Science*.

Stetter K. O. (1982) Ultrathin mycelia-forming organisms from submarine volcanic areas having an optimum growth temperature of 105 °C. *Nature* **300**, 258–260.

Stoker C. R., Zent A., Catling D. C., Douglas S., Marshall J. R., Archer D., Clark B., Kounaves S. P., Lemmon M. T., Quinn R., Renno N., Smith P. H. and Young S. M. M. (2010) Habitability of the Phoenix landing site. *J. Geophys. Res.* **115**, E00E20.

Stopar J. D., Taylor G. J., Velbel M. A., Norman M. D., Vicenzi E. P. and Hallis L. J. (2013) Element abundances, patterns, and mobility in Nakhlite Miller Range 03346 and implications for aqueous alteration. *Geochimica et Cosmochimica Acta* **112**, 208–225.

Storrie-Lombardi M. C. and Sattler B. (2009) Laser-Induced Fluorescence Emission (L.I.F.E.): In Situ Nondestructive Detection of Microbial Life in the Ice Covers of Antarctic Lakes. *Astrobiology* **9**, 659–672.

Strullu-Derrien C., Kenrick P., Goral T. and Knoll A. H. (2019) Testate Amoebae in the 407-Million-Year-Old Rhynie Chert. *Current Biology* **29**, 461-467.e2.

Summons R. E., Amend J. P., Bish D., Buick R., Cody G. D., Des Marais D. J., Dromart G., Eigenbrode J. L., Knoll A. H. and Sumner D. Y. (2011) Preservation of Martian Organic and Environmental Records: Final Report of the Mars Biosignature Working Group. *Astrobiology* **11**, 157–181.

Szopa C., Freissinet C., Glavin D. P., Millan M., Buch A., Franz H. B., Summons R. E., Sumner D. Y., Sutter B., Eigenbrode J. L., Williams R. H., Navarro-González R., Guzman M., Malespin C., Teinturier S., Mahaffy P. R. and Cabane M. (2020) First Detections of Dichlorobenzene Isomers and Trichloromethylpropane from Organic Matter Indigenous to Mars Mudstone in Gale Crater, Mars: Results from the Sample Analysis at Mars Instrument Onboard the Curiosity Rover. *Astrobiology* **20**, 292–306.

Tanaka K. L., Robbins S. J., Fortezzo C. M., Skinner J. A. and Hare T. M. (2014) The digital global geologic map of Mars: Chronostratigraphic ages, topographic and crater morphologic characteristics, and updated resurfacing history. *Planetary and Space Science* **95**, 11–24.

Tank M., Thiel V., Ward D. M. and Bryant D. A. (2017) A Panoply of Phototrophs: An Overview of the Thermophilic Chlorophototrophs of the Microbial Mats of Alkaline Siliceous Hot Springs in Yellowstone National Park, WY, USA. In *Modern Topics in the Phototrophic Prokaryotes: Environmental and Applied Aspects* (ed. P. C. Hallenbeck). Springer International Publishing, Cham. pp. 87–137.

Tarcea N., Frosch T., Rösch P., Hilchenbach M., Stuffler T., Hofer S., Thiele H., Hochleitner R. and Popp J. (2008) Raman Spectroscopy—A Powerful Tool for in situ Planetary Science. *Space Sci Rev* **135**, 281–292.

Tarnas J. d., Mustard J. f., Sherwood Lollar B., Stamenković V., Cannon K. m., Lorand J.-P., Onstott T. c., Michalski J. r., Warr O., Palumbo A. m. and Plesa A.-C. (2021) Earth-like Habitable Environments in the Subsurface of Mars. *Astrobiology* **21**, 741–756.

Taylor T. N., Hass H. and Kerp H. (1997) A cyanolichen from the Lower Devonian Rhynie chert. *American Journal of Botany* **84**, 992–1004.

The Meteoritical Society (2021) Meteoritical Bulletin Database. *Meteoritical Bulletin Database*.https://www.lpi.usra.edu/meteor/metbull.php (2021) Accessed November 10, 2021

Thomas-Keprta K. L., Clemett S. J., Bazylinski D. A., Kirschvink J. L., McKay D. S., Wentworth S. J., Vali H., Gibson, E. K. and Romanek C. S. (2002) Magnetofossils from Ancient Mars: a Robust Biosignature in the Martian Meteorite ALH84001. *Applied and Environmental Microbiology* **68**, 3663–3672.

Thompson M. A. (2020) The statistical reliability of 267-GHz JCMT observations of Venus: no significant evidence for phosphine absorption. *Monthly Notices of the Royal Astronomical Society: Letters* **501**, L18–L22.

Treiman A. H., Barrett R. A. and Gooding J. L. (1993) Preterrestrial aqueous alteration of the Lafayette (SNC) meteorite. *Meteoritics* **28**, 86–97.

Treiman A. H. (2005) The nakhlite meteorites: Augite-rich igneous rocks from Mars. *Geochemistry* **65**, 203–270.

Treiman A. H. and Irving A. J. (2008) Petrology of Martian meteorite Northwest Africa 998. *Meteoritics & Planetary Science* **43**, 829–854.

Trewin N. H. and Rice C. M. (1992) Stratigraphy and sedimentology of the Devonian Rhynie chert locality. *Scottish Journal of Geology* **28**, 37–47.

Turbet M. and Forget F. (2019) The paradoxes of the Late Hesperian Mars ocean. *Sci Rep* **9**, 5717.

Turner S. M. R., Bridges J. C., Grebby S. and Ehlmann B. L. (2016) Hydrothermal activity recorded in post Noachian-aged impact craters on Mars: post Noachian IMPACT CRATERS. *J. Geophys. Res. Planets* **121**, 608–625.

Uckert K., Bhartia R., Beegle L. W., Monacelli B., Asher S. A., Burton A. S., Bykov S. V., Davis K., Fries M. D., Jakubek R. S., Hollis J. R., Roppel R. D. and Wu Y.-H. (2021) Calibration of the SHERLOC Deep Ultraviolet Fluorescence–Raman Spectrometer on the Perseverance Rover. *Appl Spectrosc* **75**, 763–773.

Udry A. and Day J. M. D. (2018) 1.34 billion-year-old magmatism on Mars evaluated from the co-genetic nakhlite and chassignite meteorites. *Geochimica et Cosmochimica Acta* **238**, 292–315.

Udry A., Howarth G. H., Herd C. D. K., Day J. M. D., Lapen T. J. and Filiberto J. (2020) What Martian Meteorites Reveal About the Interior and Surface of Mars. *Journal of Geophysical Research: Planets* **125**, e2020JE006523.

Usui T., Alexander C. M. O., Wang J., Simon J. I. and Jones J. H. (2012) Origin of water and mantle–crust interactions on Mars inferred from hydrogen isotopes and volatile element abundances of olivine-hosted melt inclusions of primitive shergottites. *Earth and Planetary Science Letters* **357–358**, 119–129.

Váci Z. and Agee C. (2020) Constraints on Martian Chronology from Meteorites. *Geosciences* **10**, 455.

Vago J. L., Westall F., Pasteur Instrument Teams L. S. S. W. G. and Other Contributors, Coates A. J., Jaumann R., Korablev O., Ciarletti V., Mitrofanov I., Josset J.-L., De Sanctis M. C., Bibring J.-P., Rull F., Goesmann F., Steininger H., Goetz W., Brinckerhoff W., Szopa C., Raulin F., Westall F., Edwards H. G. M., Whyte L. G., Fairén A. G., Bibring J.-P., Bridges J., Hauber E., Ori G. G., Werner S., Loizeau D., Kuzmin R. O., Williams R. M. E., Flahaut J., Forget F., Vago J. L., Rodionov D., Korablev O., Svedhem H., Sefton-Nash E., Kminek G., Lorenzoni L., Joudrier L., Mikhailov V., Zashchirinskiy A., Alexashkin S., Calantropio F., Merlo A., Poulakis P., Witasse O., Bayle O., Bayón S., Meierhenrich U., Carter J., García-Ruiz J. M., Baglioni P., Haldemann A., Ball A. J., Debus A., Lindner R., Haessig F., Monteiro D., Trautner R., Voland C., Rebeyre P., Goulty D., Didot F., Durrant S., Zekri E., Koschny D., Toni A., Visentin G., Zwick M., van Winnendael M., Azkarate M., Carreau C. and the E. P. T. (2017) Habitability on Early Mars and the Search for Biosignatures with the ExoMars Rover. *Astrobiology* **17**, 471–510.

Verbeeck J., Hens S., Potapov P. and Schryvers D. (2005) ELECTRON ENERGY LOSS SPECTROMETRY. In *Encyclopedia of Analytical Science (Second Edition)* (eds. P. Worsfold, A. Townshend, and C. Poole). Elsevier, Oxford. pp. 324–331.

Vernon-Parry K. D. (2000) Scanning electron microscopy: an introduction. *III-Vs Review* **13**, 40–44.

Villanueva G. L., Cordiner M., Irwin P. G. J., de Pater I., Butler B., Gurwell M., Milam S. N., Nixon C. A., Luszcz-Cook S. H., Wilson C. F., Kofman V., Liuzzi G., Faggi S., Fauchez T. J., Lippi M., Cosentino R., Thelen A. E., Moullet A., Hartogh P., Molter E. M., Charnley S., Arney G. N., Mandell A. M., Biver N., Vandaele A. C., de Kleer K. R. and Kopparapu R. (2021) No evidence of phosphine in the atmosphere of Venus from independent analyses. *Nat Astron* **5**, 631–635.

virtualmicroscope.org (2022) Nakhla 2 - Virtual Microscope.http://www.virtualmicroscope.org/content/nakhla-2 (2022) Accessed March 30, 2022

Vurpillot F., Gault B., Geiser B. P. and Larson D. J. (2013) Reconstructing atom probe data: A review. *Ultramicroscopy* **132**, 19–30.

Wadhwa M. and Crozaz G. (1995) Trace and minor elements in minerals of nakhlites and Chassigny: Clues to their petrogenesis. *Geochimica et Cosmochimica Acta* **59**, 3629–3645.

Walter M. R. and Des Marais D. J. (1993) Preservation of Biological Information in Thermal Spring Deposits: Developing a Strategy for the Search for Fossil Life on Mars. *Icarus* **101**, 129–143.

Webster C. R., Mahaffy P. R., Atreya S. K., Flesch G. J., Mischna M. A., Meslin P.-Y., Farley K. A., Conrad P. G., Christensen L. E., Pavlov A. A., Martín-Torres J., Zorzano M.-P., McConnochie T. H., Owen T., Eigenbrode J. L., Glavin D. P., Steele A., Malespin C. A., P. Douglas Archer J., Sutter B., Coll P., Freissinet C., McKay C. P., Moores J. E., Schwenzer S. P., Bridges J. C., Navarro-Gonzalez R., Gellert R., Lemmon M. T. and Team the M. S. (2015) Mars methane detection and variability at Gale crater. *Science*.

Wellman C. H. (2019) Palaeontology: The Rhynie Chert Is the Gift that Keeps on Giving. *Current Biology* **29**, R93–R95.

Westall F., Foucher F., Cavalazzi B., de Vries S. T., Nijman W., Pearson V., Watson J., Verchovsky A., Wright I., Rouzaud J.-N., Marchesini D. and Anne S. (2011) Volcaniclastic habitats for early life on Earth and Mars: A case study from ~3.5Ga-old rocks from the Pilbara, Australia. *Planetary and Space Science* **59**, 1093–1106.

Westall F., Loizeau D., Foucher F., Bost N., Betrand M., Vago J. and Kminek G. (2013) Habitability on Mars from a Microbial Point of View. *Astrobiology* **13**, 887–897.

Westall F., Foucher F., Bost N., Bertrand M., Loizeau D., Vago J. L., Kminek G., Gaboyer F., Campbell K. A., Bréhéret J.-G., Gautret P. and Cockell C. S. (2015) Biosignatures on Mars: What, Where, and How? Implications for the Search for Martian Life. *Astrobiology* **15**, 998–1029.

Whalley P. and Jarzembowski E. A. (1981) A new assessment of Rhyniella, the earliest known insect, from the Devonian of Rhynie, Scotland. *Nature* **291**, 317–317.

Wierzchos J., Cámara B., De Los Ríos A., Davila A. F., Sánchez Almazo I. M., Artieda O., Wierzchos K., Gómez-Silva B., Mckay C. and Ascaso C. (2011) Microbial

colonization of Ca-sulfate crusts in the hyperarid core of the Atacama Desert: implications for the search for life on Mars. *Geobiology* **9**, 44–60.

Williams D. B. and Carter C. B. (2009) *Transmission Electron Microscopy*., Springer US, Boston, MA.

Williford K. H., Farley K. A., Stack K. M., Allwood A. C., Beaty D., Beegle L. W., Bhartia R., Brown A. J., de la Torre Juarez M., Hamran S.-E., Hecht M. H., Hurowitz J. A., Rodriguez-Manfredi J. A., Maurice S., Milkovich S. and Wiens R. C. (2018) Chapter 11 - The NASA Mars 2020 Rover Mission and the Search for Extraterrestrial Life. In *From Habitability to Life on Mars* (eds. N. A. Cabrol and E. A. Grin). Elsevier. pp. 275–308.

Wordsworth R. D., Kerber L., Pierrehumbert R. T., Forget F. and Head J. W. (2015) Comparison of "warm and wet" and "cold and icy" scenarios for early Mars in a 3-D climate model: WARM AND WET VS. COLD AND ICY EARLY MARS. *J. Geophys. Res. Planets* **120**, 1201–1219.

Wordsworth R. D. (2016) The Climate of Early Mars. *Annual Review of Earth and Planetary Sciences* **44**, 381–408.

zeiss.com (2022) ZEISS ZEN Microscope Software for Microscope Components.https://www.zeiss.com/microscopy/int/products/microscope-software/zen.html (2022) Accessed March 26, 2022

Zhou W., Apkarian R., Wang Z. L. and Joy D. (2006) Fundamentals of Scanning Electron Microscopy (SEM). In *Scanning Microscopy for Nanotechnology* (eds. W. Zhou and Z. L. Wang). Springer New York, New York, NY. pp. 1–40.

Zurbuchen T. and Parker D. (2018) Joint Statement of Intent between the National Aeronautics and Space Administration and the European Space Agency on Mars Sample Return.https://mepag.jpl.nasa.gov/announcements/2018-04-26%20NASA-ESA%20SOI%20(Signed).pdf (2018) Accessed December 3, 2021